SATELLITE DYNAMICS AND ATTITUDE CONTROL

Max Newport, Valerie Pietrasz

06 April 2021

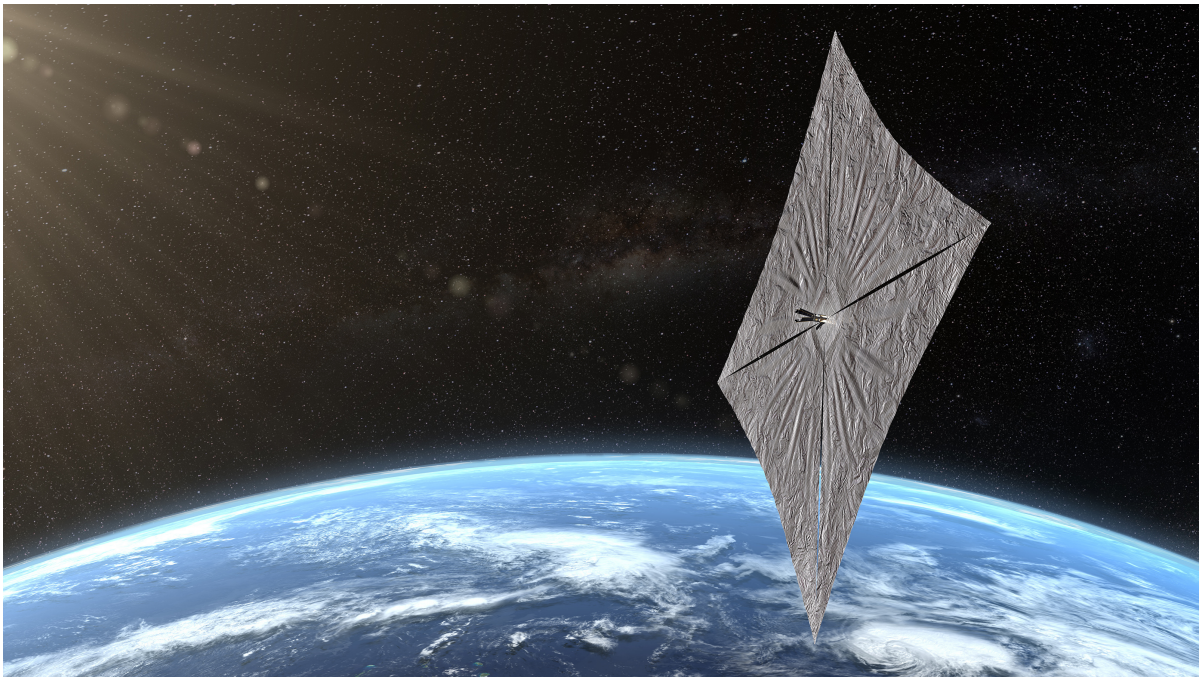

REVISION HISTORY

VERSION	REVISION NOTES
PS1	- Created document - Added PS1 material: Mission specifications, satellite selection. Structure and mass distribution. Inertia matrix, body axes. Orbit.
PS2	- Added PS2 material: Euler propagation, validation, axisymmetry. - Modified inertia to include asymmetric components (in PS1 and Appendix).
PS3	- Added PS3 material: attitude propagation, integration. - Stability and equilibrium tests. - Added comparison of Euler 312 and quaternion results (Appendix).
PS4	- Added PS4 material: dual spin, gravity gradient.
PS5	- Renumbered section to align with PS numbers. - Modified formatting to constrain figures to their relevant sections. - Added PS5 material: magnetic field, SRP, and atmospheric drag perturbations. Attitude control errors. - Added gravity gradient stability analysis (in PS4).
PS6	- Added PS6 material: Attitude determination, estimation error. Sensor measurements, sensor noise.
PS7	- Added PS7 material: Extended Kalman Filter, sensor error represntation. - Added estimated attitude control error (in PS6), further fleshed out comparison of attitude determination methods (Appendix).

Table 1: Summary of project revisions.

TABLE OF CONTENTS

INTRODUCTION

We have chosen to study the LightSail 2 mission (LS2), a solar sailing proof-of-concept mission developed by The Planetary Society. Solar sails use solar radiation pressure (SRP) to propel the spacecraft, and JAXA's IKAROS mission in 2021 was the first mission to successfully do so in interplanetary space. In contrast, LS2 used solar sailing in Earth orbit to perform a controlled orbital maneuver: namely, raising spacecraft apogee.

1 PROBLEM SET 1

1.1 MISSION ADCS CHARACTERISTICS

We will model LightSail 2's mission objectives and hardware. The spacecraft was deployed into a circular, low-earth orbit at 720km altitude, 24 degrees inclination, where it then attempted to raise its apogee using solar sailing. For analysis, we will use the starting orbital parameters with arbitrary values selected for the unknown parameters, as noted in the orbital elements section.

The method by which LS2 raised its apogee is called the on/off control strategy. While the spacecraft was moving away from the sun, the sail normal vector pointed toward the sun ("on") in order to increase spacecraft velocity. While the spacecraft was moving toward the sun, the spacecraft normal pointed perpendicularly to the direction of the sun ("off"), to maintain orbit until the spacecraft was once again moving away from the sun. Thus, the spacecraft had two target attitudes: sun pointing and sun-perpendicular pointing. *The spacecraft attitude will be represented in this project using quaternions.*

In order to realize sun and sun-perpendicular pointing, the spacecraft will require at minimum sun sensors, but additional sensors for accuracy improvement and redundancy would be preferred. To move between the two target attitudes will require 90 degree slew maneuvers twice per orbit, which can be achieved with a variety of actuators. In this case, torque rods and momentum wheels were used.

The high level ADCS requirements are listed below [8]. To keep the project within a reasonable scope, we will focus on those above the line. Anything below the line will be assumed to be met.

- Provide attitude knowledge to within 5 degrees per axis during all mission phases.
- Sun sensors provide data on the angle of light incidence to the sensors to within $\pm$ 3 degrees accuracy.
- Magnetometers provide attitude knowledge of the body-fixed x-, y-, and z-axes to within $\pm$ 5 degrees relative to the Earth magnetic field.
- Utilize a momentum wheel to achieve 90-degree slew maneuvers about one axis in $<$ 5 minutes.
- Following solar sail deployment, be capable of providing an angular acceleration of 0.0005 degrees/sec^2 per axis.
- Detumble from a maximum of 10 degrees per second per axis after sail deployment.
- Align +Z axis of the spacecraft with the magnetic field with maximum variation once settled of $<$ 60 degrees.

Component	Number	Range	Accuracy
Sun sensors	5	[15, 165] deg/axis	± 3 deg/axis
Magnetometers	4	[40μ, 2] Gauss/axis	± 5 deg/axis
Primary Gyro	1		± 1 deg/axis
Intrepid Gyro	1		± 1 deg/axis

Table 2: LS2 Sensors

Component	Number	Specifications
Torque Rods	3	Max torque: 1 $Am^2 \times \vec{B}$
Momentum Wheel	1	Max torque: 0.06 Nm^2

Table 3: LS2 Actuators

- Damp attitude rates within 2 hours of P-POD deployment.
- Accommodate a tip off rate of up to 25 degree/sec per axis from P-POD deployment.
- Prior to sail deployment, utilize torque rods to achieve attitude control to within 10 degree per axis.
- Prior to sail deployment, be capable of providing an angular acceleration of 0.1 degrees/s^2 per axis.
- Prior to solar sail deployment, provide attitude control to within 10 degrees per axis.
- Downlink telemetry for sensors, actuators and performance data.
- Sample spacecraft angular rates using gyro sensors.
- Be actively controllable in each of its three-axes.

To achieve these objectives, LS2 used the sensors and actuators listed in Tables 3 and 2. These components were selected for their low cost, low mass, and reliability.

1.2 SIMILAR MISSIONS

There are several satellites with similar mission objectives. LightSail 1 (LS1) was originally developed to meet the same objective, but was down-scoped to only achieve the goals listed prior to and including sail deployment. To reduce development costs, LS2 reused much of the LS1 design. Notable differences include a lower orbital altitude (400km for LS1 compared to 720km for LS2), removing the momentum wheel to simplify the spacecraft and reduce costs, and a simpler ADCS on LS1 [4].

IKAROS, the first successful solar sail mission, differed from LS2 in three major respects: first, it orbits the sun rather than Earth, and thus must survive the interplanetary, rather than near-Earth, environment. Secondly, it performs attitude control using liquid crystals in the sail that alter the diffusivity and reflectivity of the solar sail to allow for differential SRP across the sail [12]. Lastly, while LS1 and 2 used rigid booms to maintain the sail's shape, IKAROS removed these to save mass, and thus relies on centrifugal force from spacecraft spin to keep the sail extended. All of these differences have driven ADCS requirements that are different from LS2 (such as maintaining a minimum spin about the axis normal to the sail).

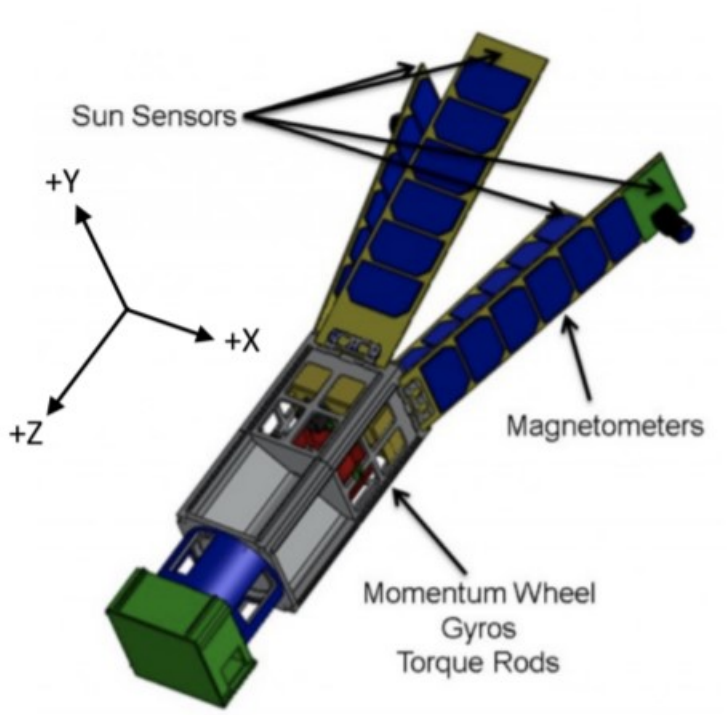

Figure 1: Annotated Full-Detail Layout of 3U Structure

NASA has launched missions similar to LS1 and LS2, NanoSail-D, to prove usage of solar sails as passive de-orbiting mechanisms. The first NanoSail-D was lost in launch, while the second performed many of the desired functions, de-orbiting after 240 days [3].

Another relevant mission is Prox-1, LS2's launch partner. Originally developed to demonstrate automated, close-proximity maneuvers relative to another CubeSat (with LS2 as its target), the proximity maneuvers were ultimately cut and the spacecraft now serves primarily to monitor and image LS2. Prox-1's ADCS mission requirements are very different (and more strict) than LS2's, requiring greater attitude knowledge and control to perform its maneuvers and imaging [9].

1.3 MECHANICAL LAYOUT

High-level drawings of the LS2 system in its various configurations are provided in Appendix B; note that this study will only consider the `LIGHTSAIL DEPLOYED` configuration. The basic layout of the 3U structure with the placement of primary ACDS components is provided in Figure 1. The body coordinates used to describe the mechanical layout are plotted in Figure 2. Note that the system is roughly axisymmetric over the x and y, with the $+z$ axis pointing away from the deployed solar panels.

LS2 uses a motorized TRAC (Triangular Roll-able And Collapsible) boom deployment system to unfurl its 5.57m square Mylar sail. During launch, the 4 primary solar panels are folded along the length of the satellite - once deployed, the panels extend along the $-z$ axis. After de-tumbling with magnetic torquing, the booms extend and unfold the 4.5 micron thick Mylar from a central "sail housing" unit. Due to limited knowledge about the exact mass distribution of the satellite and a desire for a simplified model, the mechanical layout has been reduced to five primary components, detailed in Table 4 below. The mass calculations are described in

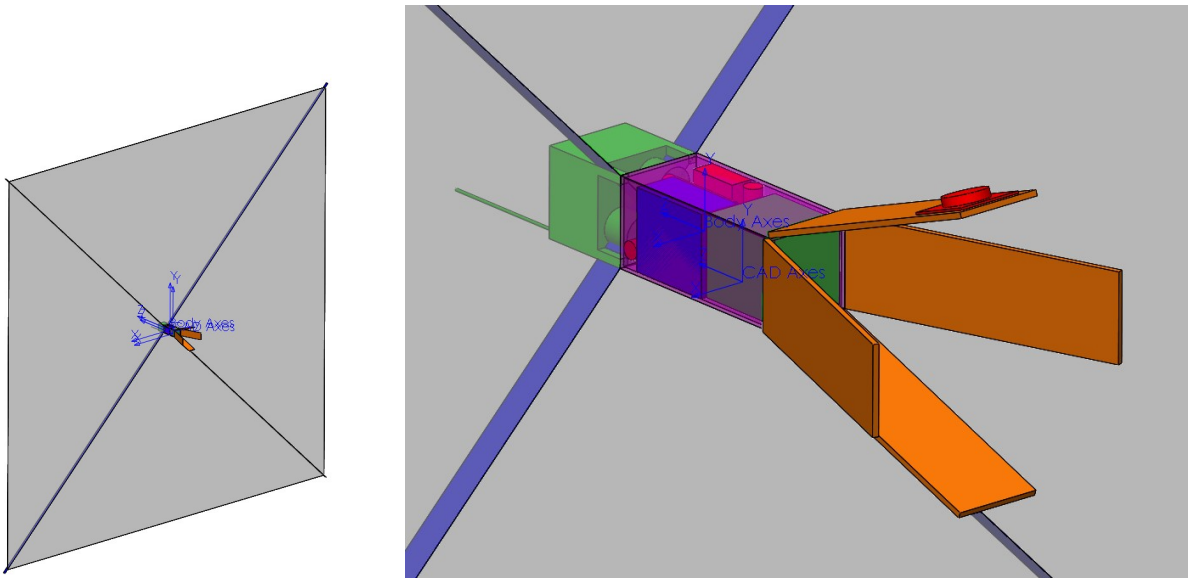

(a) Structure w/ Body Axes (b) Detail of Simplified Cubesat Structure w/ Axes

Figure 2: Simplified Mechanical Layout of LightSail 2

Name	Color in 3D Model	Subsystems	Mass (kg)
Forward Body	Green	Comms, Boom Motors (x2), Boom Housing	1.47
Booms	Blue	TRAC Booms (x4)	0.93
Solar Sail	Grey	Mylar sail	0.20
Rear Body	Purple	Magnotorquers, Mom. Wheel, Power, Avionics	1.73
Solar Panels	Orange	Solar Cells, Magnetometers, Cameras	0.60
TOTAL	**-**	**-**	**4.93**

Table 4: Primary Components of Simplified Mechanical Layout

further detail in Appendix A; while some effort was taken to include asymmetric contributions to the total volume, the large contribution of the square solar sail creates a fairly axisymmetric system.

1.4 INERTIA PROPERTIES

The inertia properties provided below were computed using the 3D model shown in Figure 2. An analytical verification of these values is provided in Appendix D. Along the principal axes, the moments of the inertia for the system are

$$I_{xx} = 3.10288 \text{ kg} \cdot \text{m}^2,\ I_{yy} = 3.10553 \text{ kg} \cdot \text{m}^2,\ I_{zz} = 5.98305 \text{ kg} \cdot \text{m}^2$$

Using our 3D model to calculate the full inertia matrix yields, in the body frame,

$$L = \begin{bmatrix} 3.10553 & -0.00011 & -0.00003 \\ -0.00011 & 3.10289 & -0.00005 \\ -0.00003 & -0.00005 & 5.98305 \end{bmatrix} \text{ kg} \cdot \text{m}^2$$

1.5 OUTER SURFACE DISCRETIZATION

To provide an easy way of analyzing environmental perturbative torques, we also simplify the outer geometry. The surface normals and centroids are pulled from the CAD model, where the solar panels and solar sail are taken to have a negligible thickness (effectively reducing those components to planes) and minor elements like cameras are not included in the discretization. Using the Solidworks VBA Macro in Appendix C, we export the centroid, unit normal, and area information for each outward-facing surface of interest. A MATLAB script (included in the same appendix) imports the information into MATLAB data structures for use in future simulations. Table 5 displays the centroid locations in body coordinates, the associated normal vector, and the associated area.

Location (m)	**Normal Vec**	**Area** (m^2)
(-0.003, -0.054, -0.049)	(0, -1, 0)	0.023
(0.047, -0.004, -0.049)	(1, 0, 0)	0.023
(-0.003, 0.046, -0.049)	(0, 1, 0)	0.023
(-0.053, -0.004, -0.049)	(-1, 0, 0)	0.023
(-0.003, -0.004, -0.164)	(0, 0, -1)	0.01
(-0.003, 0.1, -0.313)	(0, -0.94, -0.342)	0.032
(0.101, -0.004, -0.313)	(-0.94, 0, -0.342)	0.032
(-0.003, -0.108, -0.313)	(0, 0.94, -0.342)	0.032
(-0.107, -0.004, -0.313)	(0.94, 0, -0.342)	0.032
(-0.003, 0.1, -0.313)	(0, 0.94, 0.342)	0.032
(-0.107, -0.004, -0.313)	(-0.94, 0, 0.342)	0.032
(-0.003, -0.108, -0.313)	(0, -0.94, 0.342)	0.032
(0.101, -0.004, -0.313)	(0.94, 0, 0.342)	0.032
(-0.053, -0.004, 0.121)	(-1, 0, 0)	0.011
(-0.003, -0.054, 0.121)	(0, -1, 0)	0.011
(0.047, -0.004, 0.121)	(1, 0, 0)	0.011
(-0.003, 0.046, 0.121)	(0, 1, 0)	0.011
(-0.003, -0.004, 0.176)	(0, 0, 1)	0.01
(-0.003, -0.004, 0.066)	(0, 0, -1)	31.003
(-0.003, -0.004, 0.066)	(0, 0, 1)	31.003

Table 5: Centroid, normal, and area data pulled from CAD model.

1.6 ORBITAL ELEMENTS & PROPAGATION

The initial orbit propagator was developed for AA 279A in Winter 2019, and later further supplemented to include simple orbital perturbations (namely, atmospheric drag and J2, with

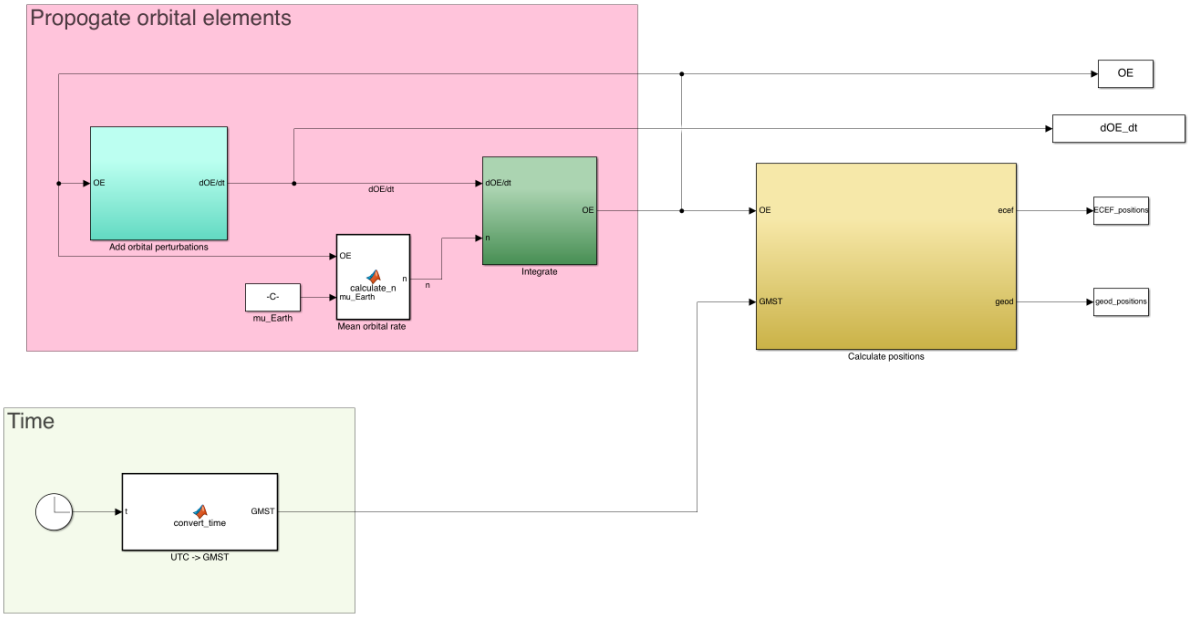

Figure 3: Top-level overview of the initial orbit propagator.

the infrastructure in place to add additional perturbations as relevant). SRP will be added to model the change in apogee that is one of the mission objectives. It will be incorporated into the ADCS simulation, and an overview is presented in Figure 3.

Initial values for the orbital elements are given in Table 6. These were used to produce the sample orbits given in Figure 4.

Orbital element	**Symbol**	**Initial value**	**Units**	**Notes**
Epoch	t_0	2019-07-08.20	YY-MM-DD.dd	
Semi-major axis	a	7095.553	km	$R_E + 717.4175$km
Eccentricity	e	0.0010951		
Inclination	i	24	deg	
RAAN	Ω	0	deg	Selected arbitrarily
Argument of Periapsis	ω	0	deg	Selected arbitrarily
Eccentric anomaly	E	0	rad	Selected arbitrarily

Table 6: Initial orbital elements, pulled from [11]. The arbitrarily selected values are those for which we do not have data, and have little effect on our modeling.

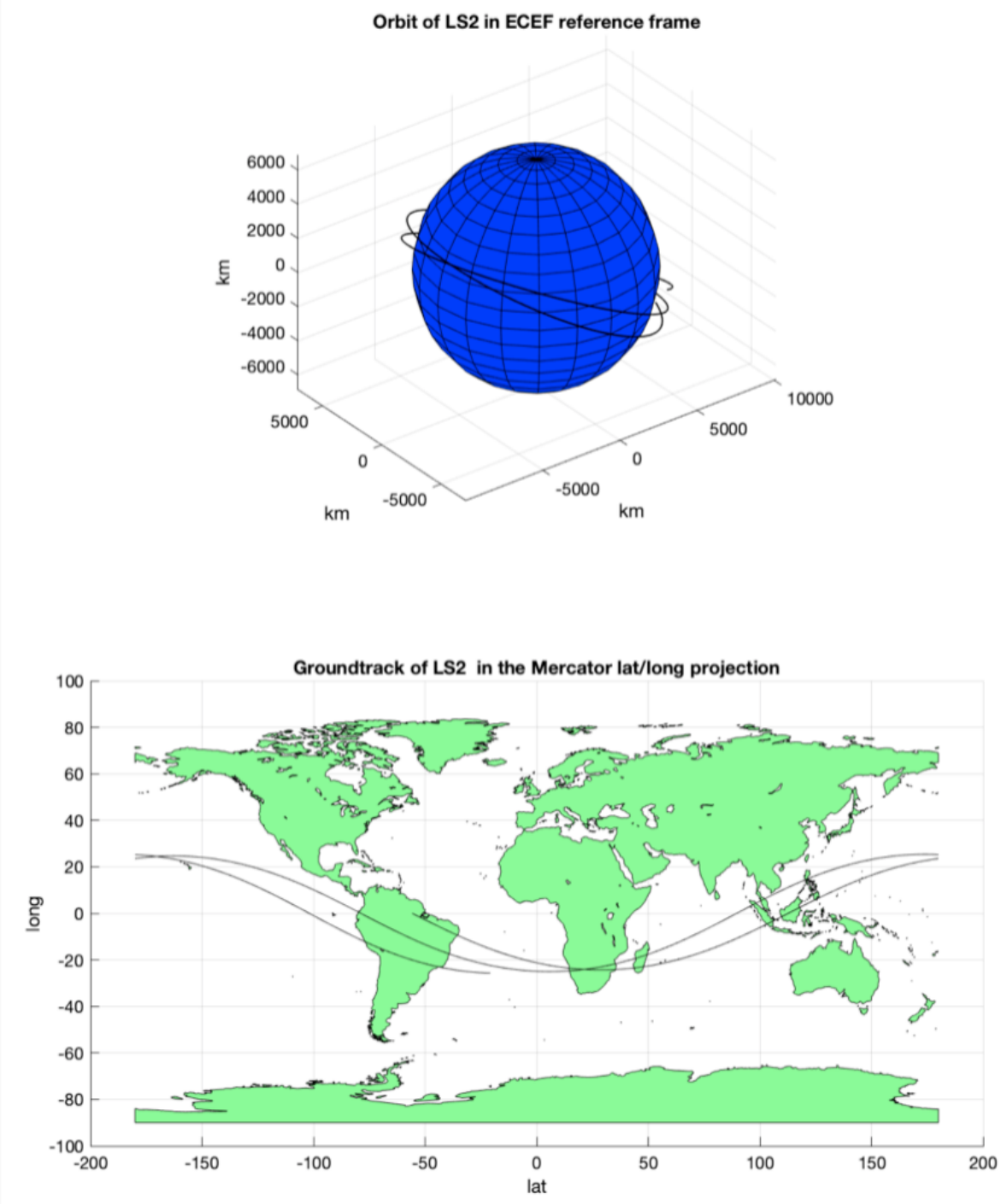

Figure 4: Initial sample orbits of LS2 given the orbital parameters in Table 6.

2 PROBLEM SET 2

2.1 PRINCIPAL AXES

The principal axes are shown alongside the body axes in Figure 5 - note that due to the overwhelming inertial contribution of the solar sail and booms, the primary difference between the axes systems is the flipping of the x and y axes to ensure well-ordered eigenvalues. Using the MATLAB script below, we can calculate the rotation matrix from the principal axes to body axes (whose columns represent the expression of the principal axes in body coordinates).

$$R = \begin{bmatrix} 0.04156 & 0.99911 & -1.042 \times 10^{-5} \\ 0.9991 & -0.04156 & -1.736 \times 10^{-5} \\ 1.778 \times 10^{-5} & 9.695 \times 10^{-6} & 1.000 \end{bmatrix}$$

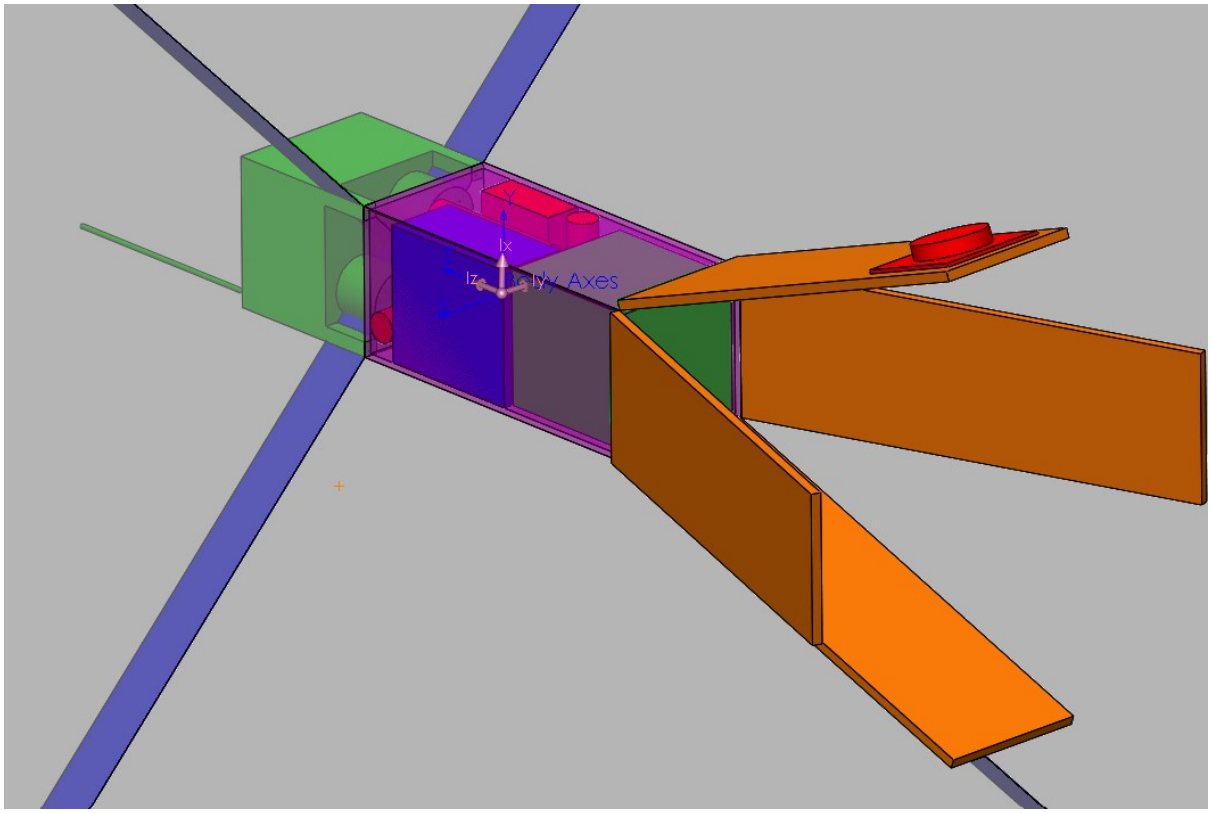

Figure 5: Body axes (blue) and principal inertia axes (pink), overlaying the simplified spacecraft CAD model.

2.2 NO-TORQUE PROPAGATION

Using the Simulink block-diagram in Figure 6, we can propagate the angular velocity without the contribution of torque with respect to the principal axes. Plotting the resulting polhode over top of the momentum and energy ellipses that constrain the motion of the spacecraft in Figure 7, we can clearly see how our angular velocity vector is constrained to lay along the intersection of the two ellipses. Additionally, we can see from the planar projections of the polhode that while the x and z projections are (sections of) ellipses, the y projection is a hyperbola. Note that we use the following (arbitrary) initial angular velocity (expressed in principal axes) for our spacecraft:

$$\omega_0 = \begin{bmatrix} -6 \\ 8 \\ 0.1 \end{bmatrix} \text{ deg/sec}$$

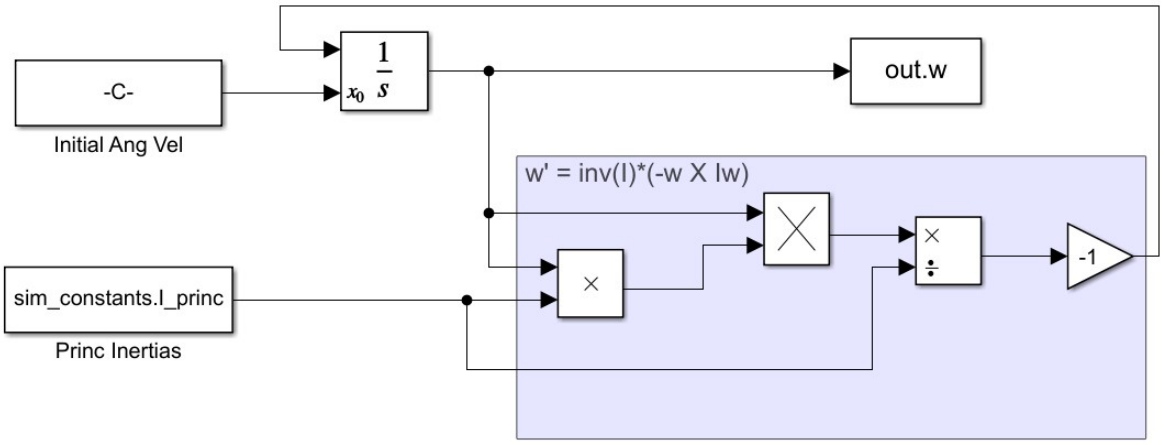

Figure 6: Simulink block diagram for propagating no-torque Euler equations in principal axes.

To verify that our solution works in other cases, we consider an angular velocity along a principal axis to test out our propagator:

$$\omega_{0,2} = \begin{bmatrix} 0 \\ -10 \\ 0 \end{bmatrix} \text{ deg/sec}$$

The results of this propagation are shown in Figure 8. Again, our results are as expected - our angular velocity remains constant, but appears to lay at an unstable equilibrium (which makes sense, as our spin is about the intermediate axis - any off-axis angular velocity, however small, would result in tumbling).

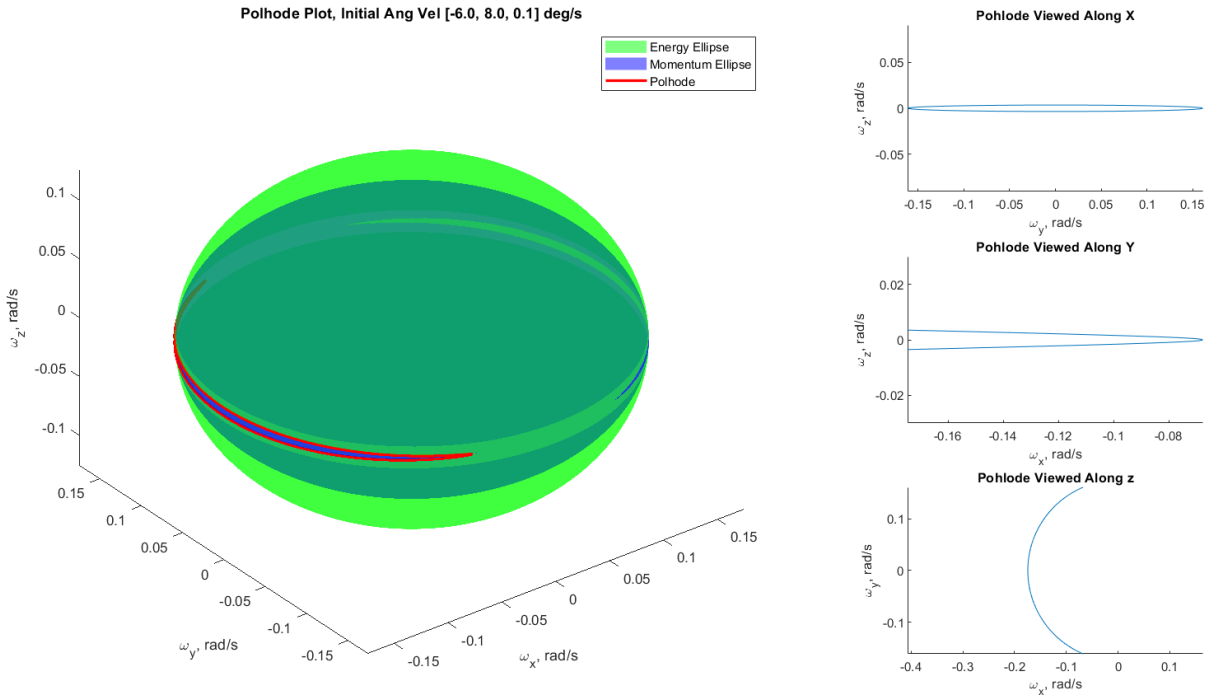

Figure 7: Plot of spacecraft polhode propagation in principal axes, assuming no-torque and non-trivial initial conditions.

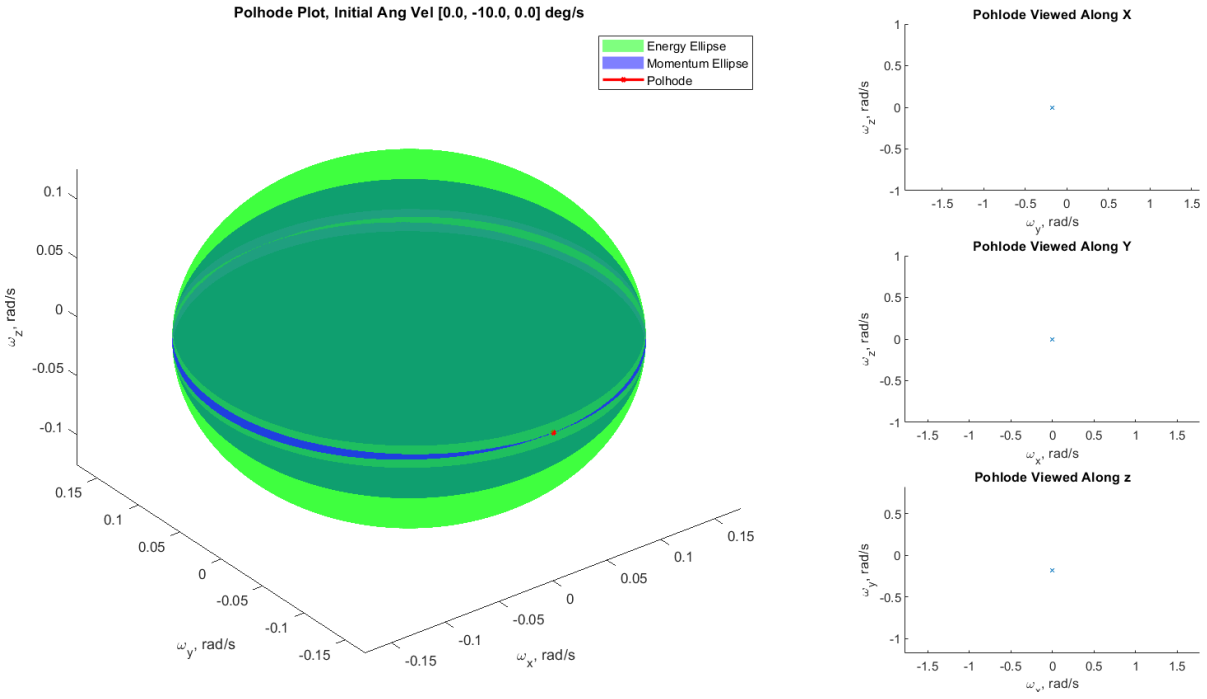

Figure 8: Plot of polhode propagation in principal axes, assuming no-torque and an initial angular velocity along the intermediate axis only.

2.3 AXIAL SYMMETRY

Although our spacecraft is nearly axisymmetric, we would like to analyze the case of torqueless true axial symmetry. For this, we set $I_{xx} = I_{yy} = 3.10288\text{kg} \cdot \text{m}^2$. The solution to Euler's equations in the axisymmetric case, where $\lambda = \frac{I_z - I_x}{I_x}\omega_z$, is simply the circle

$$\omega_{xy} = (\omega_{x0} + i\omega_{y0}) \exp(i\lambda t) \tag{1}$$

As usual for this representation of circles, ω_x is the real component while ω_y is the imaginary. Using the initial conditions that generated Figure 7, the analytic result across time is shown in Figure 9.

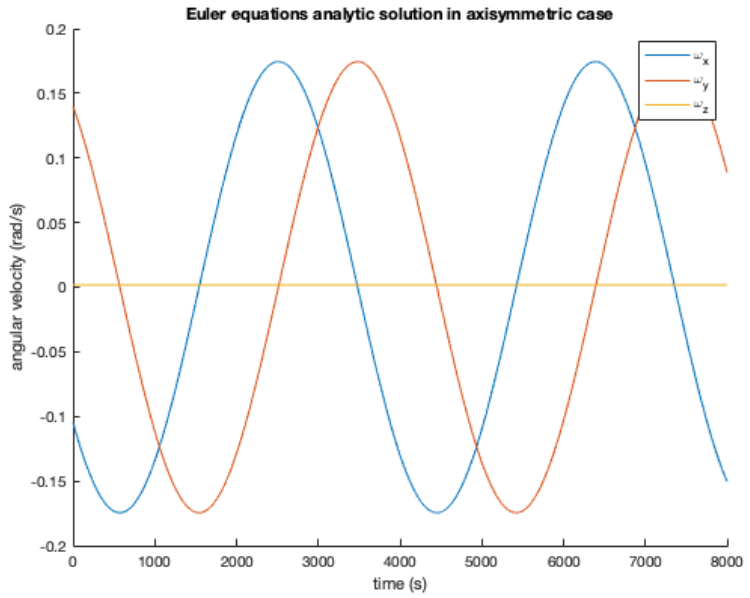

Figure 9: Time-domain solution of axisymmetric Euler equations using $\omega_0 = [-6, 8, 0.1]$.

Comparing to the numeric results achieved using numeric propagation of the Euler equations, the error evolves as in Figure 10. First, we observe that there is no ω_z error. This is expected as in this system, it is constant and uncoupled from ω_x, ω_y, so there should be no numeric integration error. For ω_x, ω_y, the error starts small – on the order of 10^{-10} rad/s. The error behaves as sinusoids with mean 0 (and period similar to analytic result) bounded by exponential growth – the amplitudes are growing and will continue to grow unbounded as time progresses, although it will take many revolutions to reach any substantial error. Further, there is a phase delay between ω_x, ω_y in the numeric propagator.

Thus, within the integration error, the angular velocity vectors exchange momentum as expected, maintaining a constant ω_{xy}. However, there will be an apparent fluctuation of angular momentum about the mean due to integration error.

Finally, we compare the numeric results of the no-torque pseudo-axisymmetric case, as we have modelled the satellite, to the true axisymmetric case in Figure 11. Although the differences in inertia in the two cases are small ($I_{yy} = 3.10288\text{kg} \cdot \text{m}^2$ in the ideal case versus $I_{yy} = 3.10553kg \cdot m^2$ in the real case), the error is not small for ω_x, ω_y. Because ω_z is largely decoupled and constant, this error is small, although noticeable. From this, we can see it is important for us to simulate the coupled motion of the nearly symmetric axes of our spacecraft and not make the true axisymmetric assumption.

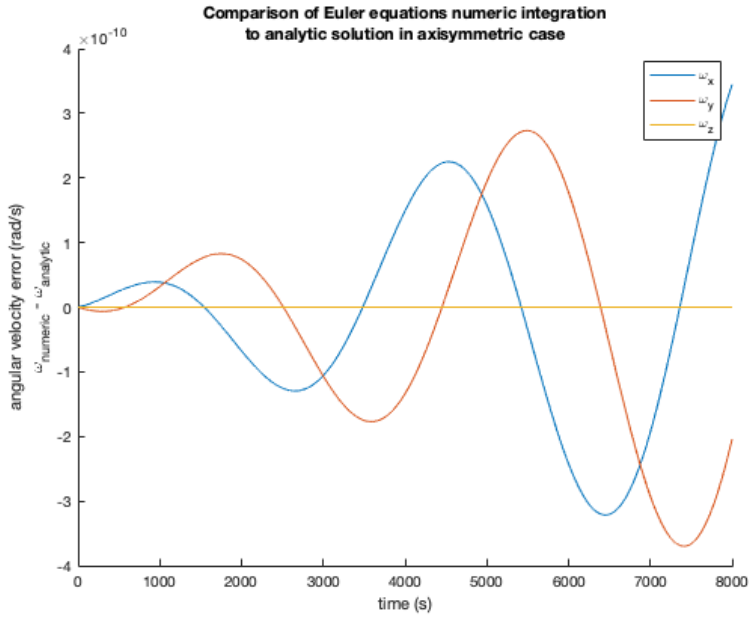

Figure 10: Evolution of error of numeric integration of Euler equations in the axisymmetric case ($\omega_0 = [-6, 8, 0.1]$.)

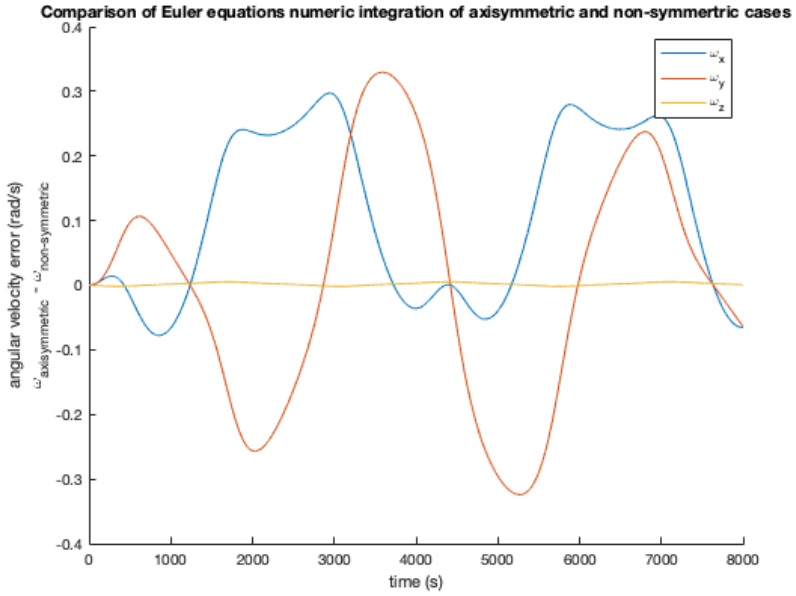

Figure 11: Evolution of difference between numeric integration of Euler equations in the pseudo-axisymmetric and true axisymmetric cases ($\omega_0 = [-6, 8, 0.1]$.)

3 PROBLEM SET 3

3.1 KINEMATIC INTEGRATION

To build toward an easily validated system, we build in kinematics integration that supports two types of attitude parameterization: quaternions (our primary method) and 312 Euler angles (a secondary method for validation). By toggling an input boolean, the simulation's attitude propagation can be switched between the two attitude parameterizations with ease.

The kinematics equation for quaternions was developed in class as

$$\frac{d\vec{q}}{dt} = \frac{1}{2}\Omega\vec{q} \tag{2}$$

for Ω as a function of the angular velocity, $\vec{\omega}$,

$$\Omega = \begin{bmatrix} 0 & \omega_z & -\omega_y & \omega_x \\ -\omega_z & 0 & \omega_x & \omega_y \\ \omega_y & -\omega_x & 0 & \omega_z \\ -\omega_x & -\omega_y & -\omega_z & 0 \end{bmatrix}$$

For 312 Euler angles, we derive the kinematics equation starting with the angular velocity in principal axes

$$\vec{\omega} = \dot{\phi}\hat{3} + \dot{\theta}\hat{1}' + \dot{\psi}\hat{y}$$

We get the components in principal frame by projecting onto the principal axes

$$\begin{aligned} \omega_x &= \vec{\omega}\cdot\hat{x} = \dot{\phi}(\hat{3}\cdot\hat{x}) + \dot{\theta}(\hat{1}'\cdot\hat{x}) \\ &= \dot{\phi}\cos\theta\sin\psi + \dot{\theta}\cos\psi \end{aligned}$$

$$\begin{aligned} \omega_y &= \vec{\omega}\cdot\hat{y} = \dot{\phi}(\hat{3}\cdot\hat{y}) + \dot{\theta}(\hat{1}'\cdot\hat{y}) + \dot{\psi} \\ &= \dot{\phi}\sin\theta + \dot{\psi} \end{aligned}$$

$$\begin{aligned} \omega_z &= \vec{\omega}\cdot\hat{z} = \dot{\phi}(\hat{3}\cdot\hat{z}) + \dot{\theta}(\hat{1}'\cdot\hat{z}) \\ &= \dot{\phi}\cos\theta\cos\psi - \dot{\theta}\sin\psi \end{aligned}$$

Solving for our angular rates, we get

$$\begin{aligned} \dot{\phi} &= \frac{1}{cos\theta}(\omega_x\sin\psi + \omega_z\cos\psi) \\ \dot{\theta} &= \omega_x\cos\psi - \omega_z\sin\psi \\ \dot{\psi} &= \omega_y + \tan\theta(\omega_x\sin\psi + \omega_z\cos\psi) \end{aligned} \tag{3}$$

Note the singularity at $\theta = \frac{\pi}{2}$ for this parameterization.

Integrating our kinematics equations with the Euler equations from the previous problem set gives a full determination of our attitude in our orbital propagation. Using the bi-directional conversions between quaternions, 312 Euler angles, and direction cosine matrices, we can compare our solutions and visualize our attitude throughout the orbit. All solution below are generated using the quaternion kinematics, but a brief comparison with the 312 Euler results is provided in Appendix F.

3.2 ATTITUDE PROPAGATION

Given our previously-defined initial conditions, we propagate our spacecraft through a single orbit period. We can then verify that our simulated attitude and angular velocity match our expectations. In Fig 12, we can see that the components of angular momentum remain very nearly constant in the inertial frame throughout the duration of simulation (note that the small errors are due to numerical propagation effects). In Fig 13, we see that the angular velocity trace in inertial coordinates, the "herpolhode," lays in a plane normal to the (constant) angular momentum vector.

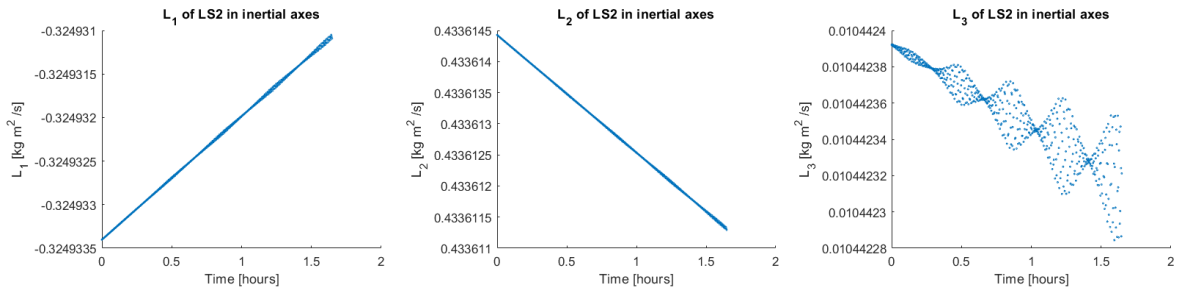

Figure 12: Components of Angular Momentum in Inertial Coordinates

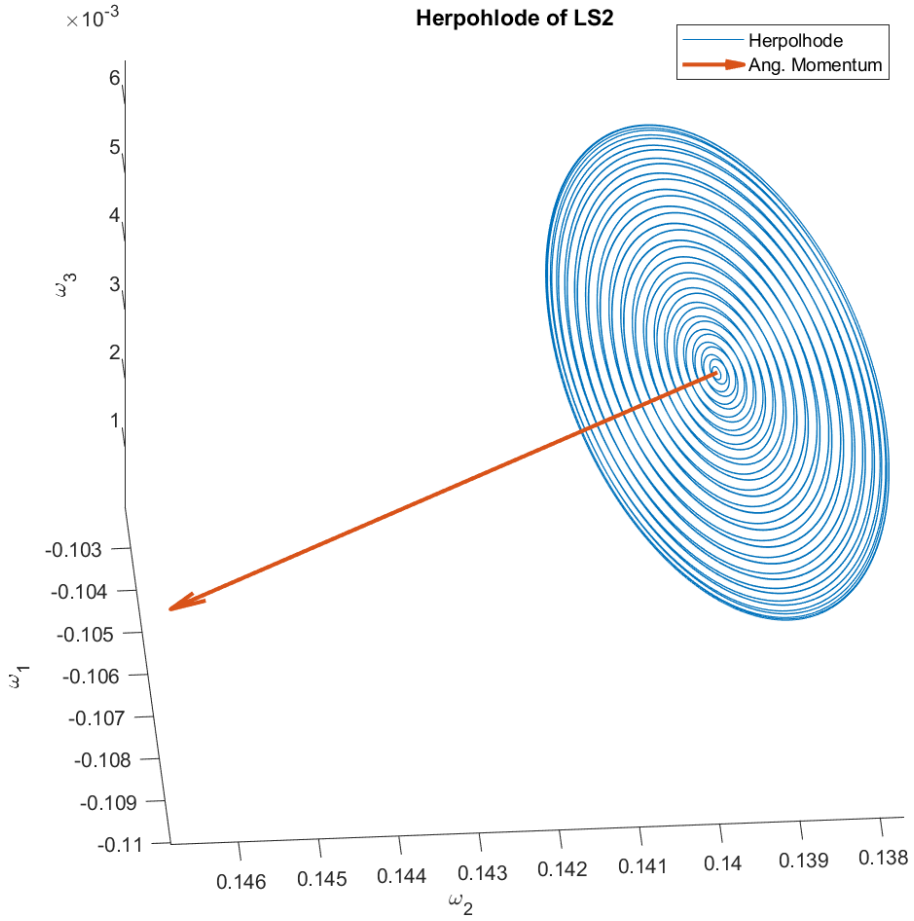

Figure 13: Herpolhode of LS2 spacecraft in plane

In Figs 14 and 15, we can see various coordinate systems of interest (RTN, body, and principal

axes) plotted in time. The former plot places the coordinate triads in the appropriate place in ECI, for visualization of the coordinate system with respect to the orbital motion. The latter show the trace of the coordinate axes' tips, their color changing from the initial color to yellow as time progresses.

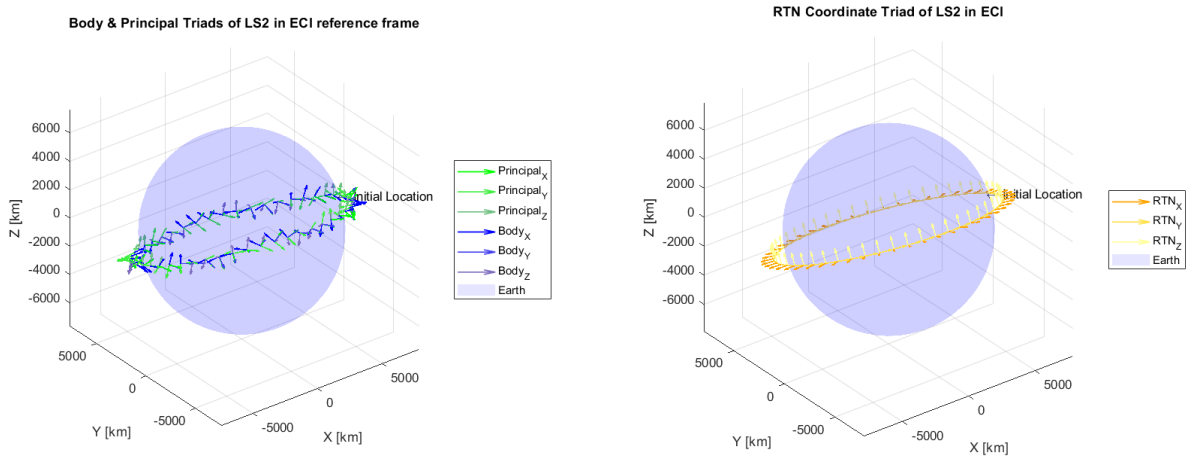

Figure 14: Coordinate triads motion in ECI

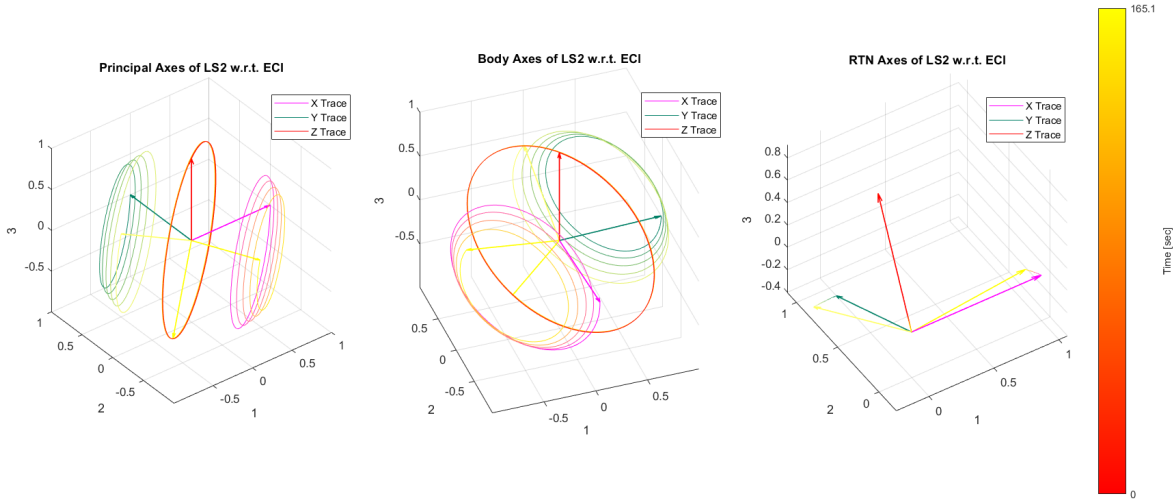

Figure 15: Coordinate triad motion in time

3.3 EQUILIBRIUM TESTS

Placing our initial spin along the principal axis of maximum inertia and assuming that the principal axes initially correspond with the inertial axes, we can test if our attitude propagation maintains stability - we see in Fig 16 that the components of angular velocity remain constant in principal axes, as expected. Converting our quaternion output to 312 Euler angles in Fig 17, we can see that θ and ψ remain constant while ϕ increases linearly (note that the sawtooth shape comes from the angle being wrapped to 2π).

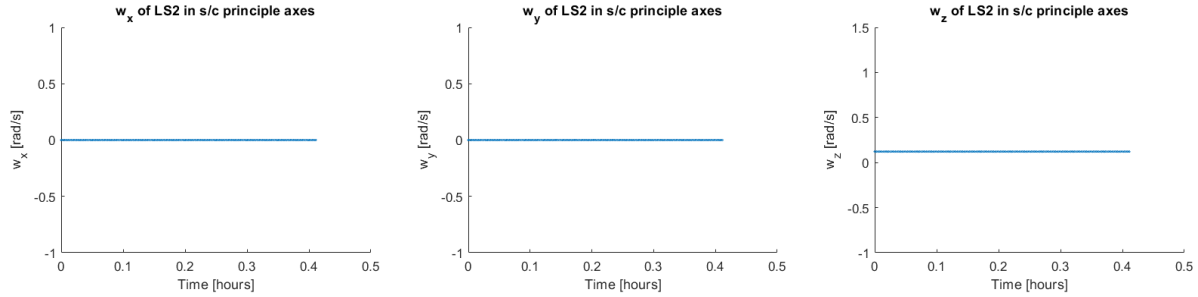

Figure 16: Components of angular velocity for spin along principal Z axis

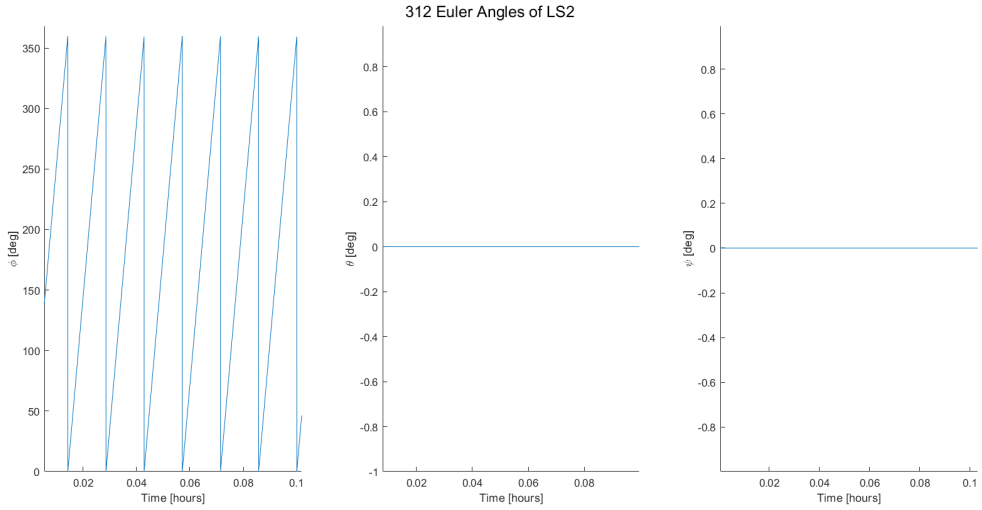

Figure 17: 312 Euler angles for spin along principal Z axis

If we instead assume that our principal axes align with the RTN frame initially, with the angular velocity oriented along the N axis, our angular velocity components once again remain constant (so long as we ignore any orbital perturbations), as seen in Fig 18. This behavior initially may seem strange, as the RTN frame is non-inertial, but with spin around the principal z-axis, our angular velocity is stable; furthermore, the N axis remains constant due to the lack of orbital perturbations (no torques keep the angular momentum vector, $\vec{h}$, constant).

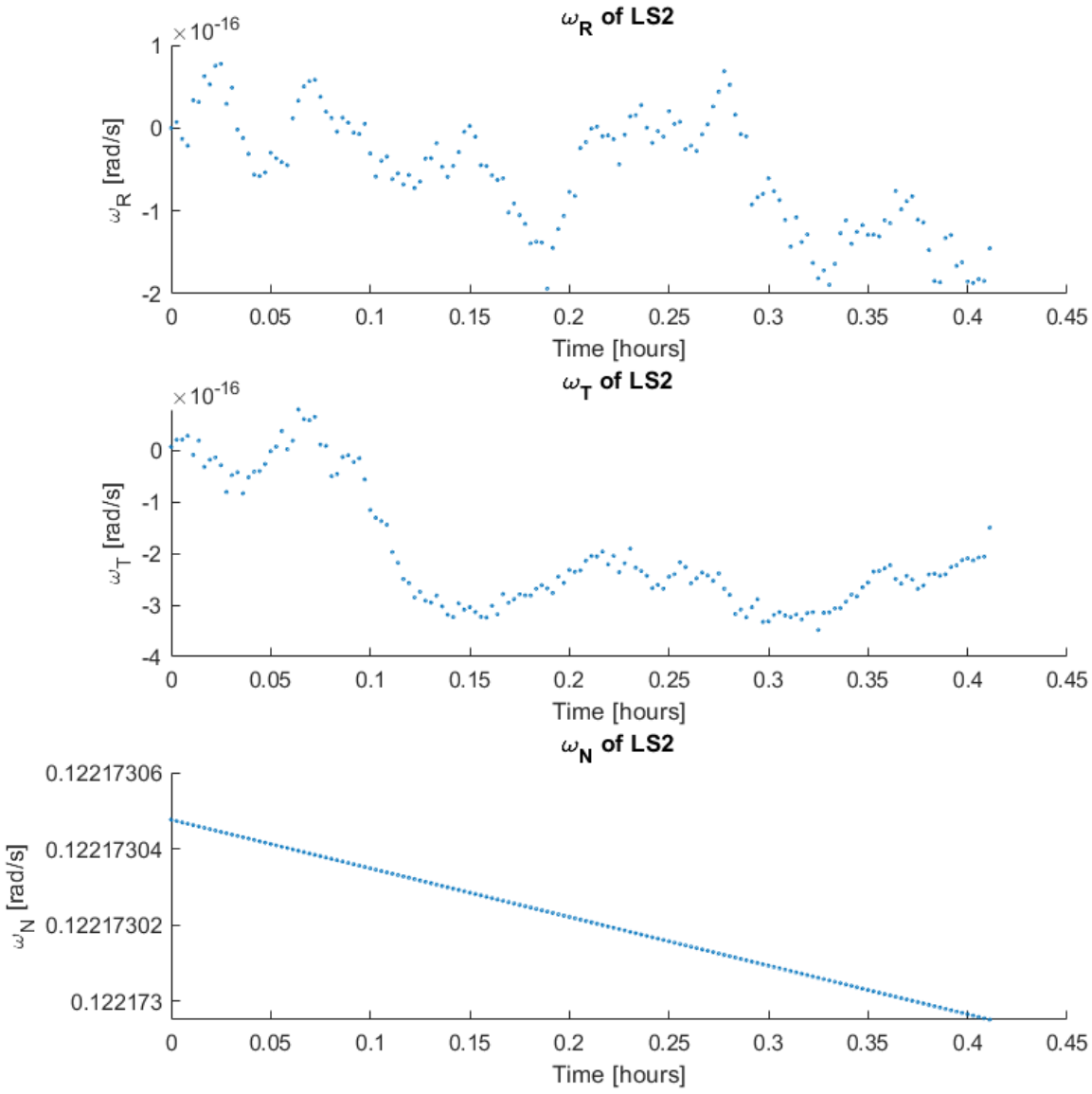

Figure 18: Components of angular velocity in RTN frame, with spin along N axis

3.4 STABILITY TESTS

Once again initially aligning the principal axes with the inertial, we test the stability of spin about the three principal axes with minor pertubations. This effect is generated by providing a spin of 7 deg/s about the principal axis in question, and giving a small spin of 0.01 deg/s about the other two principal axes. The results of these stability simulations (principal-axes angular velocity, momentum, and Euler angles) are provided in Figs 19 - 21 - note that in general, the rapid switching between complementary values for Euler angles is due to the inverse trigonometric functions used in converting from quaternions to 312 Euler angles.

For an initial spin about the X-axis, the axis of least inertia, we see *periodic stability* in angular velocity and instability in angles in Fig 19.

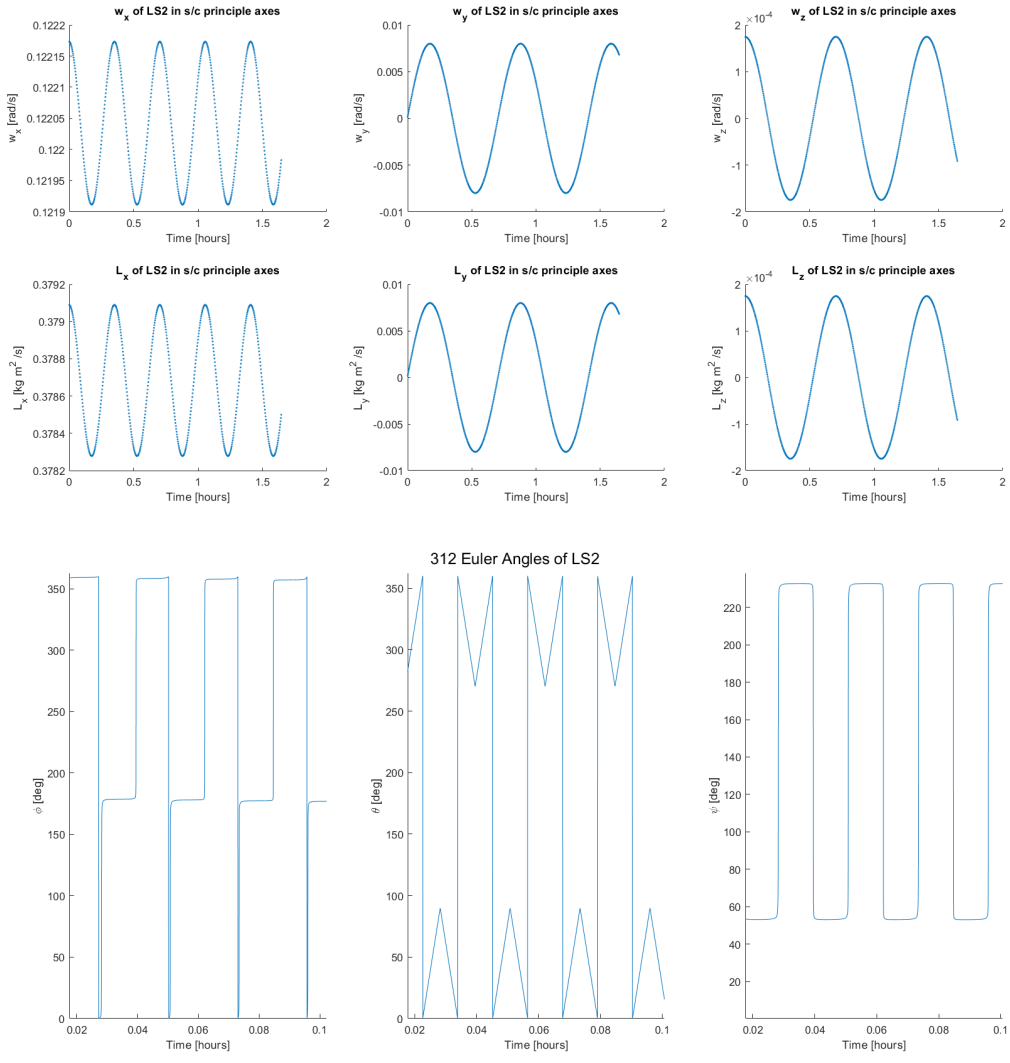

Figure 19: Velocities, angular momentum, and 312 Euler angles for principal X-axis spin.

For an initial spin about the Y-axis, the axis of intermediate inertia, we see *instability* in angular velocity and instability in angles in Fig 20.

For an initial spin about the Z-axis, the axis of maximum inertia, we see *periodic stability* with a much higher frequency in angular velocity and instability in angles in Fig 21.

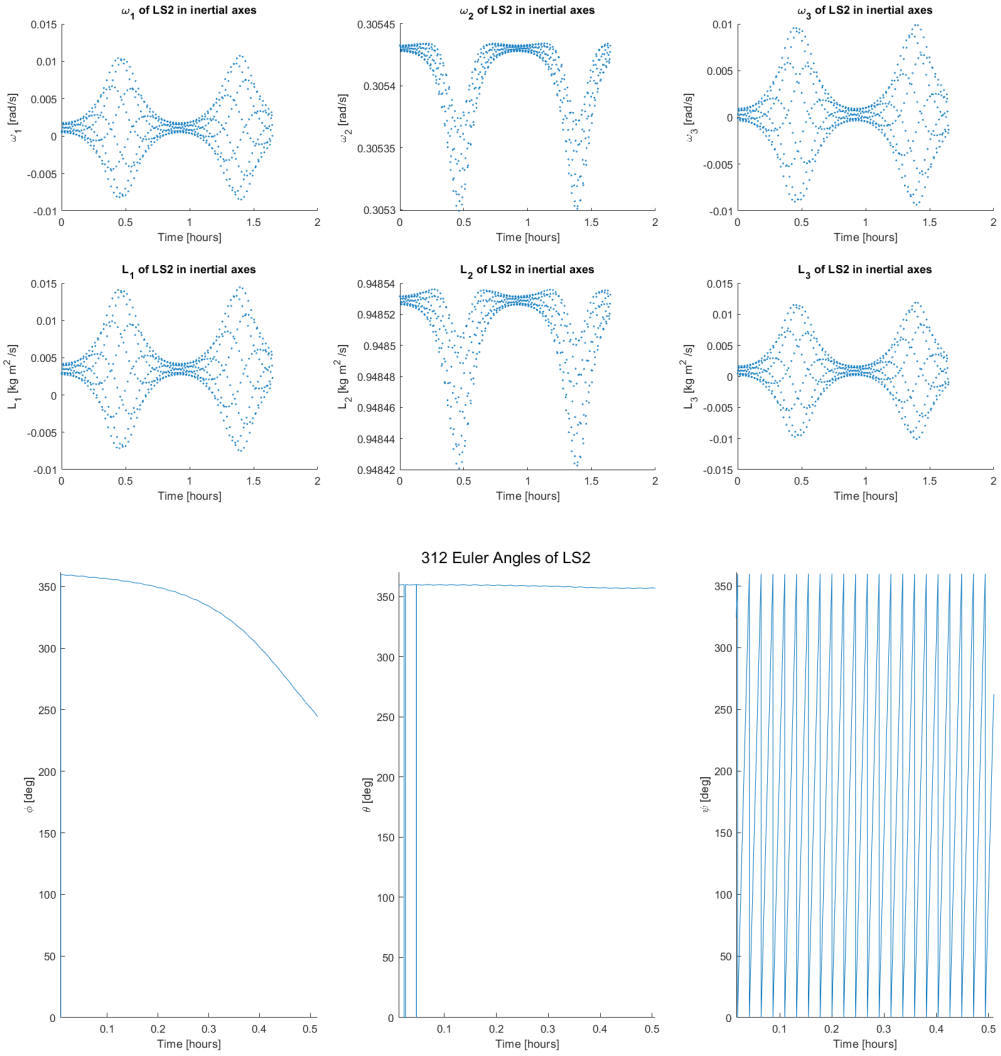

Figure 20: Velocities, angular momentum, and 312 Euler angles for principal Y-axis spin.

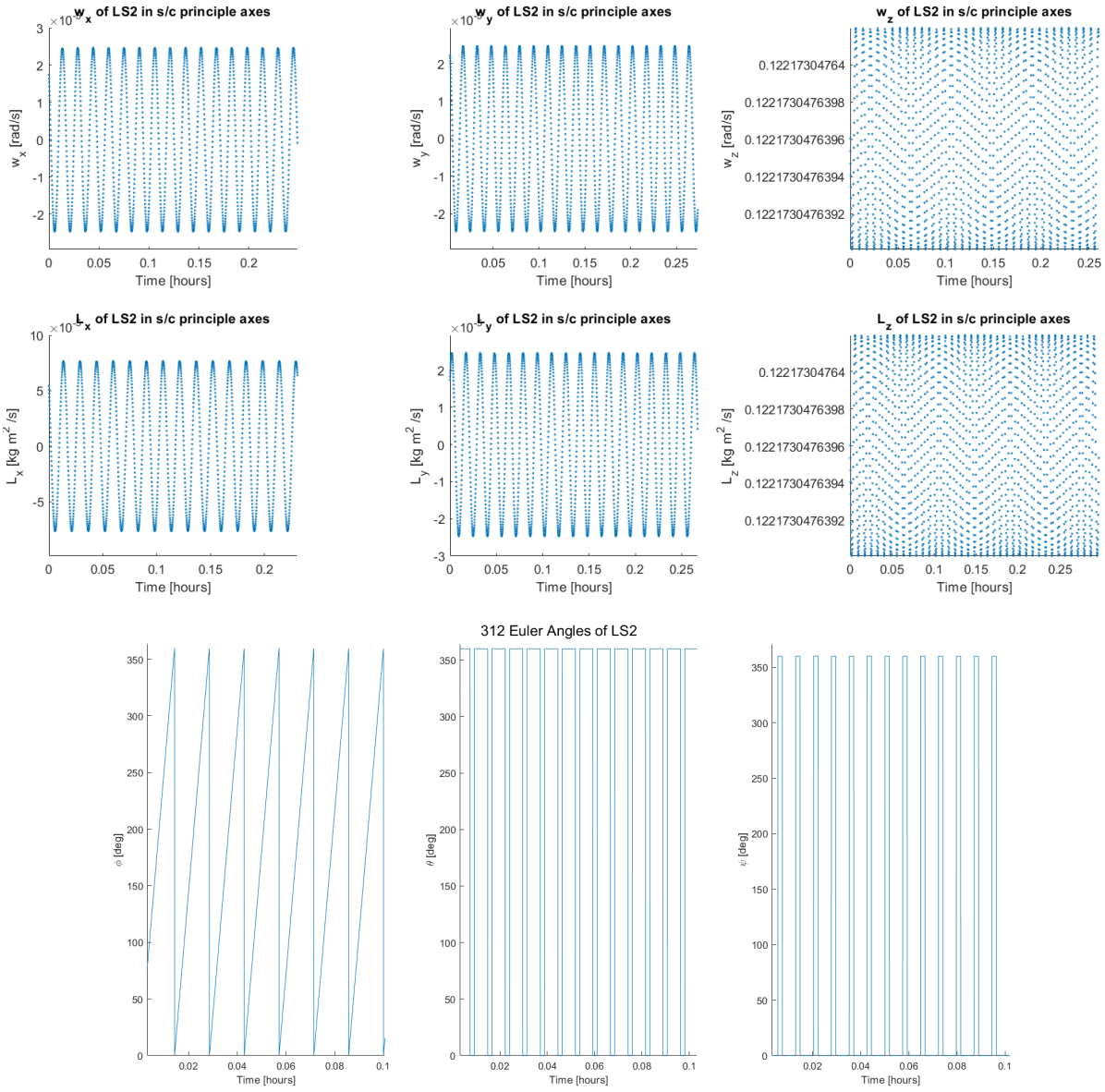

Figure 21: Velocities, angular momentum, and 312 Euler angles for principal Z-axis spin.

4 PROBLEM SET 4

4.1 DUAL SPIN

By adding a momentum wheel into our simulation (as see in Fig 22), we give the spacecraft the capacity to perform maneuvers and ensure stability along an axis of choice. In Appendix G, we validate our new dynamics by testing the equilibrium and stability cases from the previous problem set, but now with an applied angular momentum in the momentum wheel. The data used for our momentum wheel's moment of inertia and maximum spin rate is pulled from the LS2 parts list [7], which indicates that LS2 uses a RW3-0.060 momentum wheel from Sinclair Interplanetary.

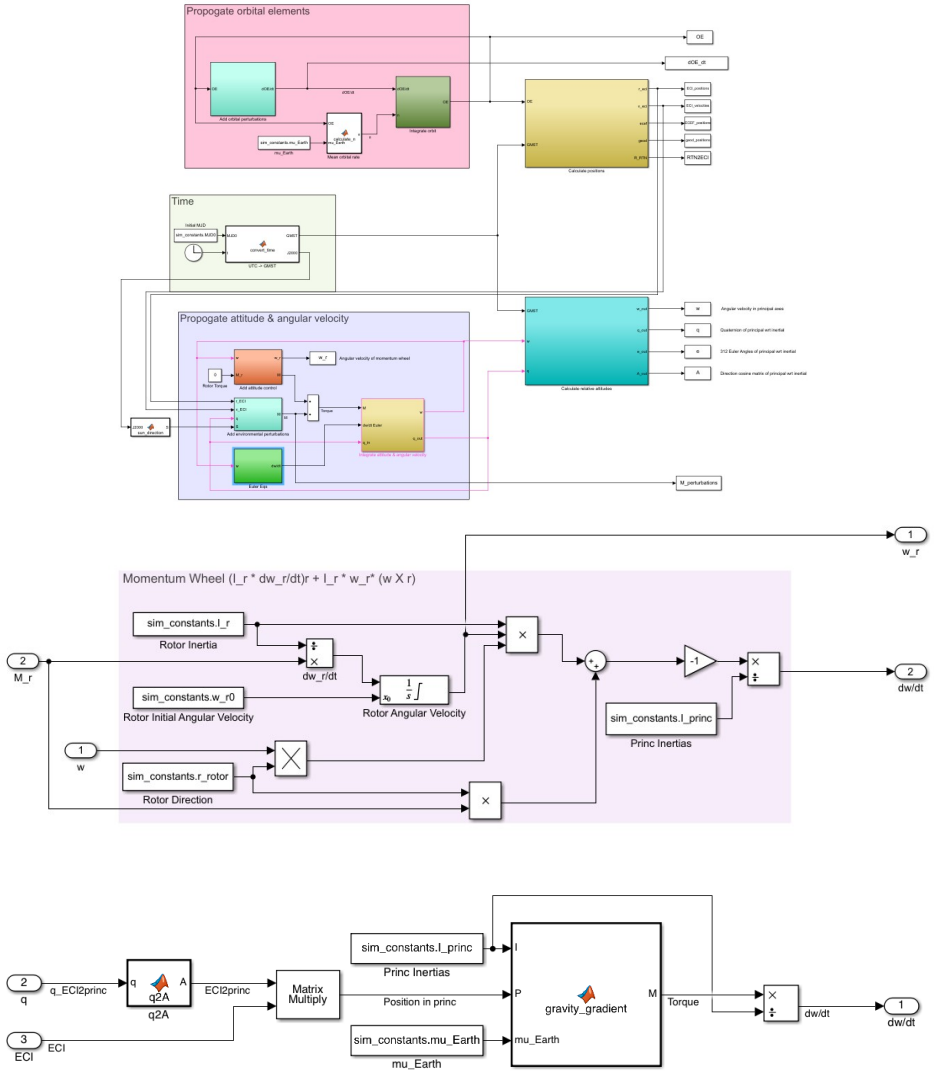

Figure 22: Updated Overview of Simulink Propagator with Momentum Wheel and Gravity Gradient Details

To give stability along our intermediate axis (the principal Y), we can place the rotor's axis along Y and give it a spin such that

$$I_r \omega_r > (I_z - I_y)\bar{\omega}_y$$

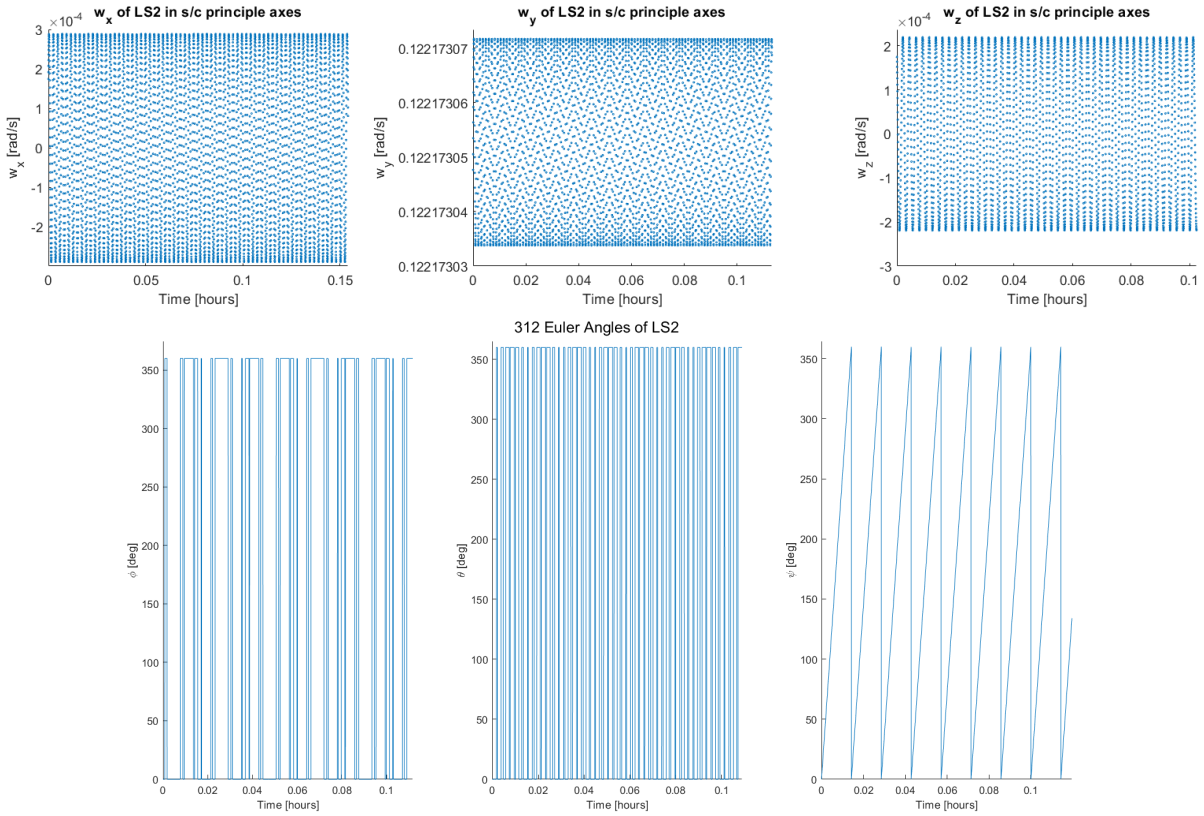

Figure 23: Angular velocity components and 312 Euler angles for intermediate axis spin, with momentum wheel for stability.

where I_r is the rotor's moment of inertia and $\bar{\omega}_y$ is the desired equilibrium spin rate. By setting our initial angular velocity to be equivalent to that used in our Y-axis stability test, we can cross-compare our results. In Fig 23, we can see the resulting inertial-axes angular velocity components and the 312 Euler angles that result from our simulation. Unlike in our stability test for the intermediate axis, we now see that our spin is stable with the added help of a momentum wheel along principal Y axis (note that oscillations in ω_y are very small in magnitude, and that only ψ increases linearly while the other two Euler angles remain near 0° or 360°). This is incredibly useful given that our mission requirements require Y-axis slewing for Sun-pointing, and maintaining stable spin about this axis can help to prevent tumbling.

We can additionally attempt to ensure stability about the principal Z axis without spinning the spacecraft about the Z axis. This would be useful directly before Y axis slew maneuvers, allowing a precise understanding of how momentum wheel changes will change the inertial alignment of the Z axis. Giving the spacecraft an initial angular velocity of 0.01 deg/s about each principal axis, we put the momentum wheel axis along Z and spin it to 100 rad/s (with such a small Z spin, just about any non-trivial momentum wheel spin will suffice to ensure stability). The results of this trial can be seen in Fig 24 - note that just as in our stability test with spin primarily along the Z axis, we see periodic stability of the spacecraft angular velocity but without significant Z spin!

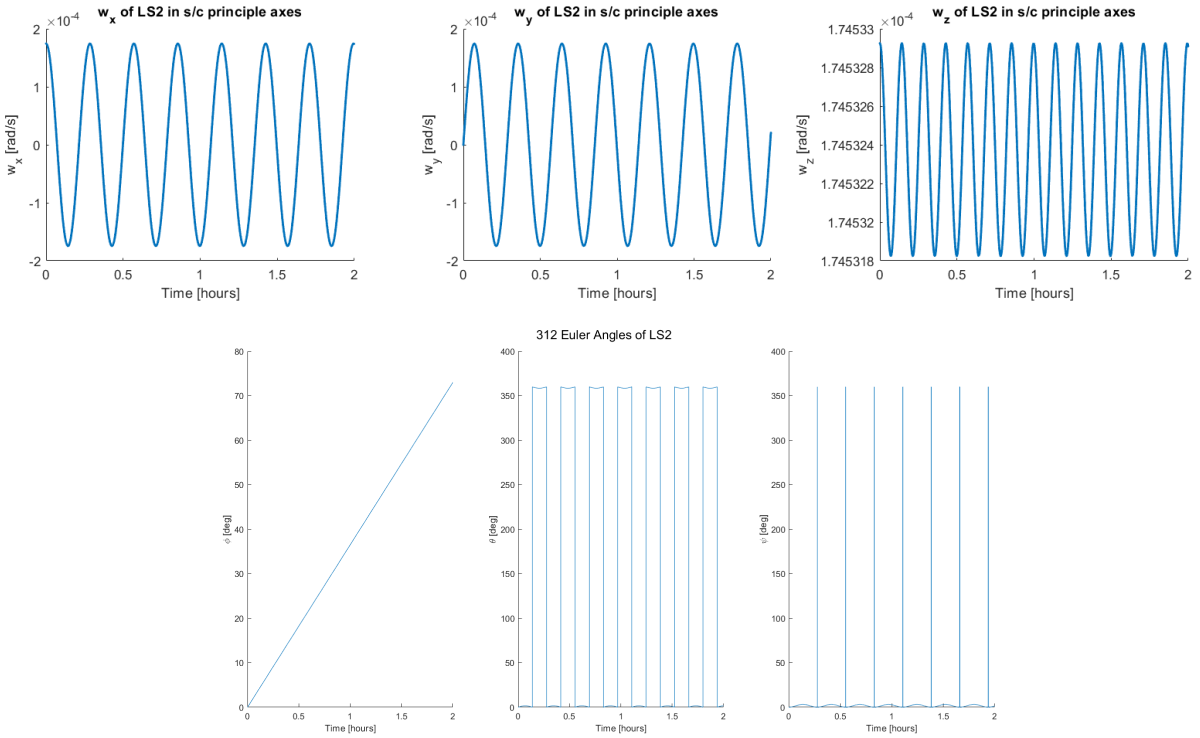

Figure 24: Angular velocity components and 312 Euler angles for low spin, with momentum wheel for Z stability.

4.2 GRAVITY GRADIENT TORQUE

The spacecraft torque due to a gravity gradient is modeled using Eq. 4 (included within the "Add environmental perturbations" block as seen in Fig 22).

$$\vec{M} = \frac{3GM}{R^3} \begin{bmatrix} (I_z - I_y)c_y c_z \\ (I_x - I_z)c_z c_x \\ (I_y - I_x)c_x c_y \end{bmatrix} \tag{4}$$

Using $a_0 = 7080.6$ km in an arbitrary direction not aligned with the RTN frame, a back-of-the-envelope calculation yields gravity gradient torques on the order of 10^{-6} in Y, Y and 10^{-9} in Z. When simulated with the same initial conditions as in Section 3.2, we see torques that match this calculation (Fig. 26).

To assess gravity gradient stability, we plot the spacecraft's moment of inertia coefficients K_i against regions of stable (white) and unstable gravity gradient torque in Fig. 25. LS2 can be oriented such that it is just barely within the stable region (top right corner). However, because of its proximity to the stability limit, small perturbations are enough to create a gravity gradient instability. The stability of the various configurations is assessed in Appendix H. Further, because the target attitudes are with respect to the sun and not Earth-pointing, the satellite will not often be in a stable configuration, so the gravity gradient torque must be actively compensated for.

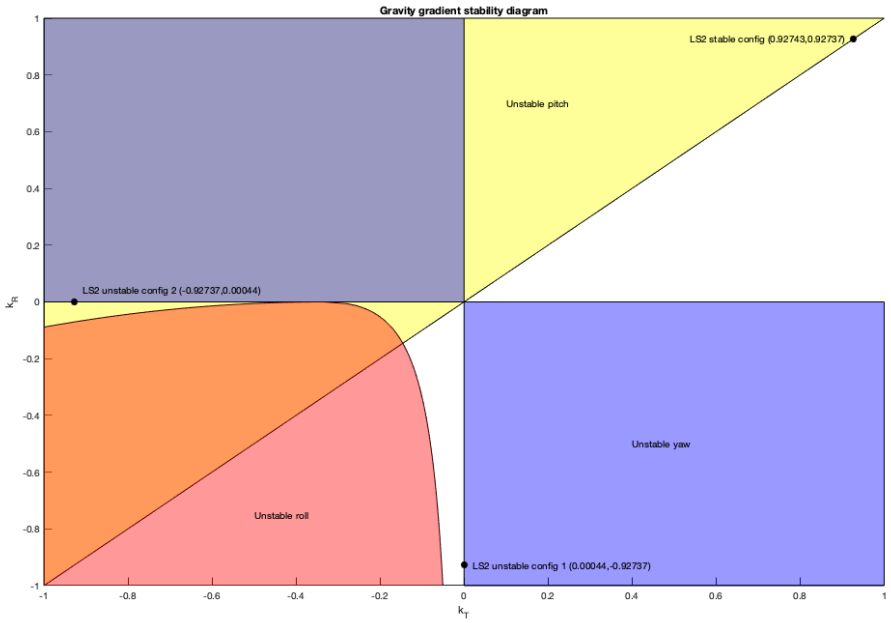

Figure 25: Assessment of spacecraft configurations that lead to stable and unstable gravity gradient torques based on LS2's mass properties.

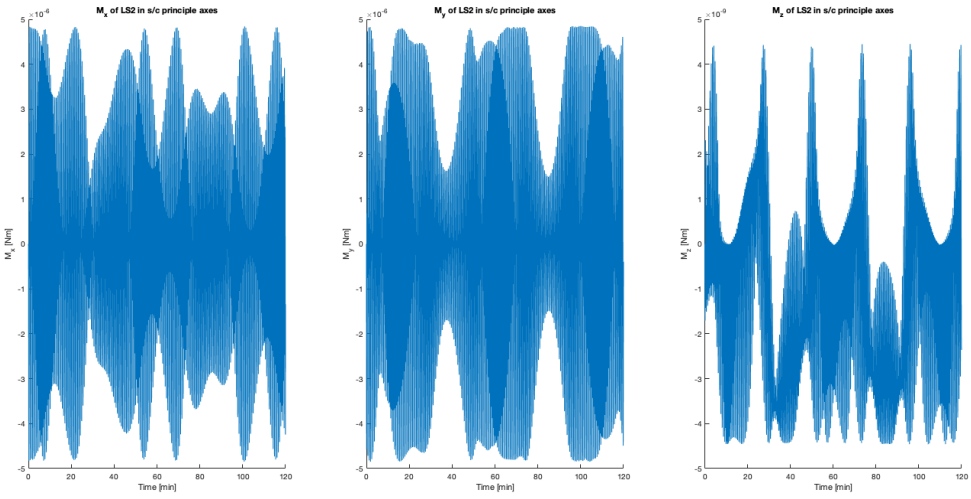

Figure 26: Torques on spacecraft principal axes due to gravity gradient.

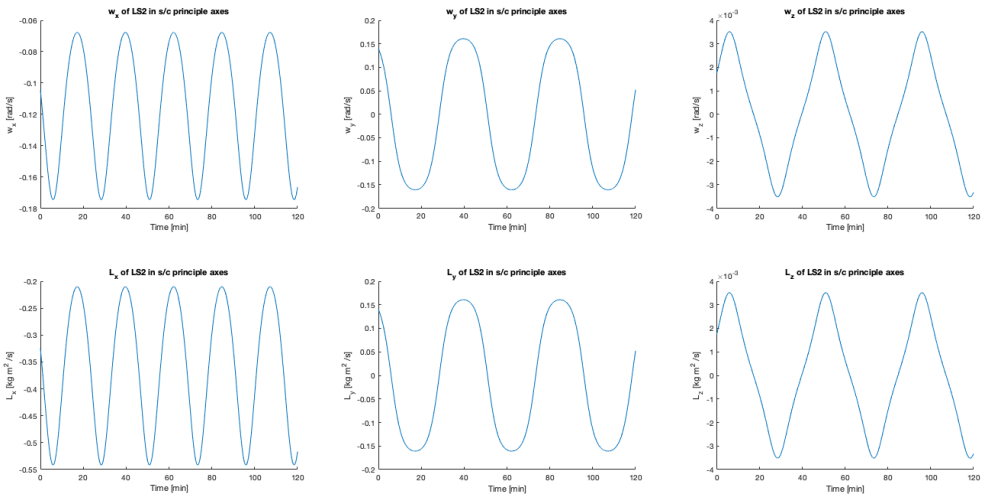

Figure 27: Angular velocity, momentum spacecraft principal axes due to gravity gradient.

5 PROBLEM SET 5

5.1 PERTURBATIONS

To include further environmental attitude disturbances, we implement torques as a result of solar radiation pressure (SRP), aerodynamic drag, and magnetic torque. The output of all environmental perturbation blocks is summed into a perturbation torque, which is subsequently fed into the Euler equations.

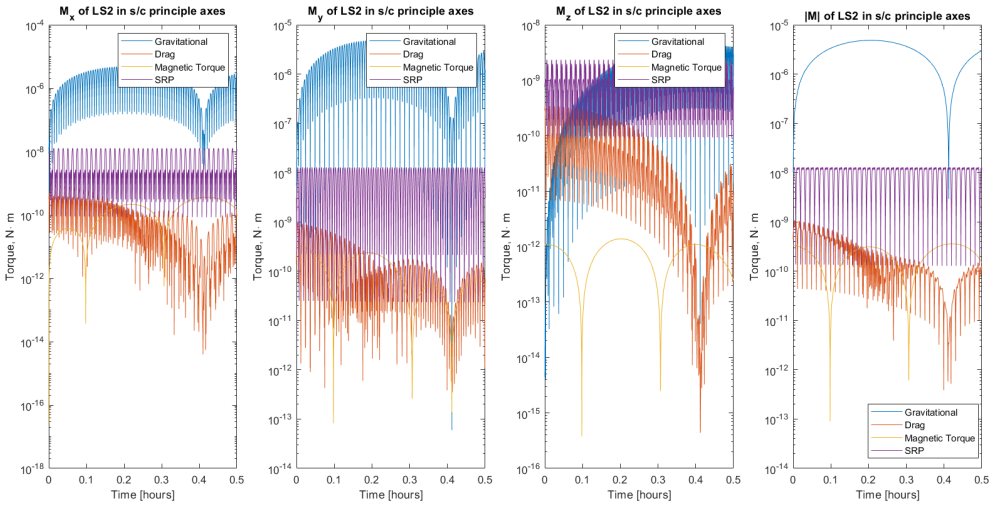

Figure 28: Comparison of disturbance torque magnitudes.

In Fig 28, we plot the logarithm of the torque magnitudes for relative comparison and validation using the conservative estimates from Chapter 11 of Larson & Wertz's Space Mission Analysis and Design (SMAD) [6]. The computed conservative estimates from Wertz's analysis are provided below in Table 7. Note that while the gravity gradient and magnetic torque estimates are very close to our calculated values, our simulated values of SRP and aerodynamic drag are much lower than the estimated value from SMAD. After checking our simulation, it seems likely that this discrepancy is due to the fact that the majority of the area used in calculating the conservative estimates is contributed by the solar sail. However, the solar sail does not have a very large moment arm for most attitudes, greatly reducing the effective areas.

Disturbance	Max. Simulated Torque, $N \cdot m$	SMAD Estimate, $N \cdot m$
Aero. Drag	$1E-9$	$1.4E-6$
Gravitational	$4E-6$	$4.2E-6$
Magnetic	$2E-10$	$1.9E-10$
SRP	$2E-8$	$2.9E-5$

Table 7: Comparison of simulated torque values to conservative estimates from SMAD [6].

5.2 ATTITUDE TARGETING & CONTROL ERROR

To be able to quantify our attitude error, we must define a target attitude. In line with mission requirements, we want our orientation to provide SRP thrust when moving away from the Sun, and want to minimize SRP effects when moving towards the Sun. Furthermore, we set our body Y-axis to always lie normal to the orbital plane, in line with the orbital angular momentum

vector. When flying away from the Sun, placing our body $-Z$-axis along the Sun-pointing vector projected into the orbital plane provides in-plane solar sail thrusting. When flying toward the sun, we place our body X-axis along the Sun-pointing vector projected into the orbital plane to minimize cross-sectional area normal to the Sun direction. With this full definition of our target attitude, we can quantify the attitude control error for later implementation in active attitude control.

We define the attitude error direction cosine matrix (DCM), which we call A_{err} as

$$A_{ECI\rightarrow princ,target} = A_{err} A_{ECI\rightarrow princ,actual} \tag{5}$$

where $A_{ECI\rightarrow princ,target}$ is the desired rotation matrix to achieve target attitude and $A_{ECI\rightarrow princ,actual}$ is the actual rotation matrix of the satellite. We can solve this equation to see that

$$A_{err} = A_{ECI\rightarrow princ,target} A^{T}_{ECI\rightarrow princ,actual}$$

The resulting A_{err} matrix maps a vector in principal coordinates from its actual position to the desired, target position.

We verify the functionality of our attitude control system by turning off perturbations (both orbital and attitude) and setting our desired orientation to be identical to principal coordinates ($A_{ECI\rightarrow princ,target} = I$). Initially, our satellite's principal axes are aligned with the inertial frame and the spacecraft spins at 5 deg/s about its principal Z axis. A comparison of the resulting actual Euler angles and corresponding target and error angles is provided in Fig 29. Note that ϕ attitude and error angles are exactly opposite, as expected (the inverse rotation would need to be applied to reach the target, $\phi = 0$).

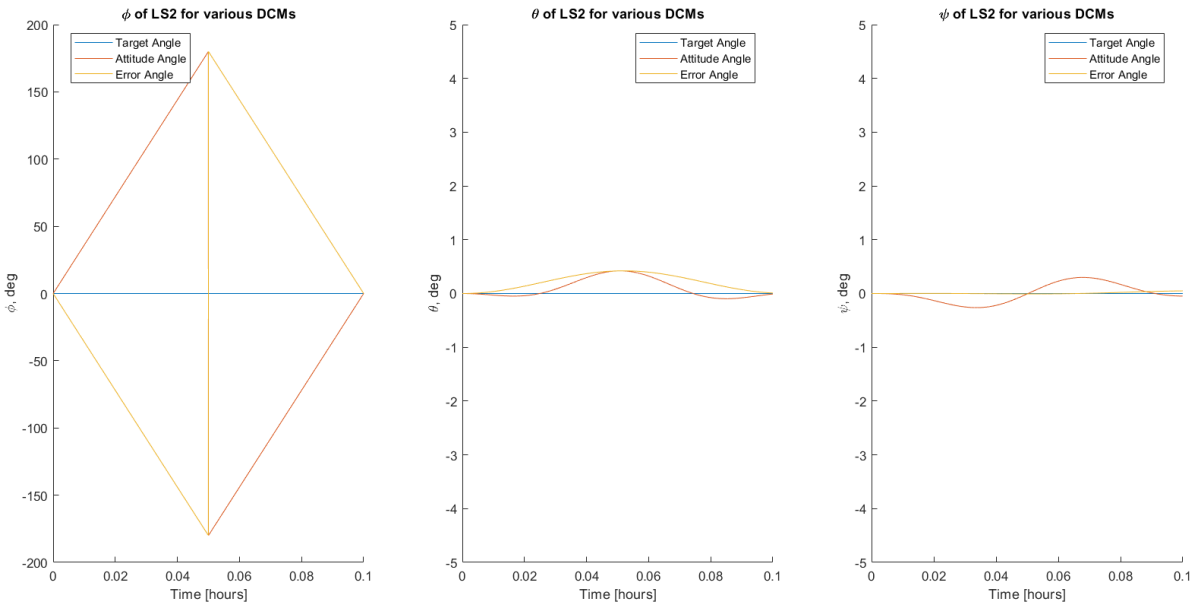

Figure 29: Euler angles, target, and error for target attitude identical to inertial frame, Z axis spin.

If we instead turn attitude perturbations on, keeping our target attitude to be the inertial reference system but with the satellite initially at rest, our resulting angular errors are purely a result of perturbative torques. The error angles provided in 30 represent the necessary rotation to take the satellite from its current attitude to the desired attitude.

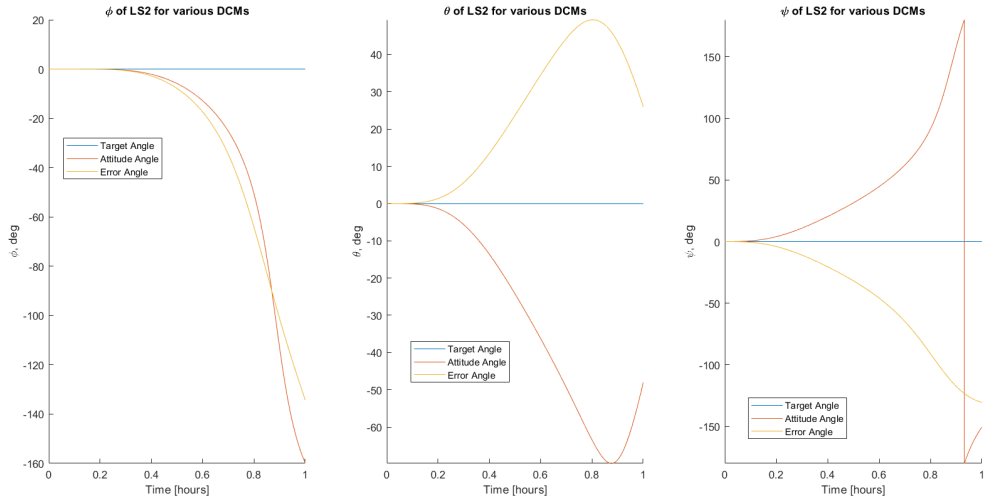

Figure 30: Euler angles, target, and error for target attitude identical to inertial frame, no initial spin with environmental perturbations.

6 PROBLEM SET 6

6.1 ATTITUDE DETERMINATION FROM SENSOR DATA

For our spacecraft, as discussed previously, we assume two sets of sensors that each produce a single vector measurement. Aboard LS2, a collection of 5 sun sensors measure the azimuth and elevation of sunlight in their respective fields of view. At any time, two or three sun sensors are able to generate measurements, and their data are transformed into the S/C body axes and fused to calculate an average Sun direction vector. Additionally, three orthogonal magnetometers provide a measurement of the magnetic field in the spacecraft body frame. Furthermore, a set of gyroscopic sensors provide measurements of angular rotation rates. In our simulation, we use the "ground truth" given by the propagator developed in previous problem sets to create measurements - in the next section, we discuss how we add random noise to these measurements to make the system realistic.

Before implementing sensor noise, however, we develop our attitude estimation tools to ensure functionality - by comparing the results of our attitude estimation with the ground truth, including zero sensor noise, we can verify that the spacecraft's estimation matches the propagator truth. For a set of measurements in the principal frame, $\vec{M}$, and a set of corresponding modeled vectors in ECI, $\vec{V}$, we implemented three attitude determination methods:

- **Deterministic method** - the estimated attitude is calculated directly from the measurements, $A = MV^{-1}$.
- **q-method** - the estimated attitude is determined using the q-method, which minimizes the least-squares error between a measurement and its corresponding, rotated model vector. Though this method allows sensor weighting, we give all measurements in $\vec{M}$ equal weighting.
- **Angular velocity kinematics** - the estimated attitude is integrated using quaternion kinematics and gyroscopic measurements of the current angular velocity.

Our $\vec{M}$ and $\vec{V}$ matrices are generated using our measured Sun vector in the principal axes, $\vec{S}_{meas}$, the measured magnetic field vector, $\vec{B}_{meas}$, and their corresponding model vectors in ECI (taken from the ground truth), $\vec{S}_{ECI}$ and $\vec{B}_{ECI}$. Given that the magnetometer readings have lower error, we generate our 3x3 matrices as

$$\vec{M} = \begin{bmatrix} | & | & | \\ \vec{p}_{meas} & \vec{q}_{meas} & \vec{r}_{meas} \\ | & | & | \end{bmatrix}$$

and

$$\vec{V} = \begin{bmatrix} | & | & | \\ \vec{p}_{ECI} & \vec{q}_{ECI} & \vec{r}_{ECI} \\ | & | & | \end{bmatrix}$$

where $\vec{p} = \vec{B}$, $\vec{q} = \frac{\vec{p}\times\vec{S}}{|\vec{p}\times\vec{S}|}$, and $\vec{r} = \vec{p} \times \vec{q}$.

In Fig 31, we see the q-method and the integrated angular velocity attitude estimations compared to the ground truth in the absence of sensor error. As expected, they agree very closely (note the minor deviation seen in the q-method is likely due to a near-singular matrix, resulting in larger errors in the computation of eigenvalues). The deterministic method, though not included in this plot, concurs exactly with the q-method in the absence of sensor error.

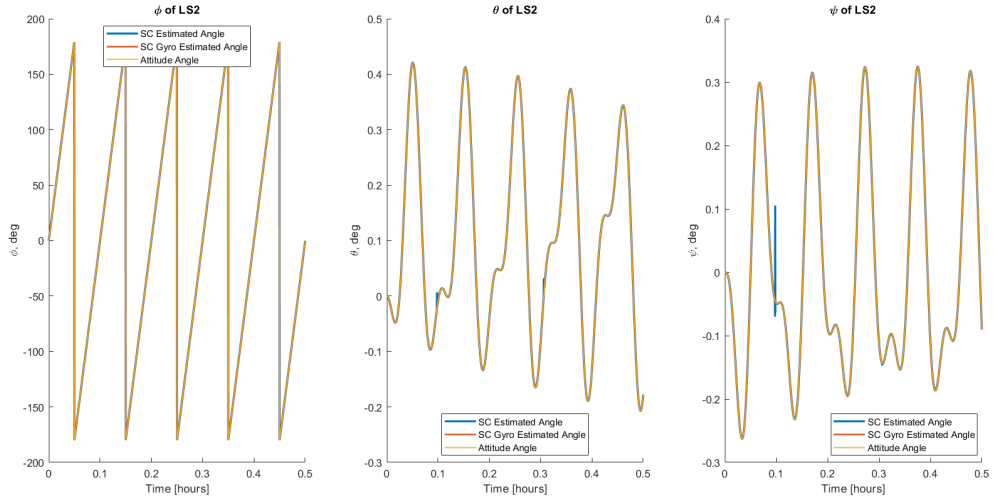

Figure 31: Comparison of q-method and gyroscope attitude estimates without sensor noise.

6.2 SENSOR NOISE

Sensor noise, based on the values in Table 2, was modelled by adding Gaussian white noise to each sensor measurement vector. For the sun sensors, which measure sun direction in azimuth and elevation, independent noise components are added to the true azimuth and elevation, then transformed to Cartesian for the reported sun direction measurement. For the magnetometer, the noise components in each axis are used to construct a 3-1-2 Euler angle rotation matrix that is then applied to the magnetic field direction vector.

The variance of the noise is calculated from the reported errors, e_{max} as $\sigma^2 = \frac{e_{max}}{\sqrt{3}}$, so that $> 99\%$ of errors fall within e_{max}. Further, a small, constant bias is added, $\approx e_{max}/10$ on each axis. The noise is seeded to enable repeatable simulations.

In Fig 32, we see the comparison of our q-method and deterministic attitude estimates with the ground truth after the addition of sensor noise. Fig 33 shows the error rotation between the q-method and the true estimate (note that the error for the deterministic method is very close to that of the q-method). The results show noisy measurements that oscillate ± 2 deg around the true attitude. In Fig 34, we see the comparison of the angular velocity estimate to the ground truth - note that the estimated attitude from gyroscopic measurements deviates severely from the true attitude. This is expected, as the integration of error accumulates as the simulation continues.

Additional analysis of deterministic attitude estimate and its comparison to the q-method are provided in Appendix I, including an analysis of the effect of "error distribution" techniques that seek to reduce error effects by averaging measurements.

6.3 SMALL SENSOR ERRORS

The sensor error DCM respresents a rotation of sensor measurements from their "true" measurement due to sensor noise and bias. Because of this error, the attitude estimate will be rotated slightly from the true attitude. We define it as the rotation from the actual orientation to the believed orientation, so that:

$$A_{ECI \to princ,est} = A_{sens.err} A_{ECI \to princ,actual} \tag{6}$$

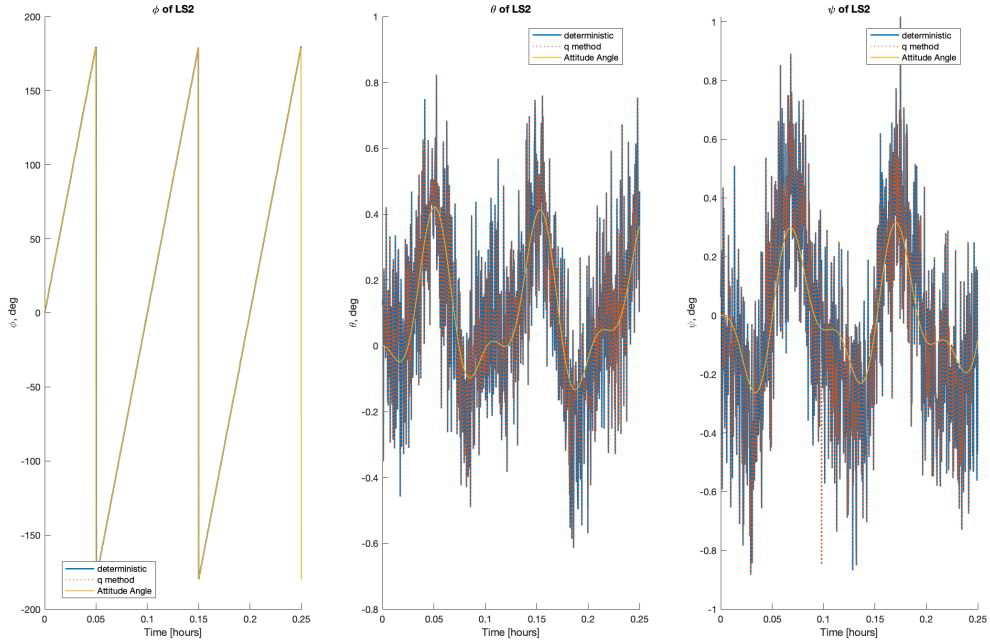

Figure 32: Comparison of q-method and deterministic attitude estimates with added sensor noise.

For an error DCM with small values, we note that this corresponds to a small rotation. For our 312 Euler angles, a small rotation error would produce an error DCM that looks like:

$$A \approx \begin{bmatrix} 1 & \phi & -\psi \\ -\phi & 1 & \theta \\ \psi & -\theta & 1 \end{bmatrix} \tag{7}$$

Clearly, given small ψ, θ, and ϕ, this matrix is nearly equivalent to the identity matrix, with the off-diagonal elements indicating the magnitude of the error rotation angles.

For a quaternion, which can be expressed in terms of 312 Euler angles as

$$q = \begin{bmatrix} \cos(\phi/2)\sin(\theta/2)\cos(\psi/2) + \sin(\phi/2)\cos(\theta/2)\sin(\psi/2) \\ \cos(\phi/2)\cos(\theta/2)\sin(\psi/2) - \sin(\phi/2)\sin(\theta/2)\cos(\psi/2) \\ -\cos(\phi/2)\sin(\theta/2)\sin(\psi/2) + \sin(\phi/2)\cos(\theta/2)\cos(\psi/2) \\ \cos(\phi/2)\cos(\theta/2)\cos(\psi/2) + \sin(\phi/2)\sin(\theta/2)\sin(\psi/2) \end{bmatrix}, \tag{8}$$

we note that the small angle approximation (throwing away terms with more than one angle) gives

$$q \approx \begin{bmatrix} \theta/2 \\ \psi/2 \\ \phi/2 \\ 1 \end{bmatrix}, \tag{9}$$

Thus, the vector component of the quaternion is directly proportional to Euler angles. Therefore, we can consider the off-diagonal elements of our error DCM or, alternatively, the vector component of our quaternion output (from our q-method, for example) to quantify the small Euler angles that rotate our estimated frame to the actual attitude.

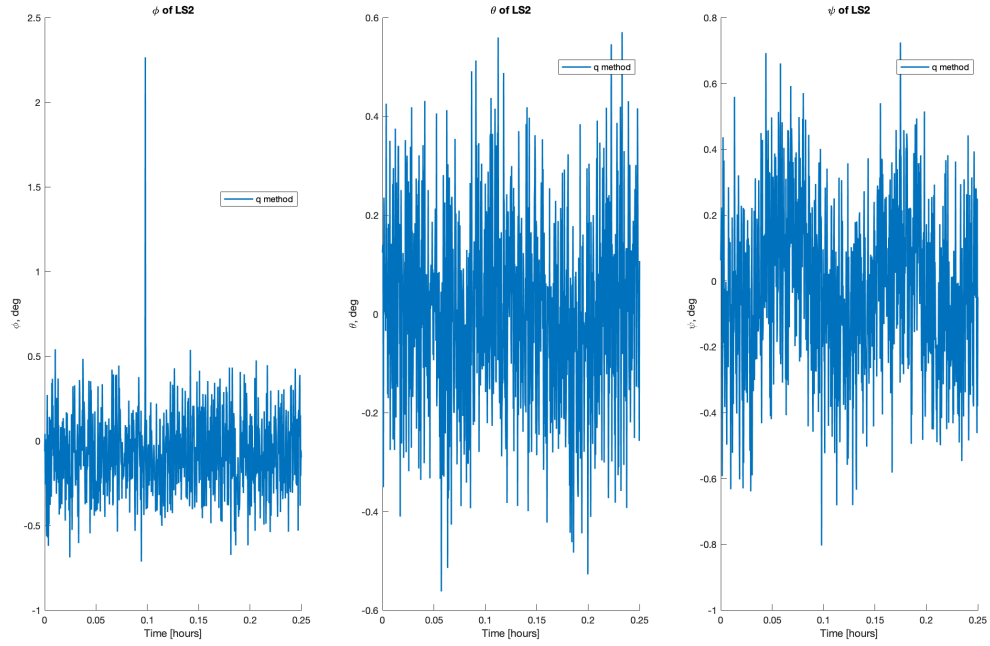

Figure 33: Error of q-method with respect to the true attitude.

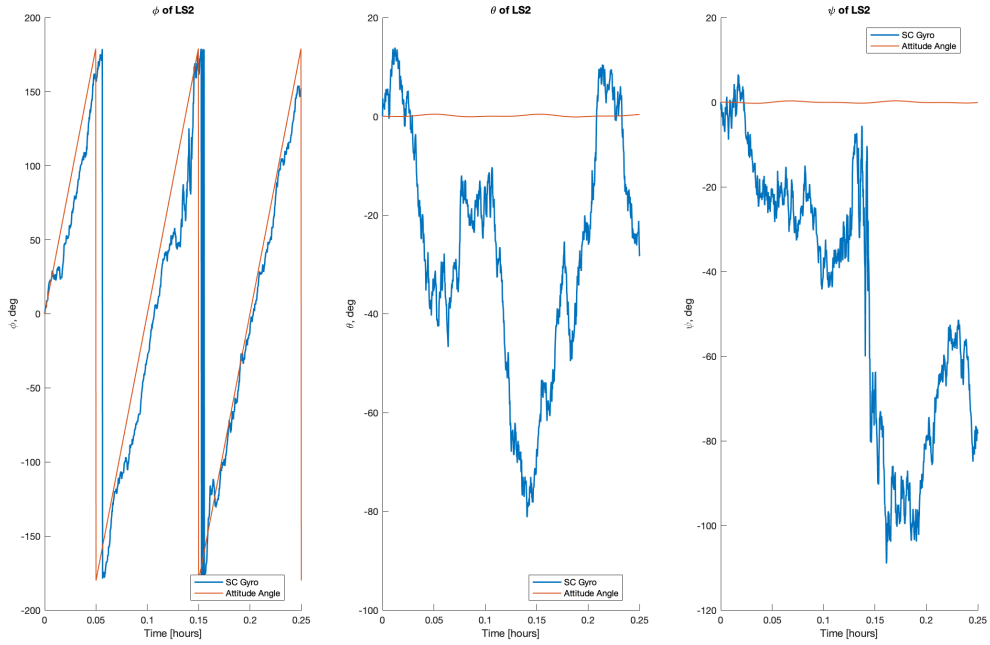

Figure 34: Integrated gyroscope estimation with sensor noise.

6.4 ESTIMATING ATTITUDE CONTROL ERROR

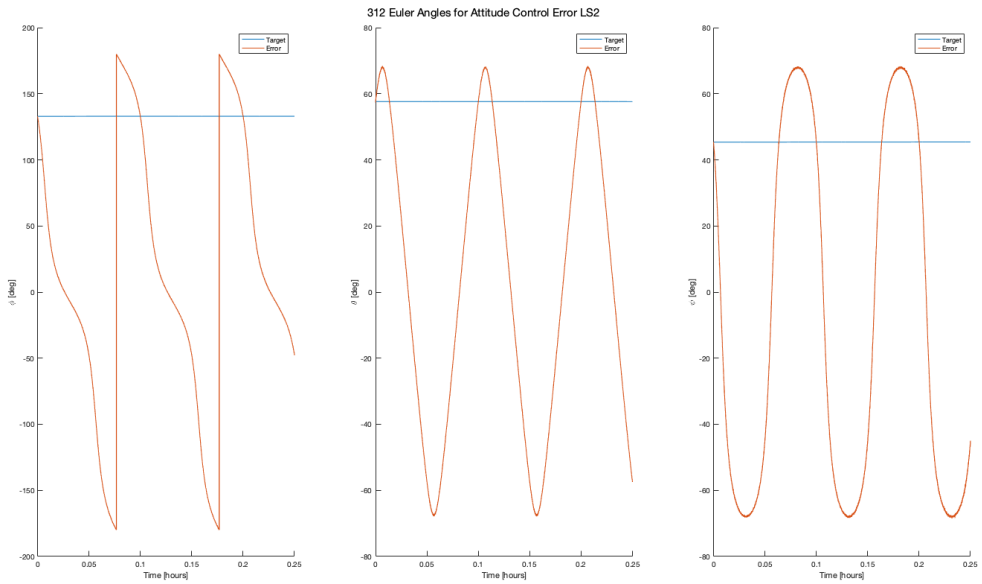

Figure 35: Attitude control error using estimated attitude from noisy data (using q-method).

Similar to how we have defined the target error in Section 5, this estimated target error represents the rotation (in principal axes) from the estimated spacecraft attitude to the desired, target attitude. Instead of $A_{ECI\rightarrow princ,target} = A_{err}A_{ECI\rightarrow princ,actual}$, we have

$$A_{ECI\rightarrow princ,target} = A_{err,est}A_{ECI\rightarrow princ,est}$$

and thus

$$A_{err,est} = A_{ECI\rightarrow princ,target}A^T_{ECI\rightarrow princ,est}$$

If $A_{ECI\rightarrow princ,est} = A_{sens.err}A_{ECI\rightarrow princ,actual}$, then

$$A_{err,est} = A_{ECI\rightarrow princ,target}(A_{sens.err}A_{ECI\rightarrow princ,actual})^T = A_{ECI\rightarrow princ,target}A^T_{ECI\rightarrow princ,actual}A^T_{sens.err}$$

We have plotted our resulting attitude control error in 35, with sensor noise included - note that the sensor noise is very small, and noise is barely visible on macroscopic contours of the attitude curves.

7 PROBLEM SET 7

7.1 UPDATED SENSOR MODELS

To further increase model fidelity, the magnetometer model was updated to add the independent noise components to each axis, rather than creating a rotation matrix, which was unnecessarily complex. The sun sensor noise, added to the azimuth and elevation of the sun direction vector, was determined to be fairly precisely modelled, and thus was not changed. In the previous section, once noise was added to the sun sensor, the measurement was transformed to Cartesian for deterministic and q-method attitude estimation. However, for the Extended Kalman Filter in this section, the sun sensor measurements are used directly in azimuth and elevation.

7.2 EXTENDED KALMAN FILTER IMPLEMENTATION

To improve our estimate of current state aboard the spacecraft, we implement an Extended Kalman Filter (EKF) to estimate key attitude state parameters. A full derivation of the associated non-linear functions and their linearizations for implementation is available in Appendix J. Note that we offer two formulations in this derivation: a state representation including sensor bias estimates and another without sensor biases. The latter is simply a subset of the former, and represents a very similar system. Based on the modification of our sensors discussed in the previous section, we define our measurement error matrix, R, to simply be the diagonal matrix with our associated sensor covariances along the diagonal (these same covariances are used to generate the Gaussian sensor noise in our simulation).

$$R = \begin{bmatrix} 7.6 \times 10^{-3}\ \mathbf{I}_3\ \text{rad}^2/\text{sec}^2 & \mathbf{0}_{3\times3} & \mathbf{0}_{3\times2} \\ \mathbf{0}_{3\times3} & 2.5 \times 10^{-13}\ \mathbf{I}_3\ \text{Tesla}^2 & \mathbf{0}_{3\times2} \\ \mathbf{0}_{2\times3} & \mathbf{0}_{2\times3} & 6.854 \times 10^{-4}\ \mathbf{I}_{2\times2}\ \text{rad}^2 \end{bmatrix} \tag{10}$$

We also add process noise to our system, such that the process noise matrix Q is a diagonal matrix whose diagonal components are equal to $0.1\delta t$, for a simulation time step of δt (in our case, we use 0.1 seconds).

Note in our derivation that we implement the full non-linear EKF, not the linearized Kalman Filter associated with our system. This means that when possible, we use the full non-linear functions to assess our expected measurements and state predictions. We test our EKF using simulation data identical to that from the last problem set - with attitude perturbations turned off, we initially align the spacecraft with the principal axes and spin it about the Z axis at 3 deg/s. Our initial state estimate is somewhat poor, estimating our initial quaternion as $(0, 0.5, 0, 0.866)^T$ compared to the true value $(0, 0, 0, 1)^T$ and our initial angular velocity as $(0.1, 0.1, 2.5)^T$ deg/s compared to the true value of $(0, 0, 3)^T$ deg/s (bias estimates, when included in the analysis below, are initially estimated to be zero). Our initial covariance estimate, P, is accordingly taken to be somewhat large, initialized as a diagonal matrix with a value of 4 along the diagonal (giving a 95% confidence interval of $\approx \pm 4$).

7.3 EKF WITH SENSOR BIAS

After implementing the formulation of the EKF with sensor bias included in the state estimation, our tests showed some rather severe issues. While angular velocity measurements behave in a fairly expected manner, the estimates of bias in the azimuth and elevation measurements of our Sun sensor run away. This causes severe issues in our attitude estimation. These results are provided in Figures 36-**??**. At this moment, we suspect that the implementation may be fundamentally flawed due to the fact the system is likely not totally observable - if the observation matrix of the system at each time step is not full rank, the EKF is not well suited to predicting the state given new measurements. Because of the size of the state (N=15), the observability matrix is quite complex and difficult to analyze, we have not been able to verify whether or not that is the case. A further question is whether the linearization of the measurement function lost some cruicial component of the sensor model logic (such as angle wrapping from 0 to 2π). We will continue to work to debug this system, in case the error is in our implementation, but for the moment we move on to an implementation without sensor bias estimation.

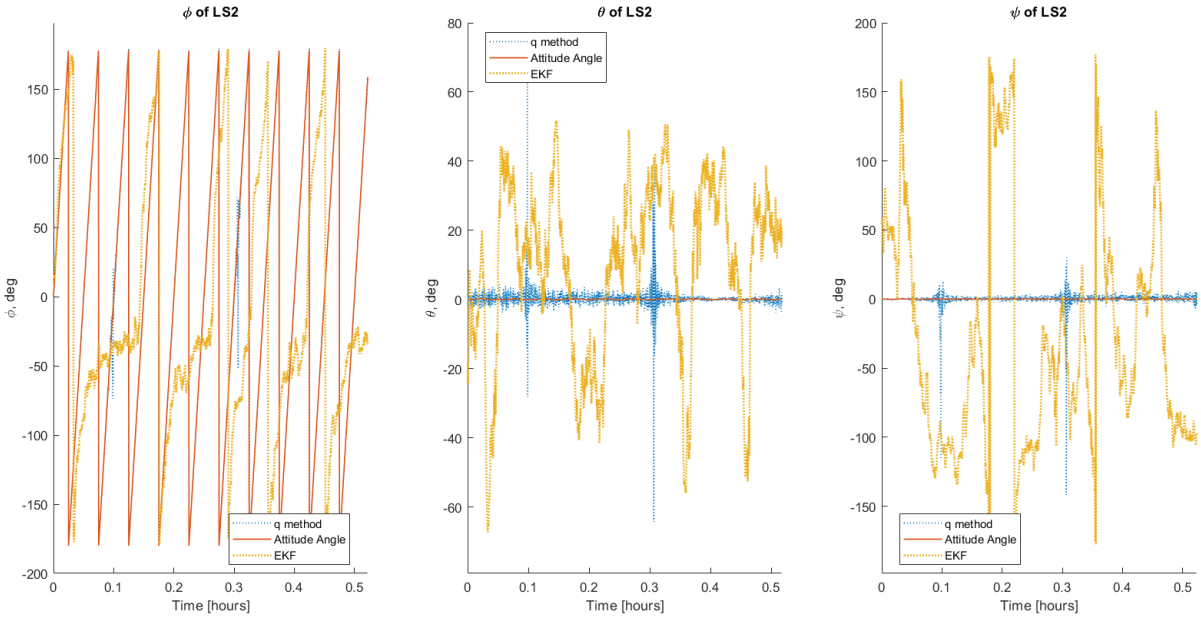

Figure 36: Attitude estimate from EKF with sensor bias estimation

7.4 EKF WITHOUT SENSOR BIAS

The implementation of the EKF without sensor bias included in the estimation was far more fruitful. The resulting estimates are provided below in Figures 41 and 42. A discussion of the error, residual, and covariance results is provided in Appendix K. In general, note that the performance of the EKF is noticeably better than the q-method after a short initial period of attitude uncertainty, in addition to providing an estimate of error at each time step.

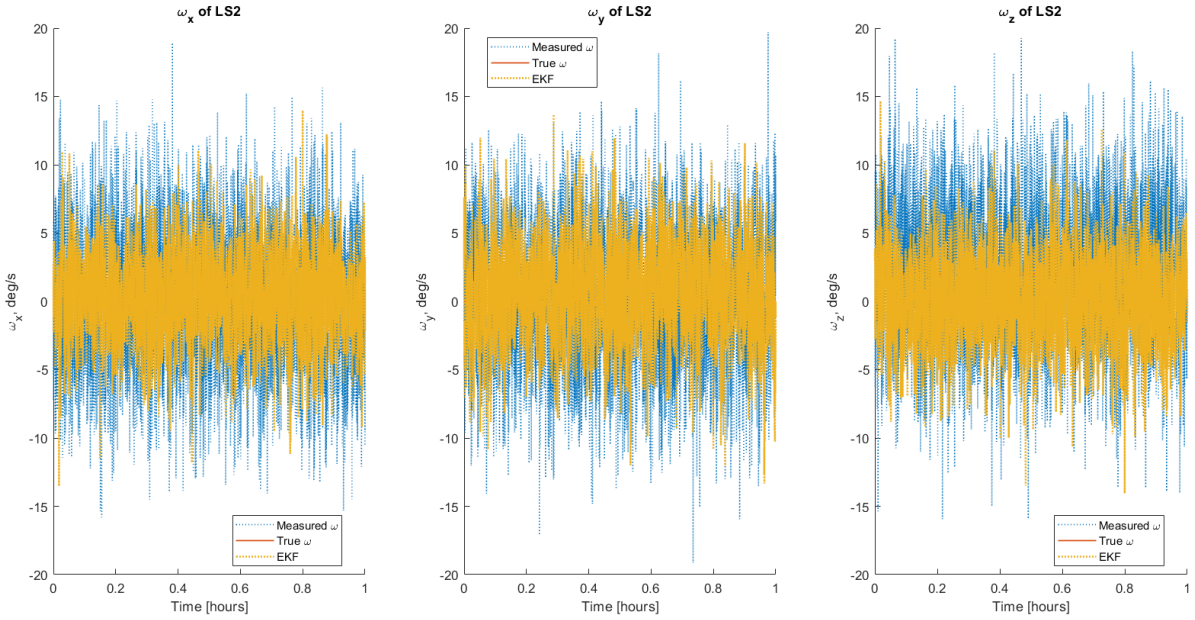

Figure 37: Angular velocity estimate from EKF with sensor bias estimation

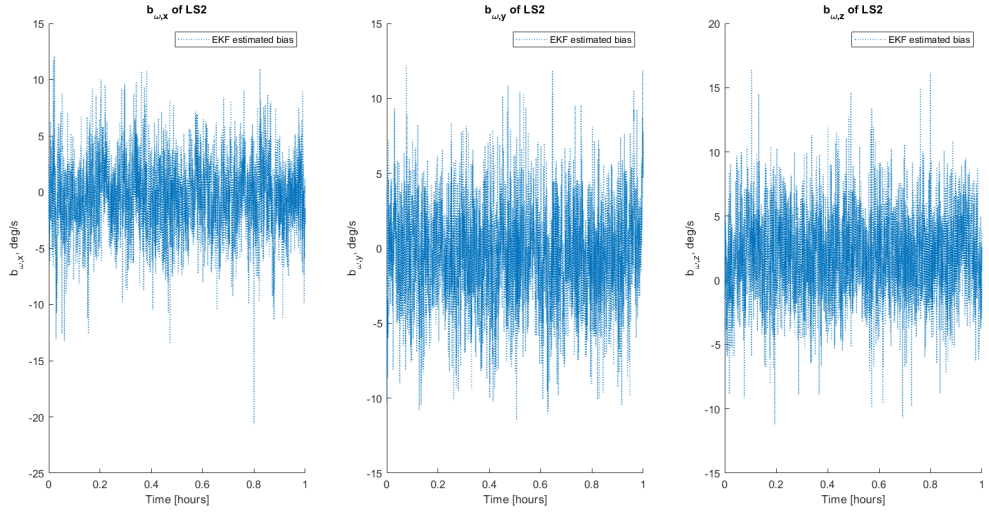

Figure 38: Angular velocity bias estimate from EKF

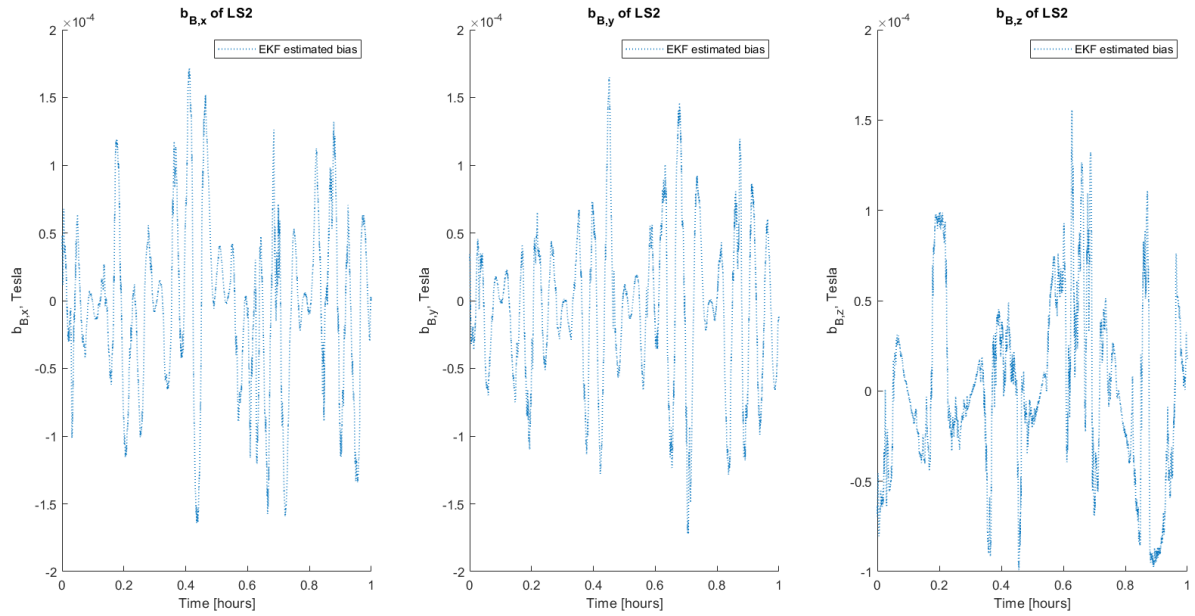

Figure 39: Magnetic sensor bias estimate from EKF

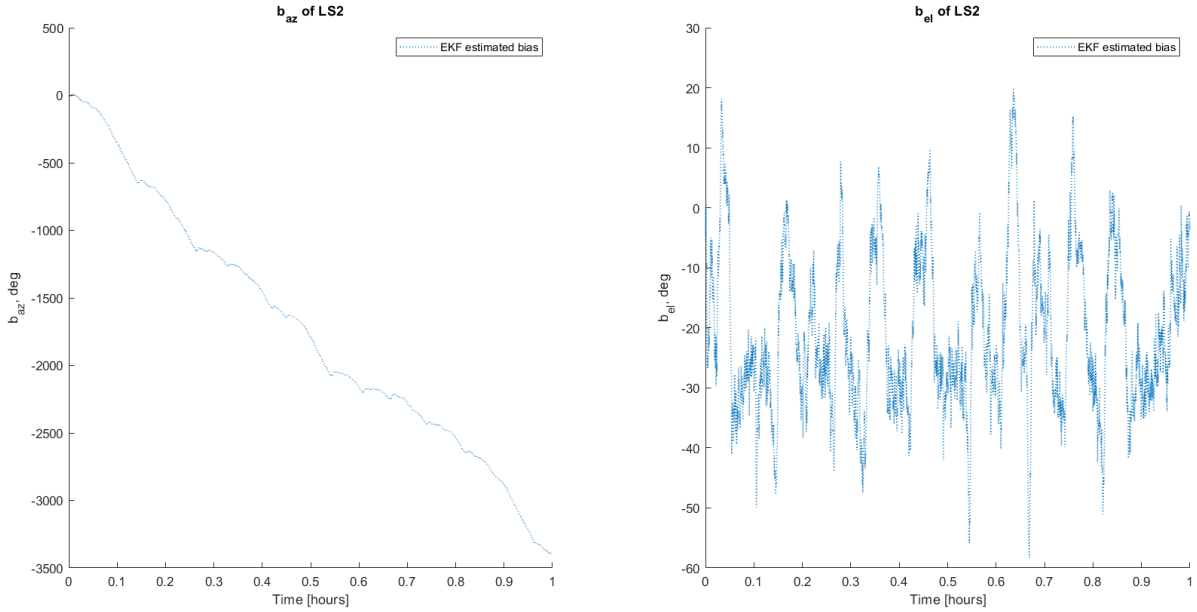

Figure 40: Sun Sensor azimuth and elevation bias estimate from EKF with major issues

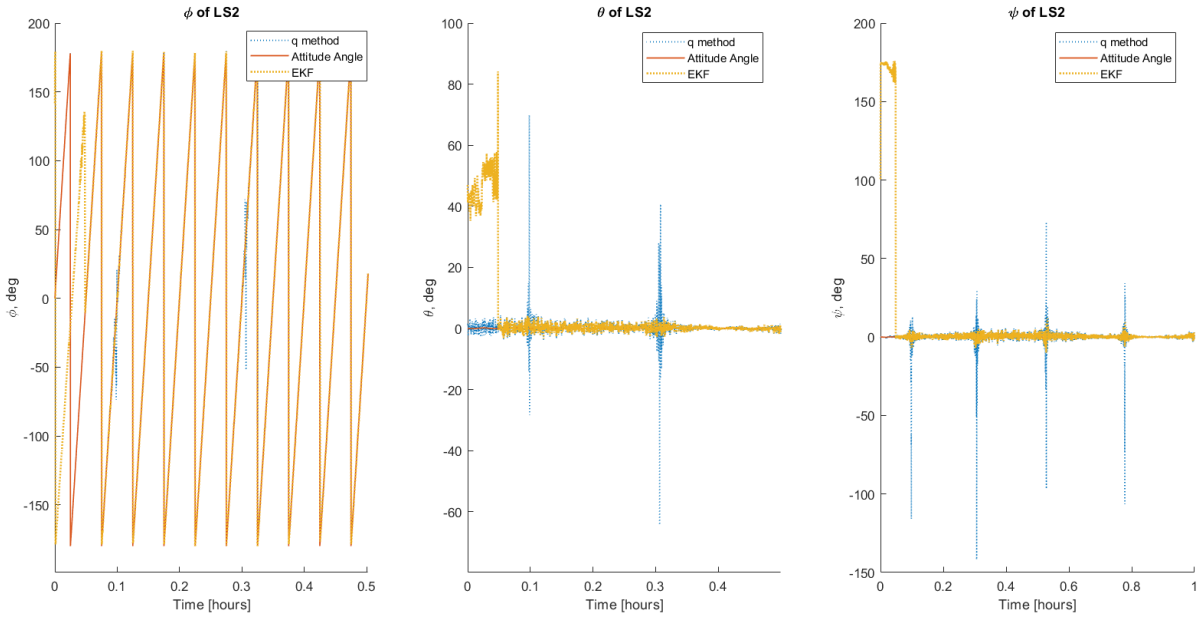

Figure 41: Attitude estimate from EKF without sensor bias estimation

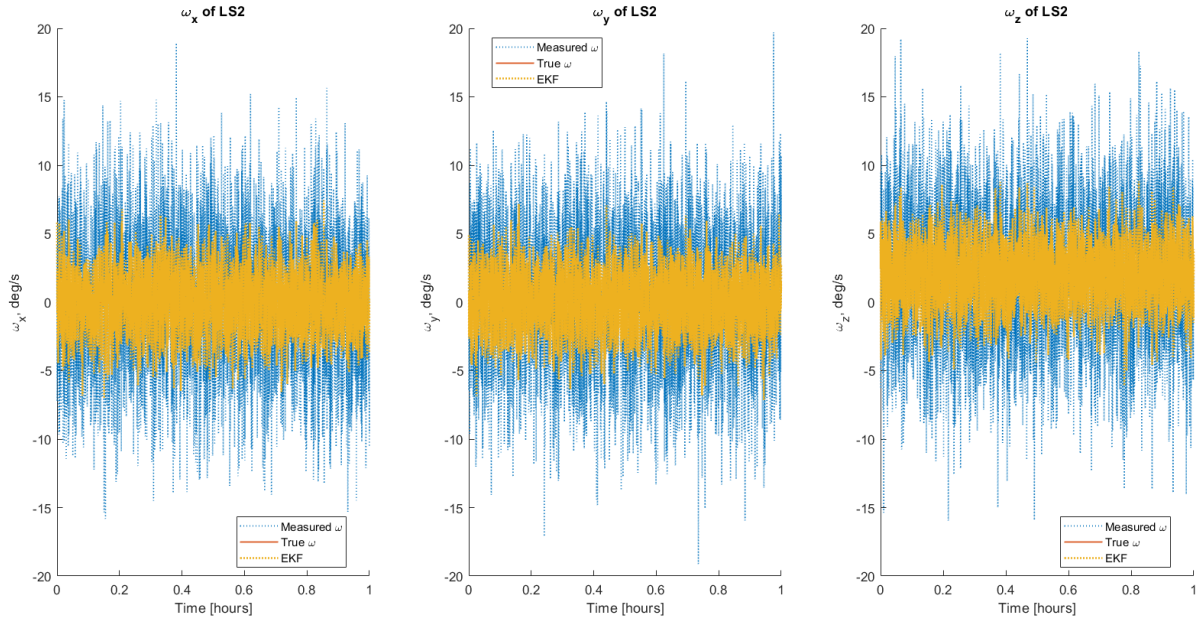

Figure 42: Angular velocity estimate from EKF without sensor bias estimation

8 REFERENCES

[1] Craig J. Van Beusekom and Ron Lisowski. "THREE-AXES ATTITUDE DETERMINATION FOR FALCONSAT-3". In: *AIAA* (2003).

[2] Chris Biddy and Tomas Svitek. "LightSail-1 Solar Sail Design and Qualification". In: 2012.

[3] George C. Marshall Space Flight Center. *NASA Facts: NanoSail-D*. https://www.nasa.gov/centers/marshall/pdf/484314main_NASAfactsNanoSail-D.pdf. Accessed: 4-6-2021.

[4] Jason Davis. *What's the Difference between LightSail 1 and LightSail 2?* https://www.planetary.org/articles/difference-between-lightsails. Accessed: 4-6-2021. June 2019.

[5] *Endurosat 3U Solar Panel*. https://www.endurosat.com/cubesat-store/cubesat-solar-panels/3u-solar-panel-xy/. Accessed: 4-3-2021.

[6] Wiley J. Larson and James R. Wertz. *Space Mission Analysis and Design*. Space Technology Series. Microcosm Press, 1999. ISBN: 1-881883-10-8.

[7] *Lightsail 2: Parts List*. Accessed: 4-3-2021. 2017.

[8] Barbara Plante et al. "LightSail 2 ADCS : From Simulation to Mission Readiness". In: 2016.

[9] Rex W. Ridenoure et al. "Testing The LightSail Program: Advancing Solar Sailing Technology Using a CubeSat Platform". In: 2016.

[10] John B. Schleppe. "Development of a Real-Time Attitude System Using a Quaternion Parameterization and Non-Dedicated GPS Receivers". In: *UCGE Reports* (1996).

[11] The Planetary Society. *LIGHTSAIL 2 MISSION CONTROL*. https://secure.planetary.org/site/SPageNavigator/mission_control.html. Accessed: 4-6-2021.

[12] Yuichi Tsuda et al. "Achievement of IKAROS – Japanese deep space solar sail demonstration mission". In: *Acta Astronautica* 82.2 (2013), pp. 183–188. ISSN: 0094-5765. DOI: https://doi.org/10.1016/j.actaastro.2012.03.032. URL: https://www.sciencedirect.com/science/article/pii/S0094576512001348.

Appendices

A Mass Distribution Analysis

The total mass of the LS2 system is quoted as 4.93kg [9] - using various published resources from the Planetary Society and the drawings in Appendix B, we are able to make rough estimates for the masses of the five primary components: the solar sail, the sail booms, the forward body, the solar panels, and the rear body.

A.1 Solar Sail

We estimate the full mass of the solar sail system (solar sails, sail booms, boom extension mechanism, and sail housing) to be 2.9kg, based off a note from a deployment package development summary stating that the whole deployment system was contained in a package with mass "<3 kg" [2]. The sail housing, which is located in the rear body of the system, we estimate as ≈500g. The solar sails, made of mylar with density $1.38\ \frac{\mathrm{g}}{\mathrm{cm}^3}$, have a total volume of $5.57\mathrm{m} \times 5.57\mathrm{m} \times 4.5\mu\mathrm{m}$ per the LS2 drawings. The total mass of the solar sails is therefore estimated as $\boxed{0.19872\ \mathrm{kg}}$.

A.2 Sail Booms

The sail booms, made of elgiloy with density $8.3\ \frac{\mathrm{g}}{\mathrm{cm}^3}$ [9], have a volume of $3.5\mathrm{cm} \times 0.02\mathrm{cm} \times 4\mathrm{m}$ per the LS2 drawings. The total mass of each sail boom is therefore estimated as $\boxed{0.2324\ \mathrm{kg}}$.

A.3 Forward Body

The forward body contains the communications avionics (transceiver board and antenna) as well as the boom extension mechanism. We can estimate the mass of the boom extension mechanism by subtracting the assumed 500g mass of the sail housing, the 198.72g of solar sail mass, and the 232.4g mass of the four sail booms from the estimated solar sail system mass of 2.9kg. By adding to that an estimated ≈200g for communications components, we get the estimated mass of the forward body as $\boxed{1.472\ \mathrm{kg}}$.

A.4 Solar Panels

The mass of each 3U-long solar panel was estimated to be $\boxed{0.150\ \mathrm{kg}}$ based off the similar mass and form factor of Endurosat's 3U solar panel system [5].

A.5 Rear Body

The mass of the rear body was calculated implicitly by subtracting the calculated masses of the above systems from the total satellite mass. This gives an estimated rear body mass of $\boxed{1.73\ \mathrm{kg}}$. We give some validity to this estimate by noting that the breakdown in Table 8 provides reasonable estimates for rear body component masses that total to 1.74 kg. Note that the table lists some approximate values (indicated with ≈) and some values taken from the links on the Lightsail 2 parts list [7] where available .

Description	Mass, kg
Momentum Wheel	0.226
Magnetorquers (x3)	0.690
Battery Cells (x8)	0.128
Avionics	≈ 0.1
Structures	≈ 0.1
Sail Housing	≈ 0.5
TOTAL	**1.744**

Table 8: Estimated Mass Breakdown of Rear Body

B LS2 System Drawings

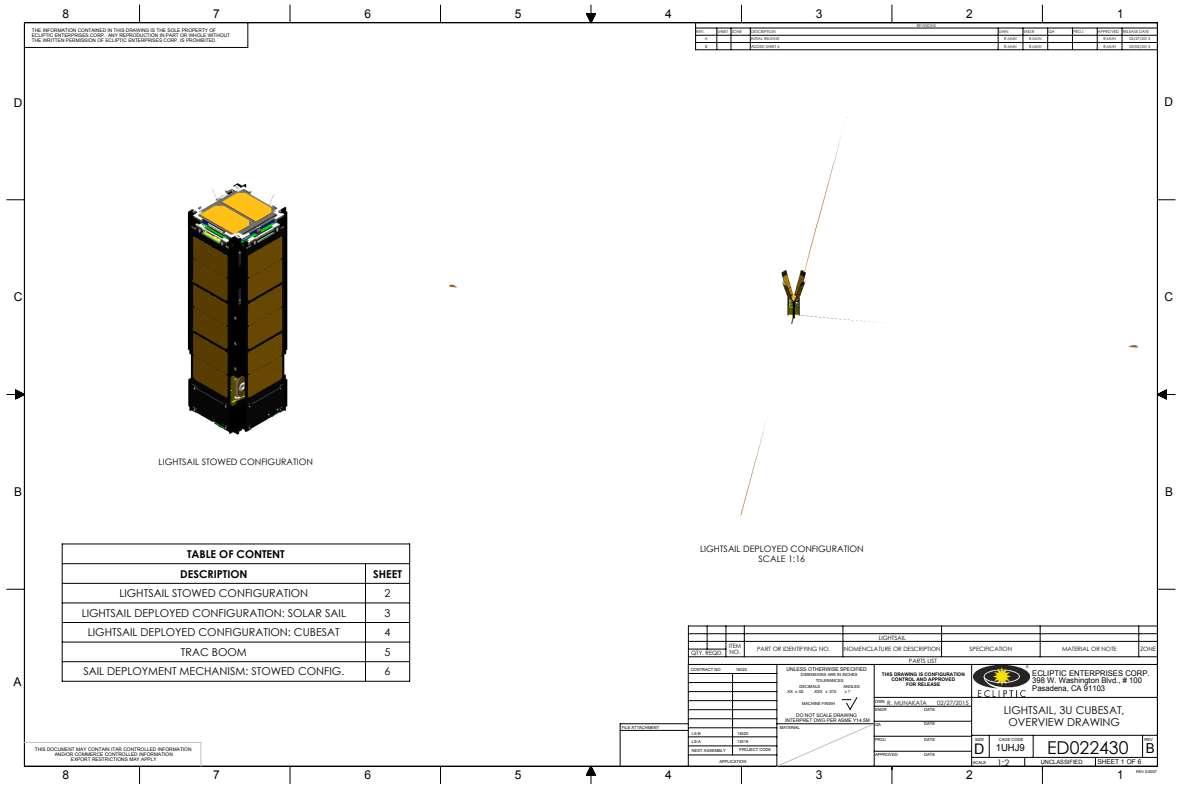

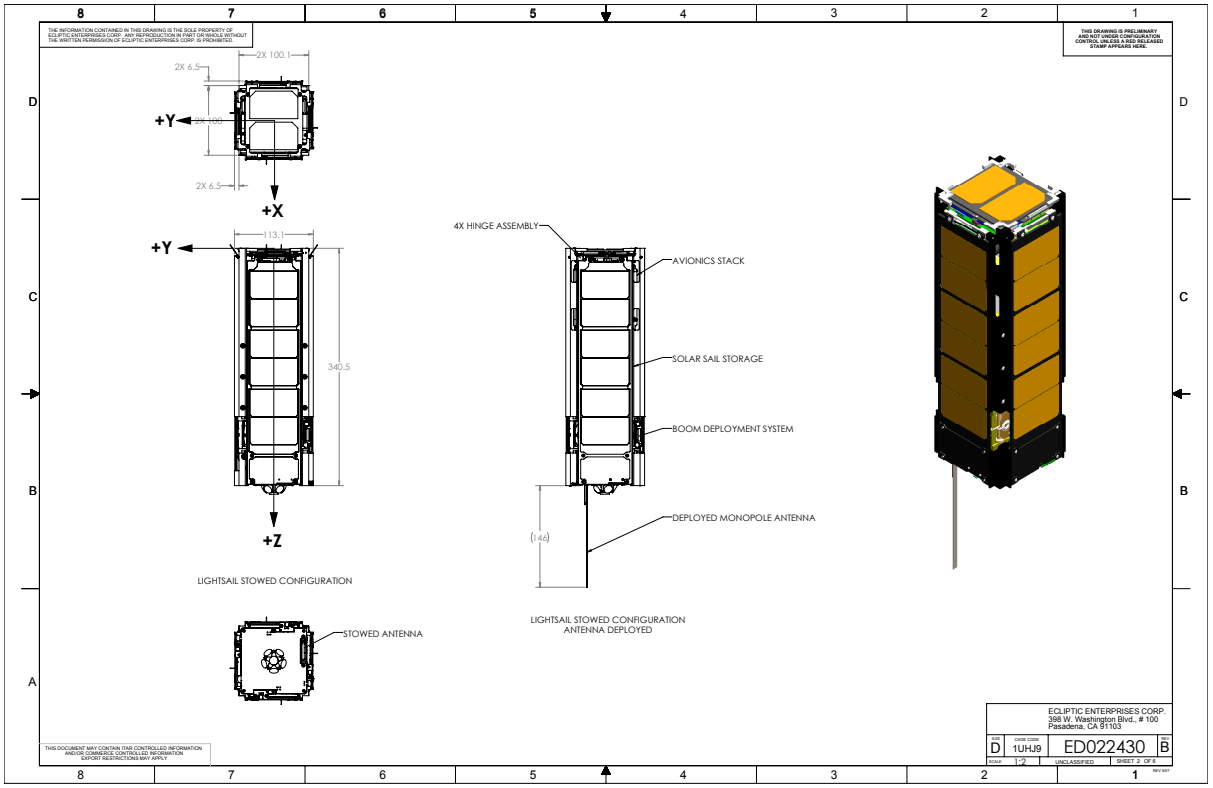
THE INFORMATION CONTAINED IN THIS DRAWING IS THE SOLE PROPERTY OF ECLIPTIC ENTERPRISES CORP. ANY REPRODUCTION IN PART OR WHOLE WITHOUT THE WRITTEN PERMISSION OF ECLIPTIC ENTERPRISES CORP. IS PROHIBITED.
THIS DRAWING IS PRELIMINARY AND NOT UNDER CONFIGURATION CONTROL UNLESS A RED RELEASED STAMP APPEARS HERE.
2X 100.1
2X 6.5
+Y
+X
+Z
113.1
340.5
4X HINGE ASSEMBLY
AVIONICS STACK
SOLAR SAIL STORAGE
BOOM DEPLOYMENT SYSTEM
DEPLOYED MONOPOLE ANTENNA
(146)
LIGHTSAIL STOWED CONFIGURATION
STOWED ANTENNA
LIGHTSAIL STOWED CONFIGURATION
ANTENNA DEPLOYED
THIS DOCUMENT MAY CONTAIN ITAR CONTROLLED INFORMATION AND/OR COMMERCE CONTROLLED INFORMATION EXPORT RESTRICTIONS MAY APPLY
ECLIPTIC ENTERPRISES CORP.
398 W. Washington Blvd., # 100
Pasadena, CA 91103
SIZE D
CAGE CODE 1UHJ9
ED022430
REV B
SCALE 1:2
UNCLASSIFIED
SHEET 2 OF 6

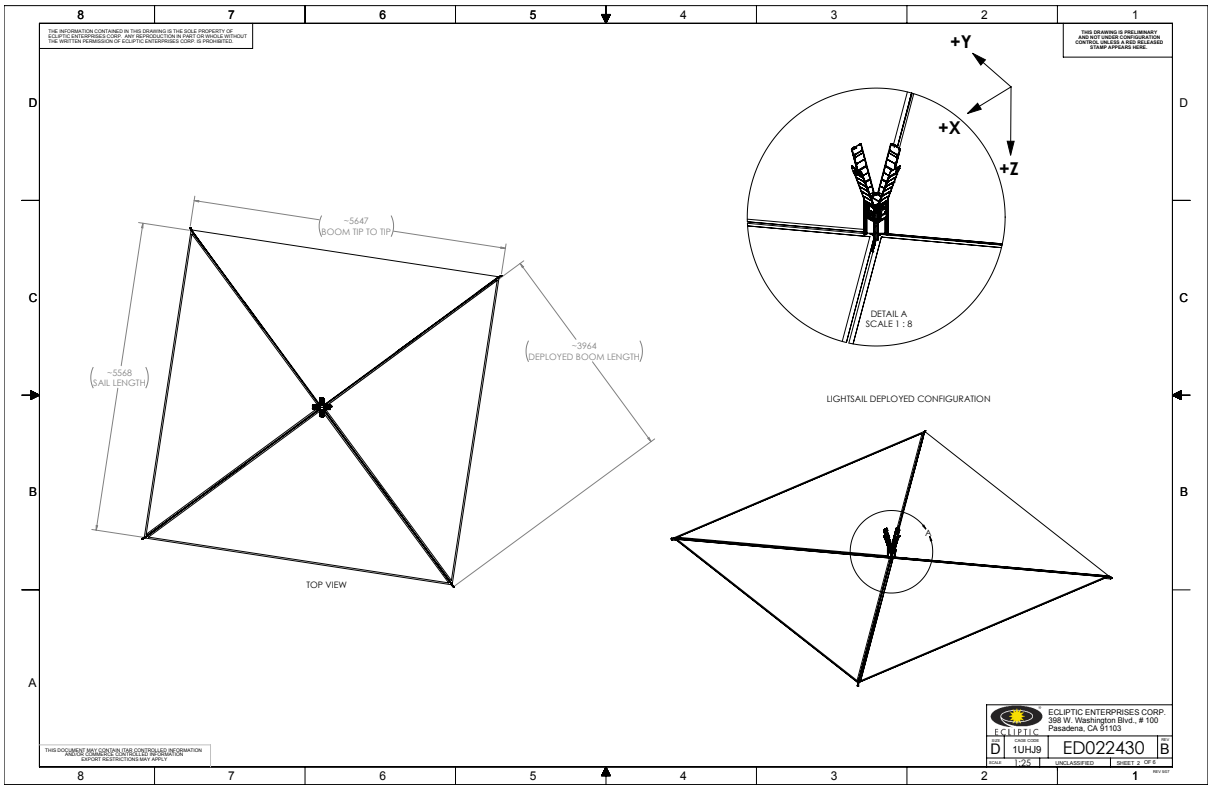
THE INFORMATION CONTAINED IN THIS DRAWING IS THE SOLE PROPERTY OF ECLIPTIC ENTERPRISES CORP. ANY REPRODUCTION IN PART OR WHOLE WITHOUT THE WRITTEN PERMISSION OF ECLIPTIC ENTERPRISES CORP. IS PROHIBITED.
THIS DRAWING IS PRELIMINARY AND NOT UNDER CONFIGURATION CONTROL UNLESS A RED RELEASED STAMP APPEARS HERE.
~5647
(BOOM TIP TO TIP)
~5568
(SAIL LENGTH)
~3964
(DEPLOYED BOOM LENGTH)
TOP VIEW
+Y
+X
+Z
DETAIL A
SCALE 1 : 8
LIGHTSAIL DEPLOYED CONFIGURATION
THIS DOCUMENT MAY CONTAIN ITAR CONTROLLED INFORMATION AND/OR COMMERCE CONTROLLED INFORMATION EXPORT RESTRICTIONS MAY APPLY
ECLIPTIC ENTERPRISES CORP.
398 W. Washington Blvd., # 100
Pasadena, CA 91103
SIZE D
CAGE CODE 1UHJ9
ED022430
REV B
SCALE 1:25
UNCLASSIFIED
SHEET 2 OF 6

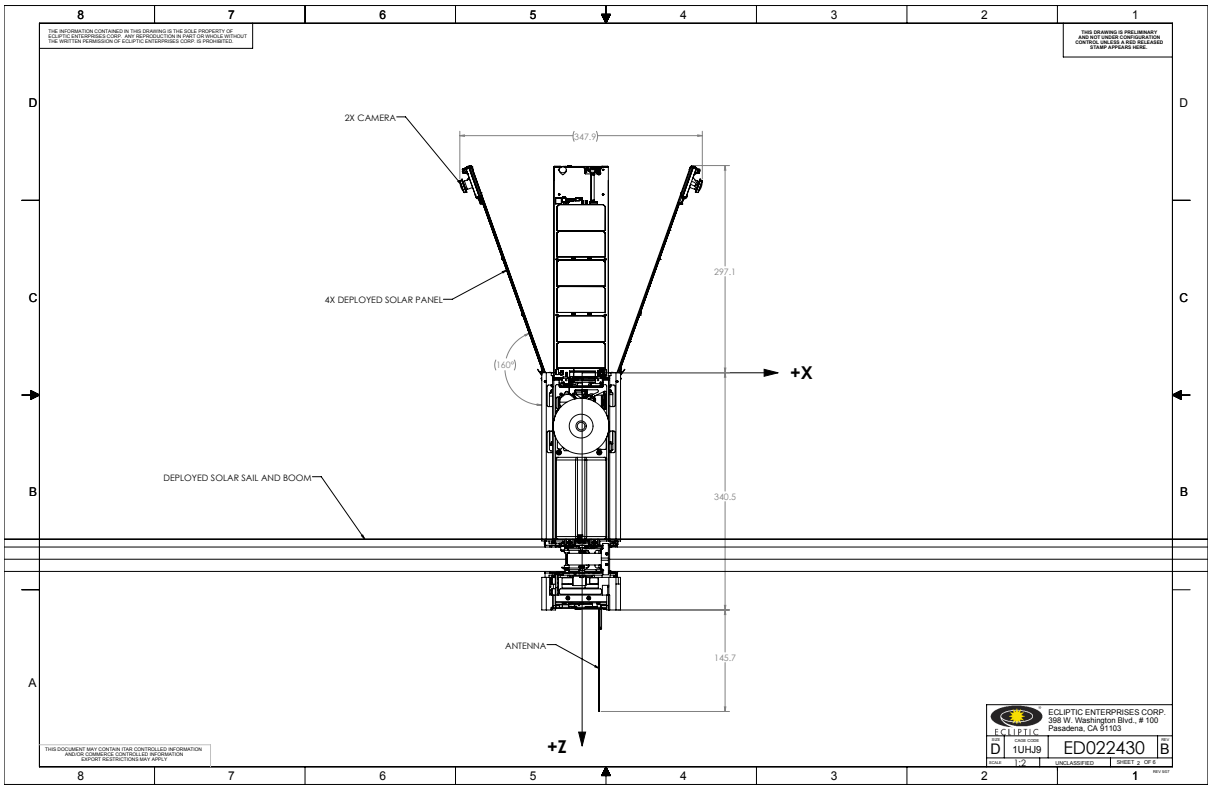
2X CAMERA
(347.9)
297.1
4X DEPLOYED SOLAR PANEL
(160°)
+X
DEPLOYED SOLAR SAIL AND BOOM
340.5
ANTENNA
145.7
+Z
ECLIPTIC ENTERPRISES CORP.
398 W. Washington Blvd., # 100
Pasadena, CA 91103
ED022430
UNCLASSIFIED

C VBA Solidworks Macro for Exporting Surface Normals

The Solidworks VBA macro below uses a sketch to generate information about the outer geometry of a shape - the starting location of a line is taken to be the barycenter of the surface, and the unit direction is taken from the vector from the start point to the end point (normalized by length). The area of the associated surface (in m^2) is encoded in the length of the line (in m) - this is particularly easy to do in Solidworks with parameterized dimensions, and makes updating the centroids and normals an easy process, even for complicated shapes. The MATLAB script following then imports the information to MATLAB.

```
Dim swApp As Object
Sub main()
Dim swApp As SldWorks.SldWorks
Dim doc As SldWorks.ModelDoc2
Dim assembly As SldWorks.AssemblyDoc
Dim sm As SldWorks.SelectionMgr
Dim eq As SldWorks.EquationMgr
Dim feat As SldWorks.Feature
Dim sketch As SldWorks.sketch
Dim v As Variant
Dim i As Long
Dim sseg As SldWorks.SketchSegment
Dim sline As SldWorks.SketchLine
Dim sp As SldWorks.SketchPoint
Dim ep As SldWorks.SketchPoint
Dim s As String
Dim CMx, CMy, CMz As Double



Set exApp = CreateObject("Excel.Application")
 If Not exApp Is Nothing Then
  exApp.Visible = True
  If Not exApp Is Nothing Then
   exApp.Workbooks.Add
   Set sheet = exApp.ActiveSheet
   If Not sheet Is Nothing Then
    sheet.Cells(1, 1).Value = "X (m)"
    sheet.Cells(1, 2).Value = "Y (m)"
    sheet.Cells(1, 3).Value = "Z (m)"
    sheet.Cells(1, 4).Value = "Normal X"
    sheet.Cells(1, 5).Value = "Normal Y"
    sheet.Cells(1, 6).Value = "Normal Z"
    sheet.Cells(1, 7).Value = "Area (m*m)"
   End If
  End If
 End If


Set swApp = GetObject(, "sldworks.application")
 If Not swApp Is Nothing Then
  Set doc = swApp.ActiveDoc
  If Not doc Is Nothing Then
   If doc.GetType = swDocASSEMBLY Then
    Set assembly = doc
    Set sm = doc.SelectionManager
```

```
47      Set eq = doc.GetEquationMgr
48      If Not assembly Is Nothing And Not sm Is Nothing Then
49          Dim j, m As Long
50          m = eq.GetCount
51          For j = 0 To m - 1
52              If InStr(1, eq.Equation(j), "SW-CenterofMassX") Then
53                  CMx = eq.Value(j)
54              ElseIf InStr(1, eq.Equation(j), "SW-CenterofMassY") Then
55                  CMy = eq.Value(j)
56              ElseIf InStr(1, eq.Equation(j), "SW-CenterofMassZ") Then
57                  CMz = eq.Value(j)
58              End If
59          Next j
60
61       If sm.GetSelectedObjectType2(1) = swSelSKETCHES Then
62        Set feat = sm.GetSelectedObject6(1, -1)
63        Set sketch = feat.GetSpecificFeature2
64        If Not sketch Is Nothing Then
65         v = sketch.GetLines2(1)
66         numlines = sketch.GetLineCount2(1)
67         Dim c As Long
68         c = 0
69         For i = 0 To numlines - 1
70          If Not sheet Is Nothing And Not exApp Is Nothing Then
71
72              Dim myType As Double
73              myType = (v(12 * i + 2))
74
75              If myType < 1 Then
76
77              Dim startX, startY, startZ, endX, endY, endZ, myL As Double
78              startX = (v(12 * i + 6))
79              startY = (v(12 * i + 7))
80              startZ = (v(12 * i + 8))
81              endX = (v(12 * i + 9))
82              endY = (v(12 * i + 10))
83              endZ = (v(12 * i + 11))
84              myL = Sqr(((startX - endX) ^ 2) + ((startY - endY) ^ 2) ...
                    + ((startZ - endZ) ^ 2))
85              sheet.Cells(2 + c, 1).Value = startX - CMx
86              sheet.Cells(2 + c, 2).Value = startY - CMy
87              sheet.Cells(2 + c, 3).Value = startZ - CMz
88              sheet.Cells(2 + c, 4).Value = (endX - startX) / myL
89              sheet.Cells(2 + c, 5).Value = (endY - startY) / myL
90              sheet.Cells(2 + c, 6).Value = (endZ - startZ) / myL
91              sheet.Cells(2 + c, 7).Value = myL
92              exApp.Columns.AutoFit
93              c = c + 1
94              End If
95          End If
96         Next i
97        End If
98       End If
99      End If
100    End If
101   End If
102  End If
103 End Sub
```

```
%% get_surfacedata()
% Reads surface data from CSV file.
% No input.
% Output:
%   - C : an (n x 3) matrix, where n is the number of surfaces, denoting
%         the location in body coordinates of each surface's ...
    centroid in m.
%   - N : an (n x 3) matrix denoting the unit outward-facing normal for
%         each surface.
%   - A : an (n x 1) matrix denoting the area for each surface, in m^2.

function [C, N, A] = get_surfacedata()
    centroid_file = 'CentroidData.csv';
    data = readtable(centroid_file, 'ReadVariableNames', false);
    C = [data.Var1 , data.Var2 , data.Var3];
    N = [data.Var4 , data.Var5 , data.Var6];
    A = data.Var7;
end
```

D Verification of Inertia Computations

For our analytical calculations, we will ignore asymmetric components, and place the associated mass of each primary component at its geometric centroid (this is a fairly safe assumption, given the layout of our satellite). This will greatly simplify our calculations.

We begin with two basic equations; first, the moments of inertia of a rectangular prism with length a along its principal x axis, length b along its principal y axis, length c along its principal z axis, and mass m:

$$I_{xx} = \frac{1}{12}m(b^2 + c^2)$$
$$I_{yy} = \frac{1}{12}m(a^2 + c^2)$$
$$I_{zz} = \frac{1}{12}m(a^2 + b^2)$$

We will also need the formula for a rectangular prism tilted about an axis, as the sail booms are at a 45° angle w.r.t the z axis and the solar panels are tilted at 20° w.r.t to the x/y axes. For the sail booms, I_{zz} is the same as above, but our formula for I_{yy} will need to be modified to account for this rotation. I_{yy} for this rectangular prism (assuming the tilt angle is $\beta = 45°$) is

$$I_{yy} = \frac{1}{12}m(acos\beta + bsin\beta + c)$$

For the solar panels, we will also need to use (depending on the orientation of the panel)

$$I_{zz} = \frac{1}{12}m(acos\beta + b + csin\beta)$$
$$\text{if tilted w.r.t to } x \text{ or}$$
$$I_{zz} = \frac{1}{12}m(a + bcos\beta + csin\beta)$$
$$\text{if tilted w.r.t to } y.$$

We also will make use of the parallel axis theorem, which states that the moment of inertia of a body about an axis B parallel to an axis, A, can be written as

$$I_B = I_A + mr^2$$

where m is the mass of the body and r is the distance between the parallel axes.

We also recognize that due to our simplified x-y symmetry, $I_{xx} = I_{yy}$ for our purposes, and by definition, our x and y axes are aligned with the principal axes. Furthermore, due to the alignment of our body axes along the line of symmetry, we know that our full inertia matrix w.r.t the body axes is roughly

$$L = \begin{bmatrix} I_{xx} & 0 & 0 \\ 0 & I_{yy} & 0 \\ 0 & 0 & I_{zz} \end{bmatrix} = \begin{bmatrix} I_{xx} & 0 & 0 \\ 0 & I_{xx} & 0 \\ 0 & 0 & I_{zz} \end{bmatrix}$$

In Table 9, we tabulate the mass, a, b, c, and the distance between the principal axis and y/z body axes for each component (measured using the CAD model). Applying our equation for moment

Component	Mass, kg	Width a, m	Length b, m	Height c, m	// to Y-Axis, m	// to Z-Axis, m	Quantity	Iyy, kg m^2	Izz, kg m^2
Forward Body	1.47168	0.1	0.1	0.11	0.12055	0	1	0.0241	0.0024528
Sail Booms	0.2324	2.00E-04	4	0.035	1.3249	1.9957	4	6.27E-01	1.24E+00
Sail	0.19872	5.57	5.57	4.50E-06	0.06555	0	1	5.15E-01	1.0275
Rear Body	1.73	0.1	0.1	0.23	0.04945	0	1	0.01330	0.002883
Solar Panel X-Tilt	0.15	6.50E-03	0.1	0.316	0.31294	0.1040	2	1.52E-02	2.18E-03
Solar Panel Y-Tilt	0.15	0.1	6.50E-03	0.316	0.3298	0.1040	2	1.76E-02	2.18E-03
TOTAL	**4.93**	-	-	-	-	-	-	**3.125909335**	**5.983479674**

Table 9: Tabulated Inertia Calculation Data.

of inertia and parallel axis theorem, we are able to calculate the contribution of each item to I_{xx} and I_{zz}. Our final results are $I_{xx} = I_{yy} = 3.125\ \mathrm{kg} \cdot \mathrm{m}^2$ and $I_{zz} = 5.983\ \mathrm{kg} \cdot \mathrm{m}^2$, which have relative errors compared to the CAD-computed values of 0.7% and 0.02%, respectively.

Given these negligibly small errors (likely caused due to the fact that the distances between the parallel axes were measured assuming that the solar panels and booms were planes, rather than prisms with finite thickness, in addition to our simplifying assumptions about mass distribution), it is clear that the CAD-computed values for the inertia characteristics of our system are trustworthy. The off-diagonal components calculate by the 3D model are trusted, as they are very close to zero.

E Additional Orbital Propagator Notes

Plots of evolution of the orbital elements used to generate Figure 4. Atmospheric drag contributes to the decrease in semimajor axis, while J2 contributes to the change in RAAN and argument of periapsis. The perturbation calculations make use of the $e \approx 0$ approximation, which is fine given the initial $e \approx 0.001$, but will need to be modified to increase fidelity as the spacecraft orbit elongates due to SRP.

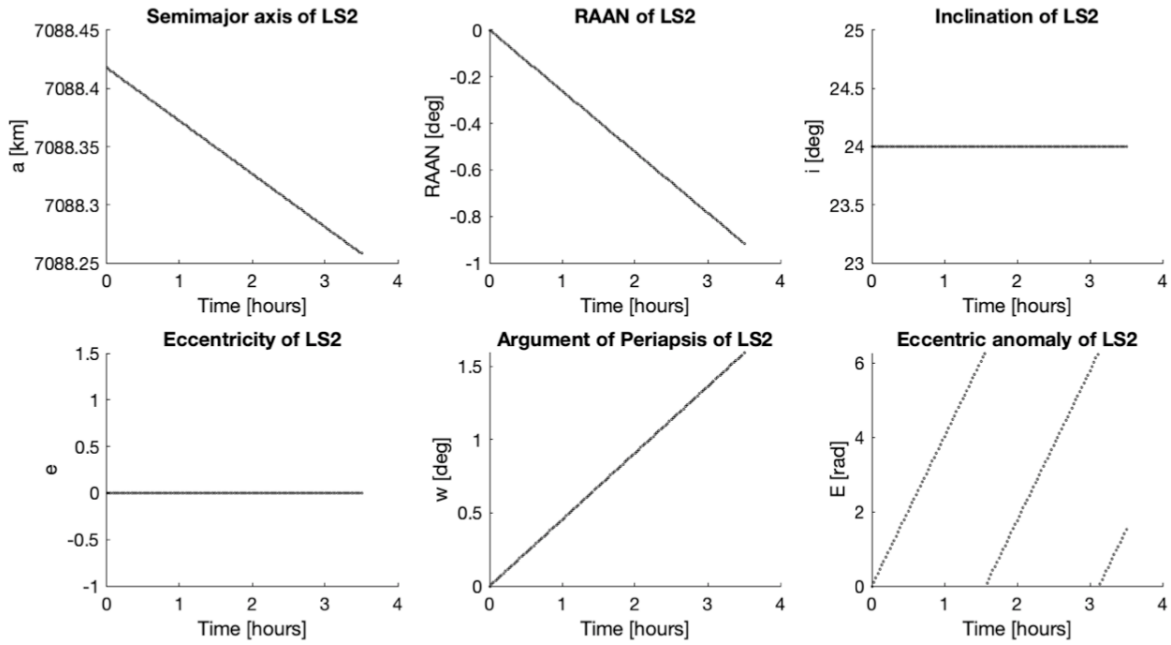

Figure 43: Keplerian orbital elements

F Quaternion and 312 Euler Kinematic Comparison

To validate our attitude propagation system, we compare the propagation of identical initial configurations for both quaternion kinematics and 312 Euler angle kinematics. In the series of figures below, we see the attitude propagation for both kinematics based on spin initially about the principal Y-axis (a principal axis was chosen to avoid the singularity of the 312 Euler sequence at $\Theta = \frac{\pi}{2}$). Note that all plots appear nearly exactly identical, validating the quaternion propagation method.

Furthermore, Fig 47 and 48 show the direct comparisons of the quaternion and 312 Euler output (each being converted to the other attitude for comparison, along with the raw difference error for comparison). Note that the 312 Euler strays from expected behavior the most, but error stay reasonable between the two parameterizations (note that a difference of 360 degrees is equivalent to a difference of zero).

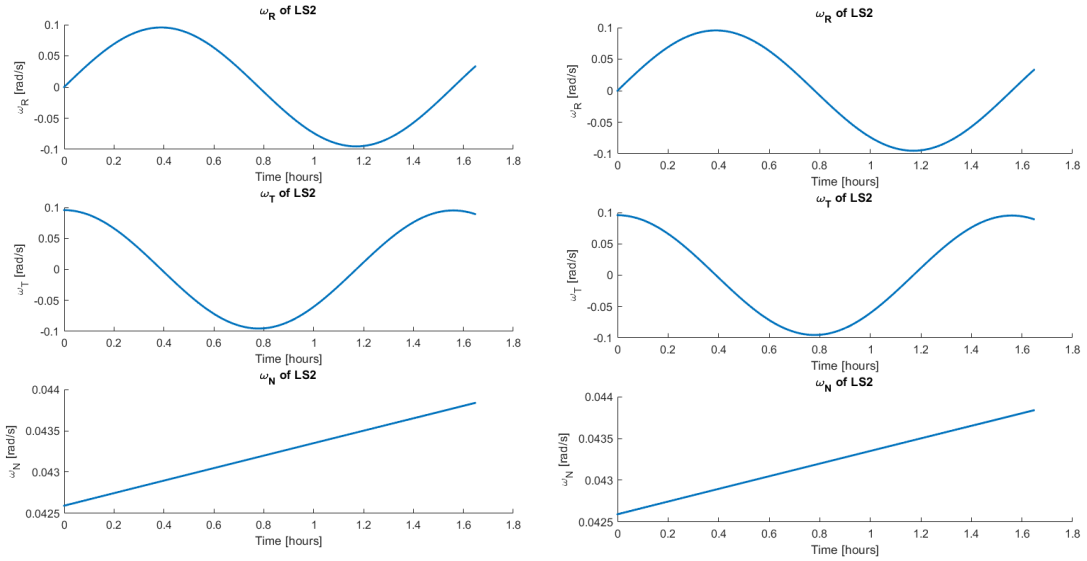

Figure 44: Angular vel. in RTN frame for Quaternion (left) and Euler 312 (right) propagation.

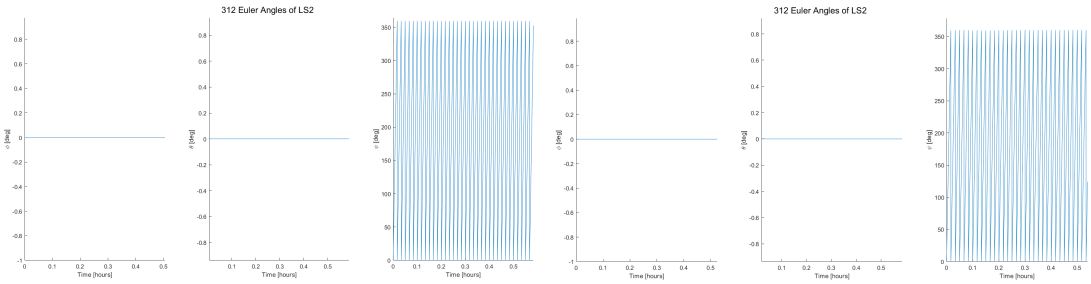

Figure 45: 312 Euler Angles for Quaternion (left) and Euler 312 (right) propagation.

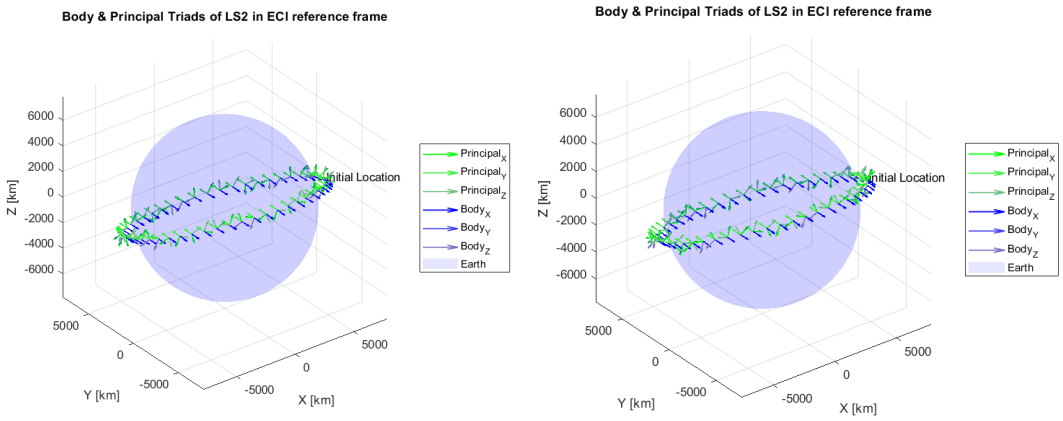

Figure 46: Coordinate triads in ECI frame for Quaternion (left) and Euler 312 (right) propagation.

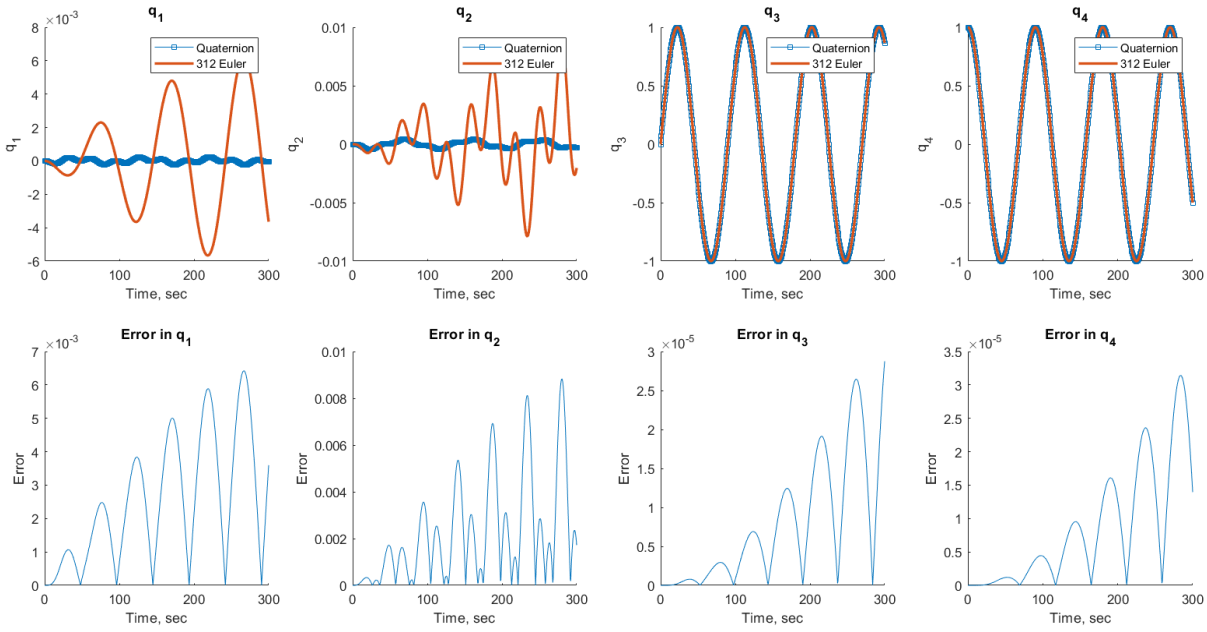

Figure 47: Comparison of quaternions from both attitude parameterizations.

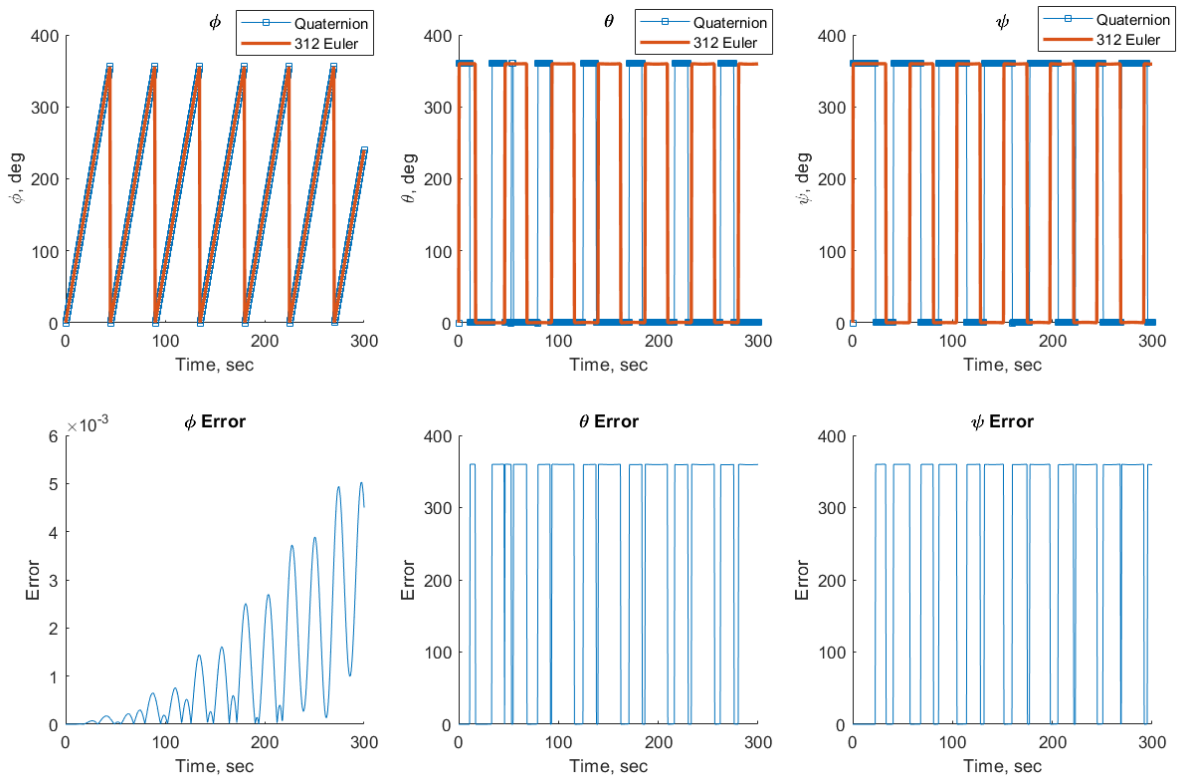

Figure 48: Comparison of Euler angles from both attitude parameterizations.

G Dual Spin Equilibrium & Stability Analysis

To ensure that our addition of a momentum wheel has not modified our simulation dynamics, we repeat the stability and equilibrium analyses required for Problem Set 3, but now with a spinning momentum wheel.

We test equilibrium in 4 cases - setting the momentum wheel's axis to be along a principal axis, we spin the system about the same principal axis and turn the momentum wheel on at 1 rad/s. Fig 49-50 show the resulting inertial-axes angular velocity and the associated 312 Euler angles. In the fourth case, we set the principal axes to be initially aligned with the RTN frame, then spin initially about the N axis. The resulting RTN frame angular velocity and 312 Euler angles are showin in 52. Note that as expected, our angular velocities remain constant and one Euler angle increases linearly.

We test stability in 3 cases - setting the momentum wheel's axis to be along a principal axis, we spin the system primarily about the same axis at 7 deg/s with the momentum wheel spinning at 1 rad/s, and give minor 0.01 deg/s perturbative spins about the other two principal axes. Fig 53-54 show the resulting inertial-axes angular velocity and the associated 312 Euler angles. Note that as expected, spinning about X and Z result in periodically stable spin, while initially spinning about Y with perturbation resulting in instability.

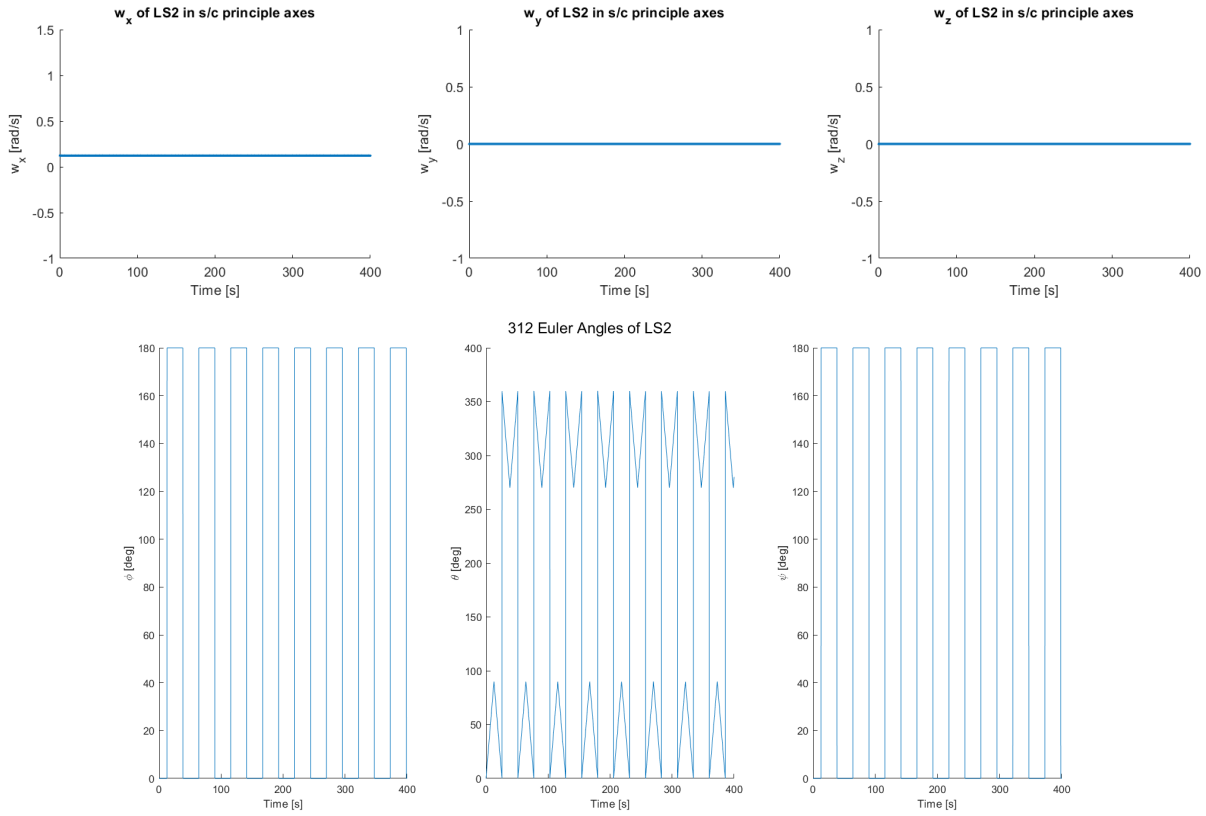

Figure 49: Dual spin equilibrium test with initial spin around X axis.

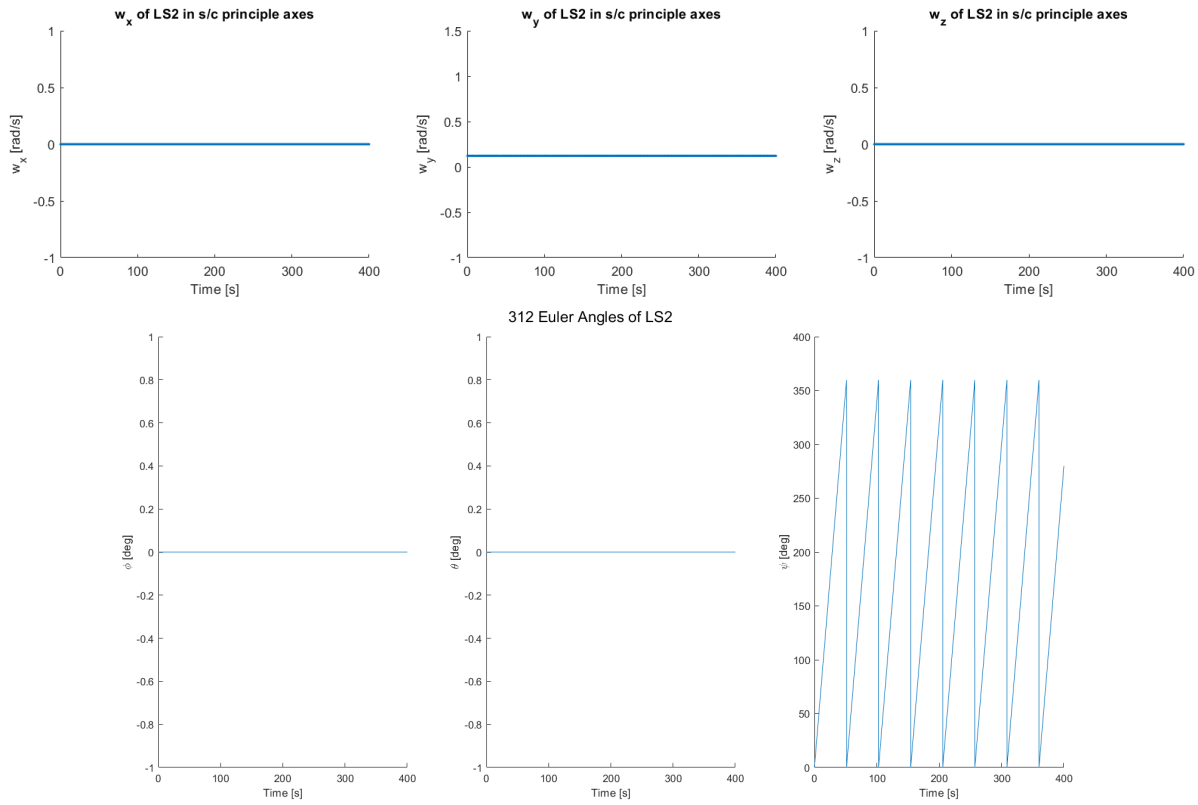

Figure 50: Dual spin equilibrium test with initial spin around Y axis.

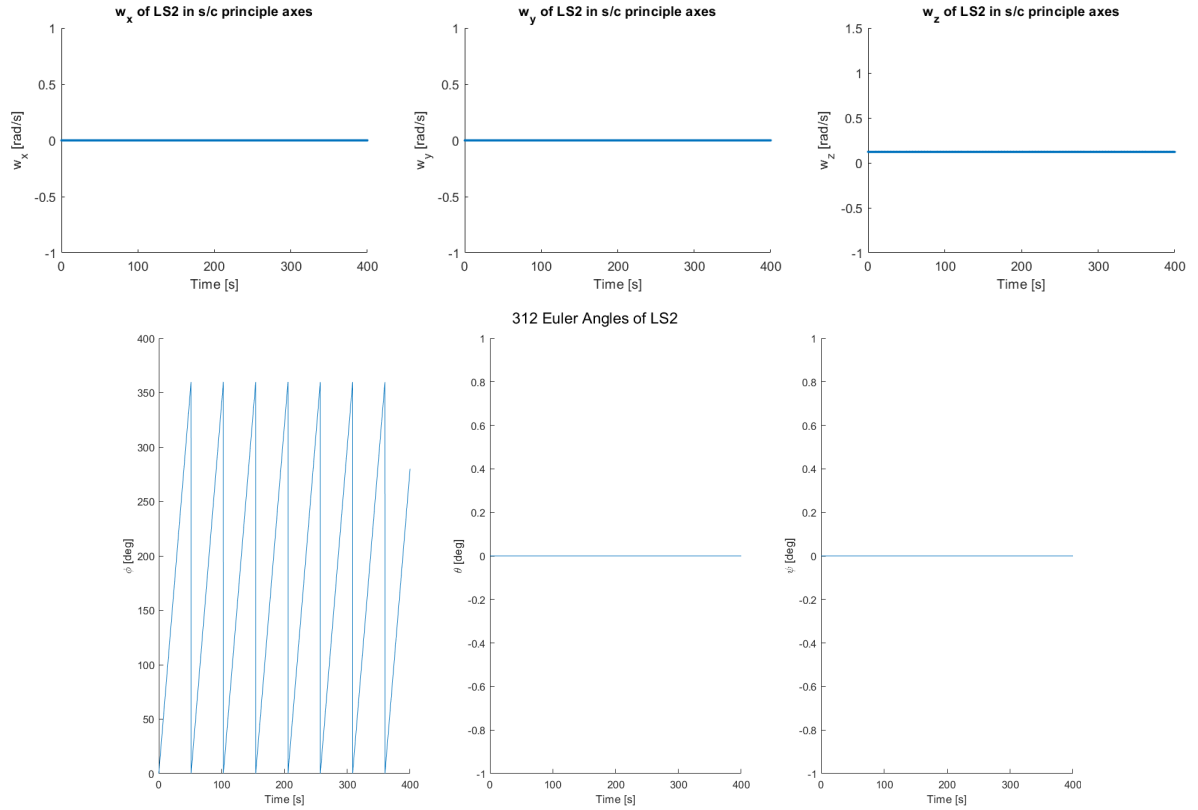

Figure 51: Dual spin equilibrium test with initial spin around Z axis.

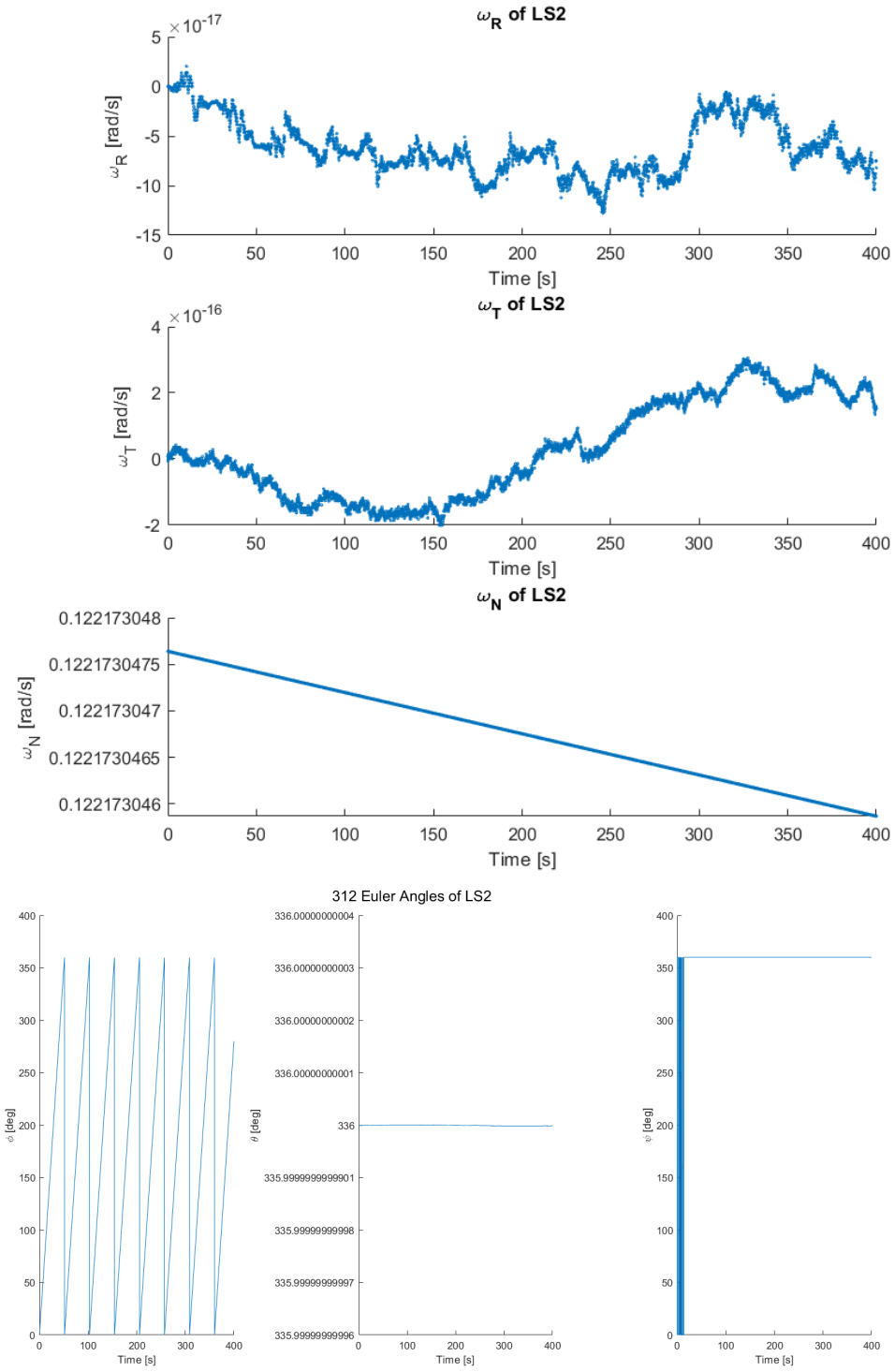

Figure 52: Dual spin equilibrium test with principal axes aligned with RTN, initial spin around N axis.

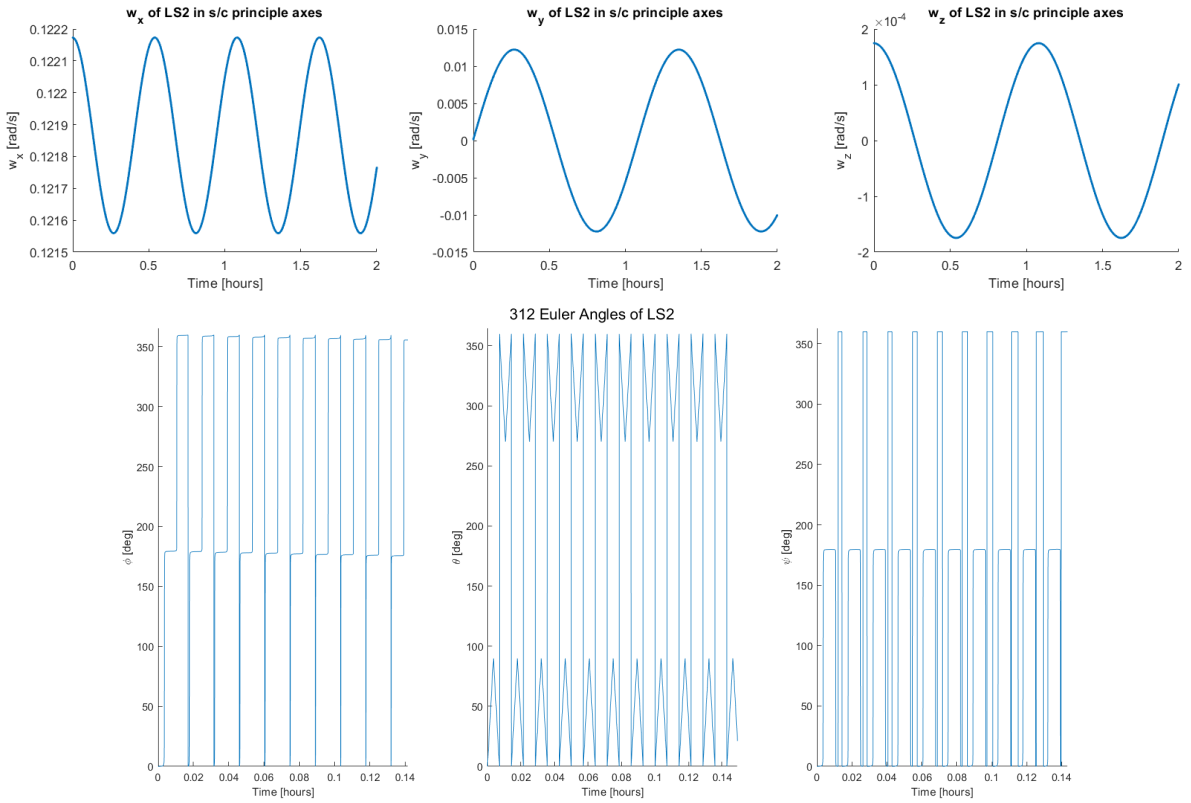

Figure 53: Dual spin stability test with initial spin mostly around X axis.

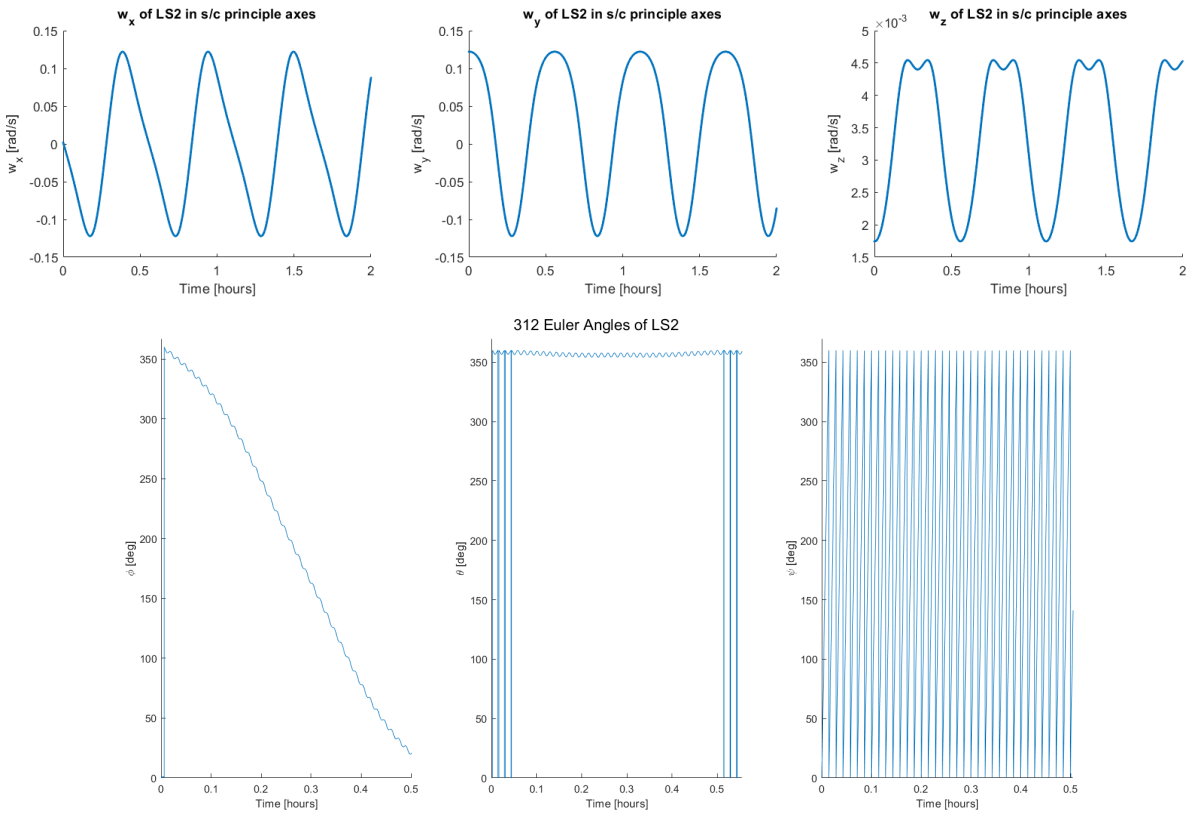

Figure 54: Dual spin stability test with initial spin mostly around Y axis.

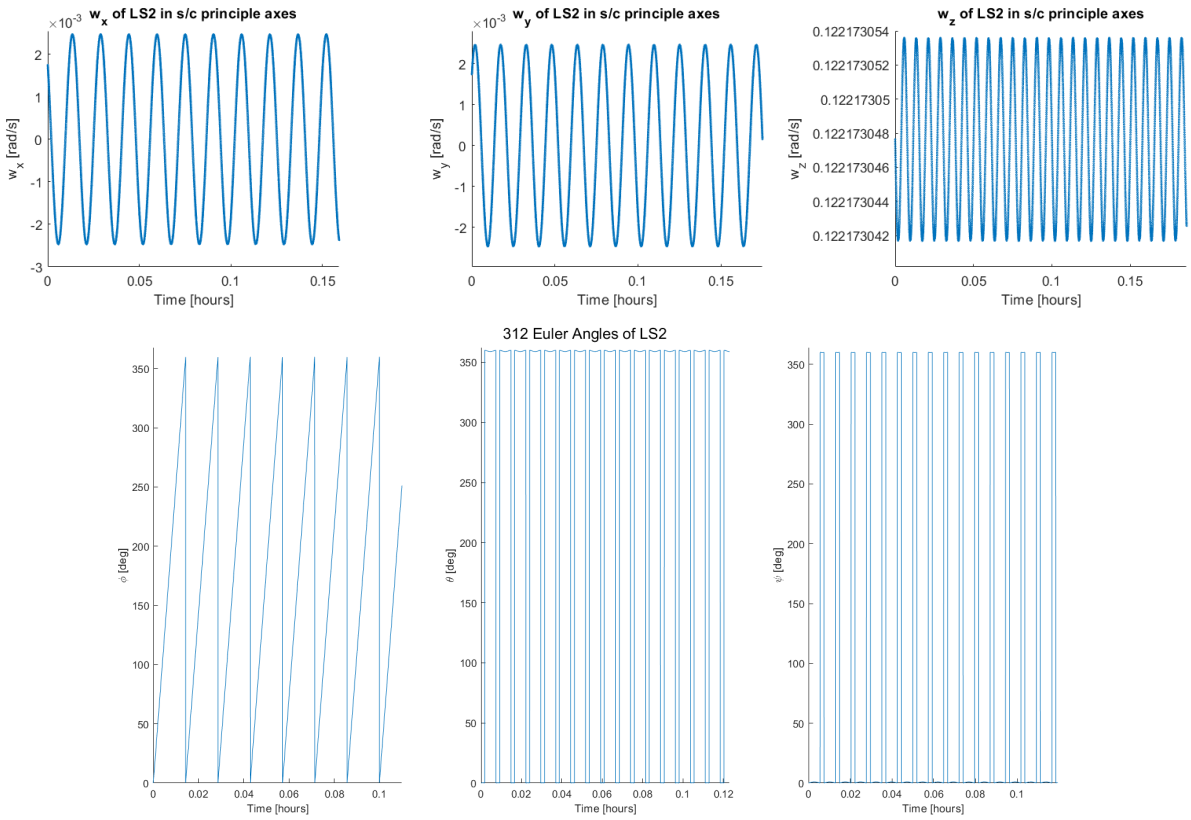

Figure 55: Dual spin stability test with initial spin mostly around Z axis.

H Gravity Gradient Stability

The gravity gradient stability is assessed in 3 cases in 2 configurations: stable (unperturbed and perturbed) and unstable. On Figure 25, these correspond to the LS2 stable config and LS2 unstable config 2, respectively.

Figure 56 shows that the spacecraft indeed remains at equilibrium if it begins in a stable orbit, with the principal axes aligned with the orbit RTN frame. The spacecraft performs small oscillations about the equilibrium position, but they remain bounded. However, as we can see in figure 57, even a small perturbation (of 10^{-4} rad/s) pushes the spacecraft into an unstable configuration, introducing a small oscillation that grows slowly with time. Lastly, Figure 58 shows the motion created by the gravity gradient in an unstable configuration, which behaves unpredictably.

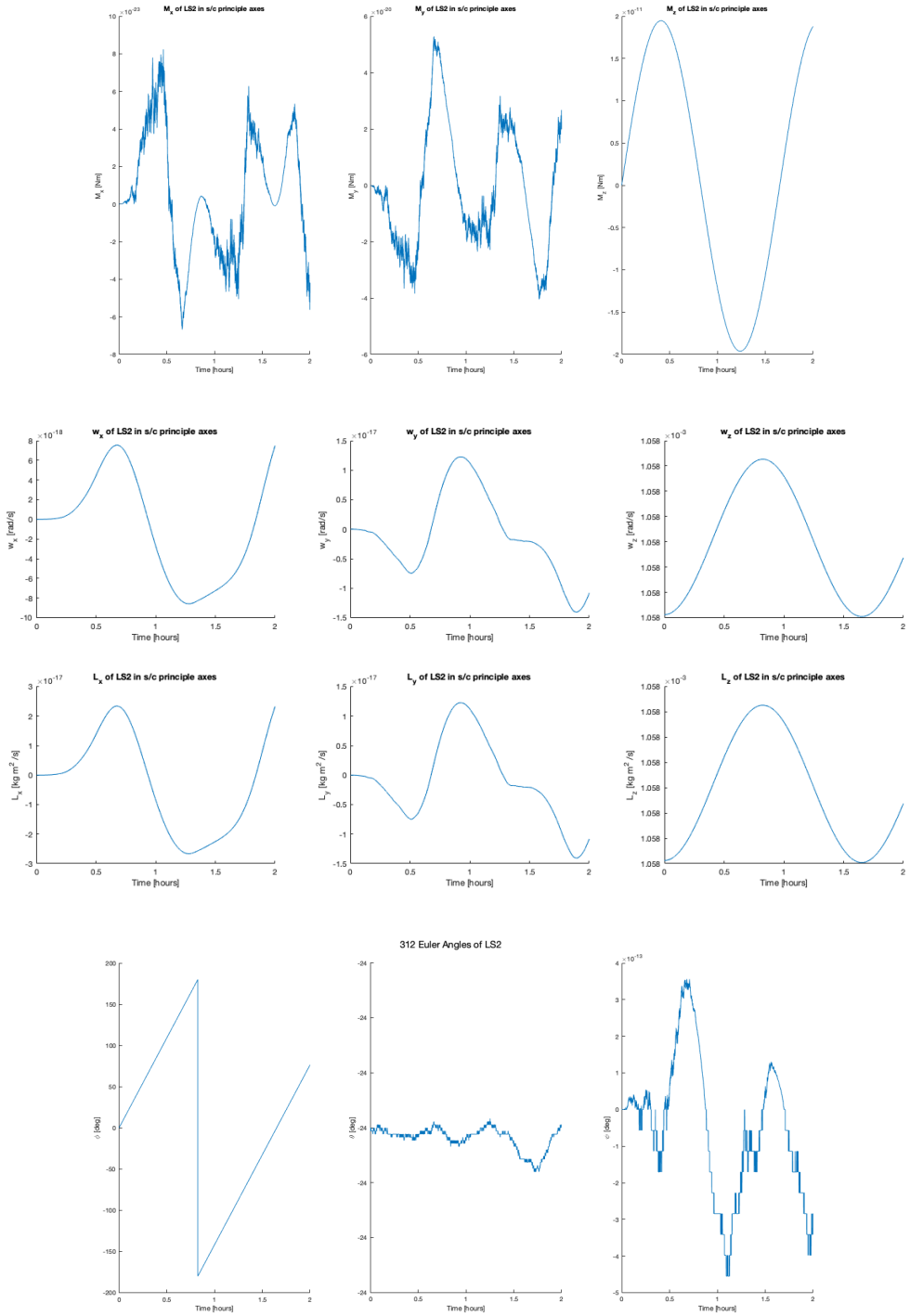

Figure 56: Gravity gradient stability assessment: stable unperturbed configuration.

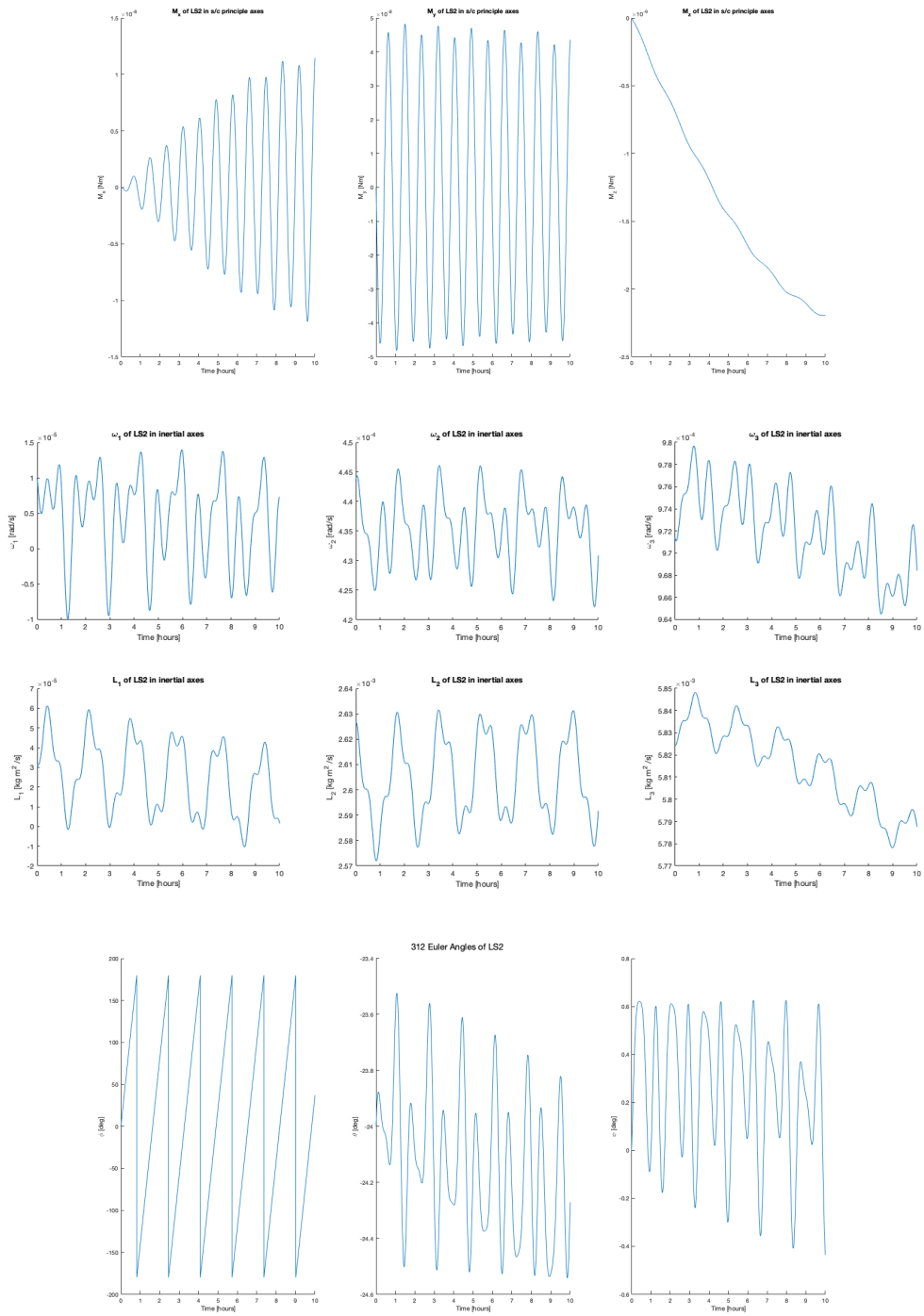

Figure 57: Gravity gradient stability assessment: stable perturbed configuration.

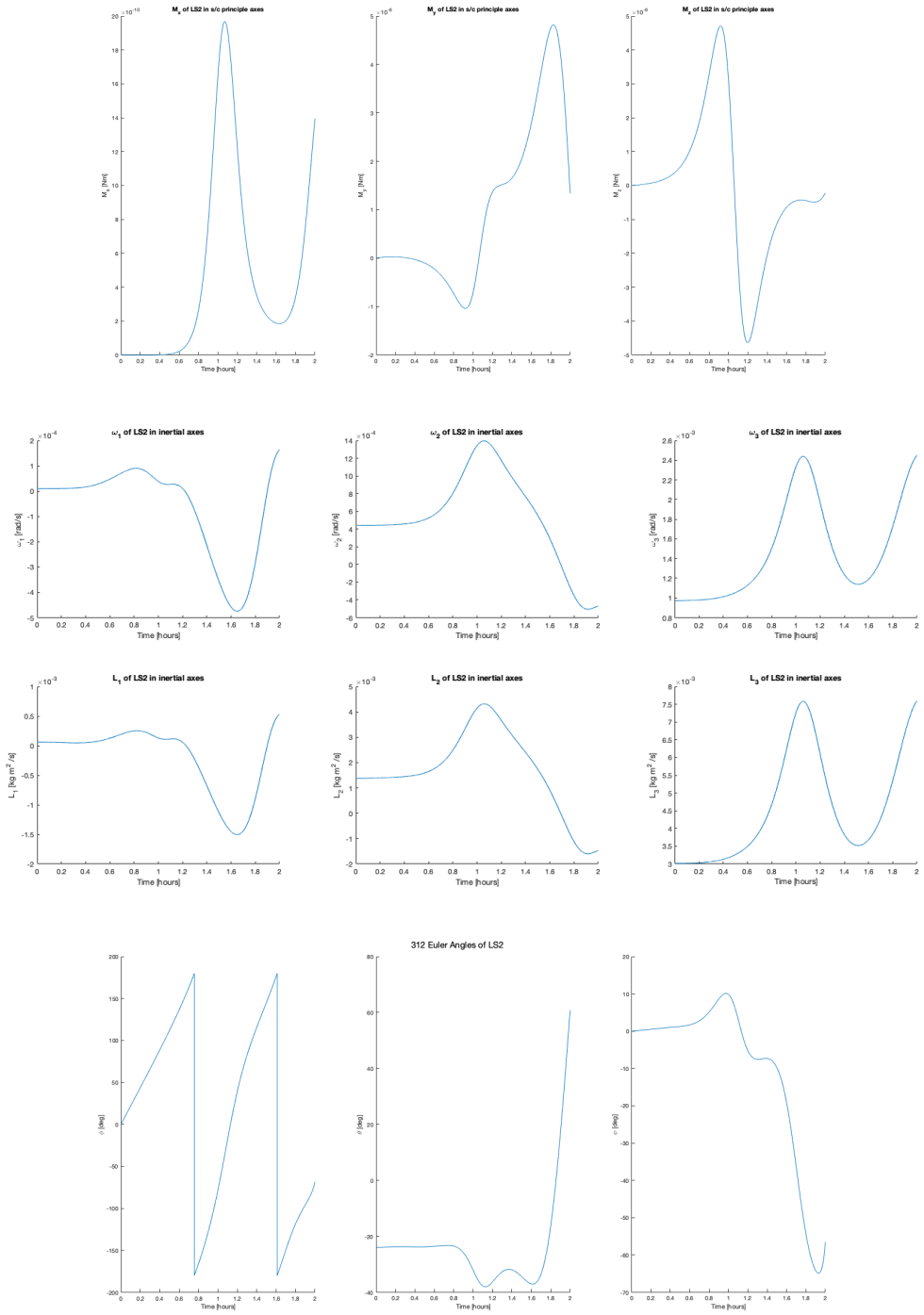

Figure 58: Gravity gradient stability assessment: unstable configuration.

I Attitude Estimation Comparisons

In the figures below, we compare our attitude estimations tactics - in Fig 59, we show the error between the q-method and deterministic method with sensor noise included. Notice that the magnitude of the error is very small, and generally shows close agreement between these two methods with the magnitude of sensor errors used.

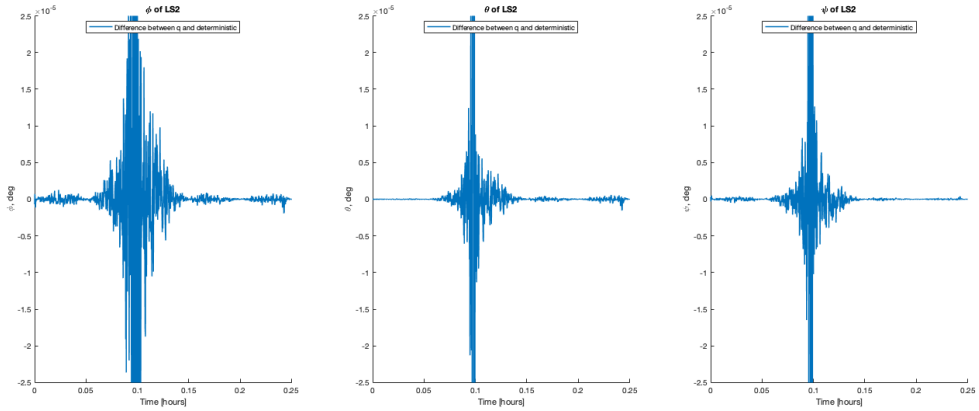

Figure 59: Error between q-method and deterministic method with sensor noise.

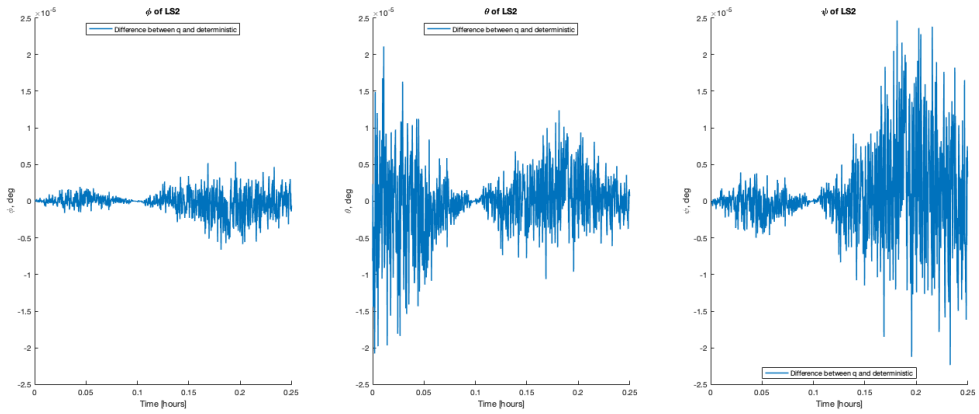

Figure 60: Error between q-method and deterministic method with sensor noise and error distribution. For comparison, Fig 59 was without error distribution.

We also analyze the effect of "distributing the error" of our measurements by re-writing our measurements and model as

$$\vec{m}_1 = \frac{\vec{B}_{meas} + \vec{S}_{meas}}{2} \quad \text{and} \quad \vec{m}_2 = \frac{\vec{B}_{meas} - \vec{S}_{meas}}{2}$$
$$\vec{v}_1 = \frac{\vec{B}_{ECI} + \vec{S}_{ECI}}{2} \quad \text{and} \quad \vec{v}_2 = \frac{\vec{B}_{ECI} - \vec{S}_{ECI}}{2}$$

such that

$$\vec{M} = \begin{bmatrix} | & | & | \\ \vec{p}_{meas} & \vec{q}_{meas} & \vec{r}_{meas} \\ | & | & | \end{bmatrix} \quad \text{and} \quad \vec{V} = \begin{bmatrix} | & | & | \\ \vec{p}_{ECI} & \vec{q}_{ECI} & \vec{r}_{ECI} \\ | & | & | \end{bmatrix}$$

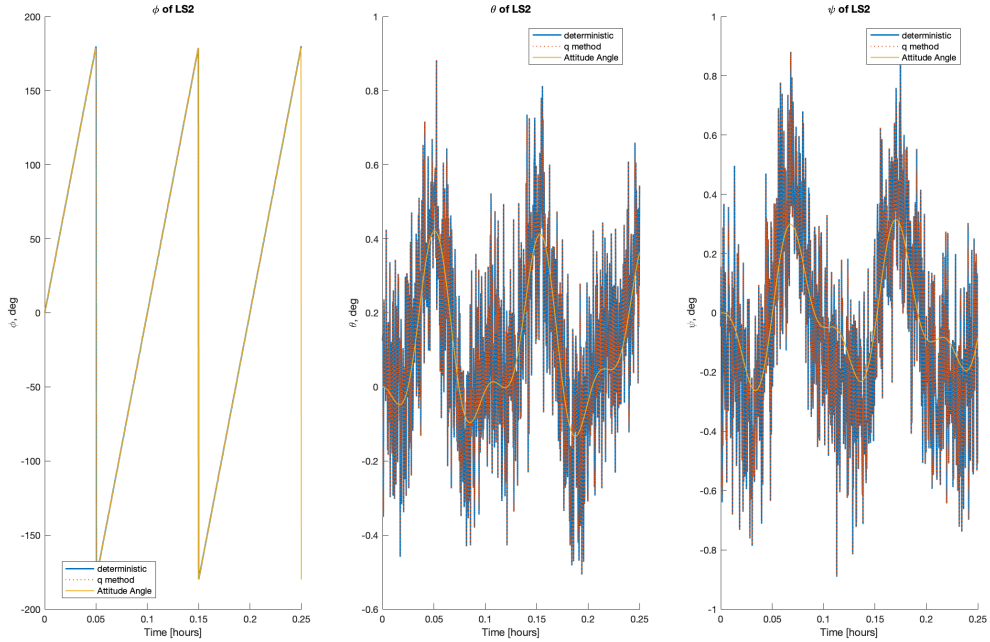

Figure 61: Attitude estimates with distributed error – non-distributed error can be seen in Section 6, Fig 32.

where $\vec{p} = \vec{m}_1$, $\vec{q} = \frac{\vec{p} \times \vec{m}_2}{|\vec{p} \times \vec{m}_2|}$, and $\vec{r} = \vec{p} \times \vec{q}$.

The effect of this distribution of error can be seen in Fig 60, 61, and 62. Note that the error redistribution generally reduces error (Fig 62), though the effect is not extremely pronounced. (Because the differences between q and deterministic are orders of magnitude less than the error between estimated and true, the error between deterministic and true with error distribution is not shown). Accordingly, the estimates provided by distributed measurements, seen in Fig 61, are very similar to those provided by Fig 32 in Section 6 of the main report. Interestingly, the difference between the two methods (q and deterministic) seems to increase at complementary times when the measurements are distributed versus not – without distribution, the difference is greatest around 0.1 hours, while with distribution, the difference is the smallest around 0.1 hours.

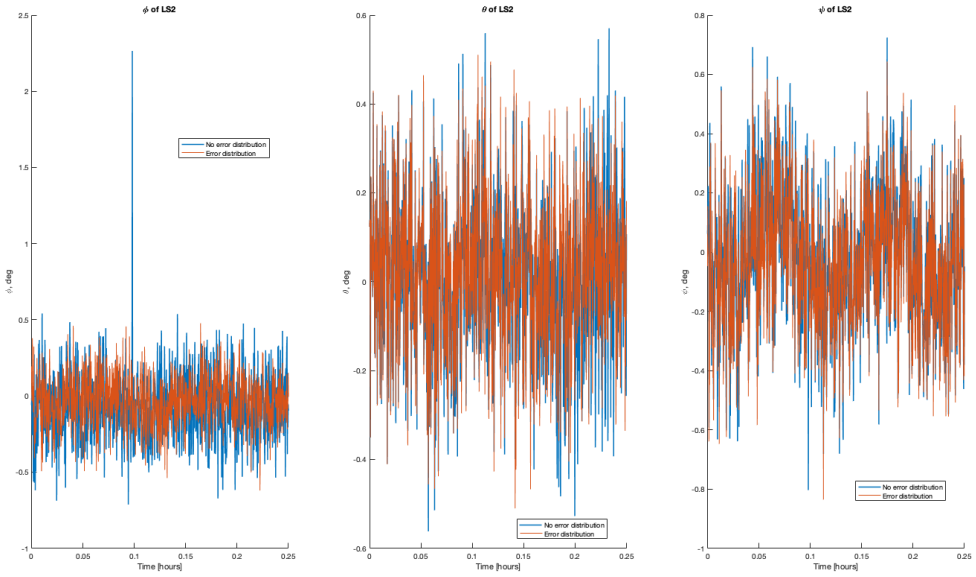

Figure 62: Error between q-method and true attitude with error distribution. The error without error distribution, previously shown in Fig 33, is shown again for comparison.

J Extended Kalman Filter Derivations

In this appendix, we document the derivation of key formulations for the implementation of our state estimation system, the Extended Kalman Filter (EKF). We represent our attitude state as

$$\vec{x} = \begin{bmatrix} \vec{q} \\ \vec{\omega} \\ \vec{b}_\omega \\ \vec{b}_B \\ \vec{b}_S \end{bmatrix} \tag{11}$$

where $\vec{q}$ is our quaternion, ω is our angular velocity expressed in principal axes, $\vec{b}_\omega$ is the gyroscope bias, $\vec{b}_B$ is the magnetometer bias, and $\vec{b}_S$ is the azimuth/elevation bias of the sun sensors. Note that the latter three vectors are unknown constants, which we fold into our state estimator to better make use of our measurement input.

We note that the time derivative of our state can be written as

$$\dot{\vec{x}} = \begin{bmatrix} \frac{1}{2}\Omega(\vec{\omega})\vec{q} = \frac{1}{2}\Lambda(\vec{q})\vec{\omega} \\ \frac{d\vec{\omega}}{dt} \\ \mathbf{0}_{3\times 1} \\ \mathbf{0}_{3\times 1} \\ \mathbf{0}_{2\times 1} \end{bmatrix} \tag{12}$$

Where

$$\Omega(\vec{\omega}) = \begin{bmatrix} 0 & \omega_3 & -\omega_2 & \omega_1 \\ -\omega_3 & 0 & \omega_1 & \omega_2 \\ \omega_2 & -\omega_1 & 0 & \omega_3 \\ -\omega_1 & -\omega_2 & -\omega_3 & 0 \end{bmatrix} \tag{13}$$

$$\Lambda(\vec{q}) = \begin{bmatrix} q_4 & -q_3 & q_2 \\ q_3 & q_4 & -q_1 \\ -q_2 & q_1 & q_4 \\ -q_1 & -q_2 & -q_3 \end{bmatrix} \tag{14}$$

$$\frac{d\vec{\omega}}{dt} = I^{-1}(\vec{T} - (\vec{\omega} \times I\vec{\omega})) \tag{15}$$

Where 14 comes from Lecture 6, 13 comes from an ADCS summary for FALCONSAT-3 [1], and 15 comes from Euler's equation of rigid-body motion with torque $\vec{T}$.

Using forward Euler formulation for the discrete-time derivative approximation, we can write our state at a time index $t+1$ as a function of a control input, u_t, the previous state at time index t,

$$\vec{x}_{t+1} = f(x_t, u_t) = x_t + \delta t \dot{\vec{x}}_t \tag{16}$$

where w_t is white additive Gaussian (WAG) process noise with covariance Q and δt is the size of the time step. Note that our control input is simply the input torque, $\vec{T}$, seen in Eq 15.

We now calculate the Jacobian of our state transition function, $f(x_t, u_t)$, for use in our EKF where we are unable to apply the true, non-linear function (what has been called in lecture the

"state transition matrix"):

$$\begin{aligned} A_t &= \frac{\partial f(\vec{x}, u_t)}{\partial \vec{x}}|_{\vec{x}=\vec{x}_t} \\ &= \mathbf{I}_{15\times 15} + \delta t \begin{bmatrix} \frac{1}{2}\Omega(\vec{\omega}) & \frac{1}{2}\Lambda(\vec{q}) & \mathbf{0}_{4\times 3} & \mathbf{0}_{4\times 3} & \mathbf{0}_{4\times 2} \\ \mathbf{0}_{3\times 4} & \Delta(\vec{\omega}) & \mathbf{0}_{3\times 3} & \mathbf{0}_{3\times 3} & \mathbf{0}_{3\times 2} \\ \mathbf{0}_{8\times 4} & \mathbf{0}_{8\times 3} & \mathbf{0}_{8\times 3} & \mathbf{0}_{8\times 3} & \mathbf{0}_{8\times 2} \end{bmatrix} \end{aligned} \tag{17}$$

where $\mathbf{I}_{15\times 15}$ is the identity matrix and we've defined

$$\begin{aligned} \Delta(\vec{\omega}) &= \frac{\partial \dot{\vec{\omega}}}{\partial \vec{\omega}} \\ &= \frac{\partial}{\partial \vec{\omega}}(I^{-1}(\vec{M} - (\vec{\omega} \times I\vec{\omega}))) \\ &= I^{-1}\left([I\vec{\omega}^{\times}]\frac{\partial \vec{\omega}}{\partial \vec{\omega}} - [\vec{\omega}^{\times}]\frac{\partial I\vec{\omega}}{\partial \omega}\right) \\ &= I^{-1}\left(\begin{bmatrix} 0 & -I_3\omega_3 & I_2\omega_2 \\ I_3\omega_3 & 0 & -I_1\omega_1 \\ -I_2\omega_2 & I_1\omega_1 & 0 \end{bmatrix} - \begin{bmatrix} 0 & -\omega_3 & \omega_2 \\ \omega_3 & 0 & -\omega_1 \\ -\omega_2 & \omega_1 & 0 \end{bmatrix}\begin{bmatrix} I_1 & 0 & 0 \\ 0 & I_2 & 0 \\ 0 & 0 & I_3 \end{bmatrix}\right) \\ &= I^{-1}\left(\begin{bmatrix} 0 & -I_3\omega_3 & I_2\omega_2 \\ I_3\omega_3 & 0 & -I_1\omega_1 \\ -I_2\omega_2 & I_1\omega_1 & 0 \end{bmatrix} - \begin{bmatrix} 0 & -I_2\omega_3 & I_3\omega_3 \\ I_1\omega_3 & 0 & -I_3\omega_1 \\ -I_1\omega_2 & I_2\omega_1 & 0 \end{bmatrix}\right) \\ &= \begin{bmatrix} \frac{1}{I_1} & 0 & 0 \\ 0 & \frac{1}{I_2} & 0 \\ 0 & 0 & \frac{1}{I_3} \end{bmatrix}\begin{bmatrix} 0 & (I_2 - I_3)\omega_3 & (I_2 - I_3)\omega_2 \\ (I_3 - I_1)\omega_3 & 0 & (I_3 - I_1)\omega_1 \\ (I_1 - I_2)\omega_2 & (I_1 - I_2)\omega_1 & 0 \end{bmatrix} \\ &= \begin{bmatrix} 0 & \frac{I_2 - I_3}{I_1}\omega_3 & \frac{I_2 - I_3}{I_1}\omega_2 \\ \frac{I_3 - I_1}{I_2}\omega_3 & 0 & \frac{I_3 - I_1}{I_2}\omega_1 \\ \frac{I_1 - I_2}{I_3}\omega_2 & \frac{I_1 - I_2}{I_3}\omega_1 & 0 \end{bmatrix} \end{aligned} \tag{18}$$

having leveraged the fact that our angular velocity is expressed in principal axes, making the inertia tensor, I, diagonal. We consider now our measurement vector,

$$\vec{y} = \begin{bmatrix} \vec{\omega}_{meas} \\ \vec{B}_{XYZ,meas} \\ \vec{S}_{az/el,meas} \end{bmatrix} \tag{19}$$

where $\vec{\omega}_{meas}$ is the measured angular velocity (in principal axes), $\vec{B}_{XYZ,meas}$ is the measured magnetic field (in principal axes), and $\vec{S}_{az/el,meas}$ is the measured azimuth and elevation of the Sun in the sun-sensor frame. We can write this measurement at time step t as a function of our state at the same time step,

$$\begin{aligned} \vec{y}_t &= g(\vec{x}_t) + v_t \\ &= \begin{bmatrix} \omega + \vec{b}_{\omega} \\ A(\vec{q})\vec{B}_{ECI} + \vec{b}_B \\ M(\tilde{A}A(\vec{q})\vec{S}_{ECI}) + \vec{b}_S \end{bmatrix} + v_t \end{aligned} \tag{20}$$

where v_t is WAG measurement noise with covariance R, ω is the true angular velocity in principal axes, $\vec{B}_{ECI}$ is the magnetic field in inertial coordinates, $\vec{S}_{ECI}$ is the sun direction in inertial

coordinates, $A(\vec{q})$ is the direction cosine matrix from inertial to principal coordinates, and $\tilde{A}$ is the rotation from principal frame to sun-sensor frame. Finally, we define the function $M(\vec{S})$ to be the function that transforms a unit vector to its azimuth/elevation representation,

$$M(\vec{S}) = \begin{bmatrix} \text{atan2}(S_2, S_1) \\ \text{acos}(S_3) \end{bmatrix} = \begin{bmatrix} \text{azimuth} \\ \text{elevation} \end{bmatrix} \tag{21}$$

Again, we will need the Jacobian of our measurement function, $g(x_t)$, for use in our EKF where we are unable to apply the true, non-linear function (what has been called in lecture the "sensitivity matrix"):

$$\begin{aligned} C_t &= \frac{\partial g(\vec{x})}{\partial \vec{x}}|_{\vec{x}=\vec{x}_t} \\ &= \begin{bmatrix} \mathbf{0}_{3\times 4} & \mathbf{I}_{3\times 3} & \mathbf{I}_{3\times 3} & \mathbf{0}_{3\times 3} & \mathbf{0}_{3\times 2} \\ \Gamma(\vec{q}, \vec{B}_{ECI}) & \mathbf{0}_{3\times 3} & \mathbf{0}_{3\times 3} & \mathbf{I}_{3\times 3} & \mathbf{0}_{3\times 2} \\ \tilde{M}(\tilde{A}A(\vec{q})\vec{S}_{ECI})\tilde{A}\Gamma(\vec{q}, A(\vec{q})\vec{S}_{ECI}) & \mathbf{0}_{2\times 3} & \mathbf{0}_{2\times 3} & \mathbf{0}_{2\times 3} & \mathbf{I}_{2\times 2} \end{bmatrix} \end{aligned} \tag{22}$$

where we define

$$\begin{aligned} \Gamma(\vec{q}, \vec{V}) &= \frac{\partial (A(\vec{q})\vec{V})}{\partial \vec{q}} \\ &= \frac{\partial}{\partial \vec{q}} \begin{bmatrix} (q_4^2 + q_1^2 - q_2^2 - q_3^2)V_1 + (2q_1q_2 + 2q_3q_4)V_2 + (2q_1q_3 - 2q_2q_4)V_3 \\ (2q_1q_2 - 2q_3q_4)V_1 + (q_4^2 - q_1^2 + q_2^2 - q_3^2)V_2 + (2q_2q_3 + 2q_1q_4)V_3 \\ (2q_1q_3 + 2q_2q_4)V_1 + (2q_2q_3 - 2q_1q4)V_2 + (q_4^2 - q_1^2 - q_2^2 + q_3^2)V_3 \end{bmatrix} \\ &= 2 \begin{bmatrix} \vec{a}\cdot\vec{V} & \vec{b}\cdot\vec{V} & \vec{c}\cdot\vec{V} & \vec{d}\cdot\vec{V} \\ -\vec{b}\cdot\vec{V} & \vec{a}\cdot\vec{V} & -\vec{d}\cdot\vec{V} & \vec{c}\cdot\vec{V} \\ -\vec{c}\cdot\vec{V} & \vec{d}\cdot\vec{V} & \vec{a}\cdot\vec{V} & -\vec{b}\cdot\vec{V} \end{bmatrix} \\ \text{for } \vec{a} &= \begin{pmatrix} q_1 \\ q_2 \\ q_3 \end{pmatrix}, \ \vec{b} = \begin{pmatrix} -q_2 \\ q_1 \\ -q_4 \end{pmatrix}, \ \vec{c} = \begin{pmatrix} -q_3 \\ q_4 \\ q_1 \end{pmatrix}, \ \vec{d} = \begin{pmatrix} q_4 \\ q_3 \\ -q_2 \end{pmatrix}, \end{aligned} \tag{23}$$

and further define the function

$$\begin{aligned} \tilde{M}(\vec{V}) &= \frac{\partial M(\vec{V})}{\partial \vec{V}} \\ &= \begin{bmatrix} \frac{-V_2}{V_1^2+V_2^2} & \frac{V_1}{V_1^2+V_2^2} & 0 \\ 0 & 0 & \frac{-1}{\sqrt{1-V_3^2}} \end{bmatrix} \end{aligned} \tag{24}$$

With these definitions in hand, we're prepared to implement our EKF. Given a prior state distribution defined by the prior mean, μ_t and the prior covariance, Σ_t, we can write the EKF algorithm as

$$\begin{aligned} A_t &= \frac{\partial f(\vec{x}, u_t)}{\partial \vec{x}}|_{\vec{x}=\mu_t} \\ \mu_p &= f(\mu_t, u_t) \\ \Sigma_p &= A_t \Sigma_t A_T^T + Q \\ C_t &= \frac{\partial g(\vec{x})}{\partial \vec{x}}|_{\vec{x}=\mu_p} \\ K_t &= \Sigma_p C_t^T (C_t \Sigma_p C_t^T + R)^{-1} \\ \mu_{t+1} &= \mu_t + K_t(y_{t+1} - g(\mu_p)) \\ \Sigma_{t+1} &= (I - K_t C_t)\Sigma_p (I - K_t C_t)^T + K_t R K_t^T \end{aligned} \tag{25}$$

Where our pre- and post-fit residuals are

$$\begin{aligned} z_{t+1,pre} &= y_{t+1} - \mu_p \\ z_{t+1,post} &= y_{t+1} - \mu_{t+1} \end{aligned} \tag{26}$$

Additional EKF Notes

We can further consider the partial derivative of our state transition function, $f(x_t, u_t)$, with respect to the control input, u_t. As noted previously, our input to the system is simply the input torque (one could also add disturbance torques into this input, or model them as uncertainty on the input itself). The resulting "control input matrix" for a control torque input in principal axes u_t is simply

$$\begin{aligned} B_t &= \frac{\partial f(x_T, u)}{\partial u}|_{u=u_t} \\ &= dtI^{-1} \end{aligned} \tag{27}$$

where I is the inertia tensor (here in principal axes, i.e. diagonal).

Quaternion normalization can become an issue when propagating attitude states, as our first-order derivative implementation does not preserve quaternion length. Therefore, we can build in quaternion normalization to our update step: consider the matrix Q, which is identical to $\mathbf{I}_{15}$ except that the upper left (4×4) submatrix is $\frac{1}{|q|}\mathbf{I}_4$ - we can then apply apply this matrix to our state transition matrix after the forward-Euler step to normalize the quaternion:

$$\vec{x}_{t+1} = f(x_t, u_t) = Q(x_t + \delta t \dot{vec}x_t) \tag{28}$$

This modification changes our state transition matrix, to be

$$\begin{aligned} A_t &= \frac{\partial f(\vec{x}, u_t)}{\partial \vec{x}}|_{\vec{x}=\vec{x}_t} \\ &= \tilde{Q} + \delta t \begin{bmatrix} \frac{1}{2}\Omega(\vec{\omega}) \odot \mathcal{Q} & \frac{1}{2|q|}\Lambda(\vec{q}) & \mathbf{0}_{4\times3} & \mathbf{0}_{4\times3} & \mathbf{0}_{4\times2} \\ \mathbf{0}_{3\times4} & \Delta(\vec{\omega}) & \mathbf{0}_{3\times3} & \mathbf{0}_{3\times3} & \mathbf{0}_{3\times2} \\ \mathbf{0}_{8\times4} & \mathbf{0}_{8\times3} & \mathbf{0}_{8\times3} & \mathbf{0}_{8\times3} & \mathbf{0}_{8\times2} \end{bmatrix} \end{aligned} \tag{29}$$

where $\odot$ is the element-wise multiplication operator, and we define

$$\begin{aligned} \mathcal{Q} &= \frac{\partial}{\partial q}\left(\frac{q}{|q|}\right) \\ &= \frac{1}{|q|^3}\begin{bmatrix} |q|^2 - q_1^2 & -q_1q_2 & -q_1q_3 & -q_1q_4 \\ -q_1q_2 & |q|^2 - q_2^2 & -q_2q_3 & -q_2q_4 \\ -q_1q_3 & -q_3q_2 & |q|^2 - q_3^2 & -q_3q_4 \\ -q_1q_4 & -q_2q_4 & -q_3q_4 & |q|^2 - q_4^2 \end{bmatrix} \end{aligned} \tag{30}$$

and $\tilde{Q}$ is identical to $\mathbf{I}_15$ except that the upper left (4×4) submatrix is $\mathcal{Q}$.

Finally, we note that an EKF formulation without the inclusion of sensor bias can be achieved by simply taking submatrices of our derivations above: the (7×7) upper left sub-matrix of A_t, and the first seven columns of the C_t sensitivity matrix.

K Extended Kalman Filter Result Analysis

In the figures below, we analyze the performance of the EKF implemented without the estimation of sensor bias, as discussed in Problem Set 7. Figures 63 and 64 show the attitude error and the absolute angular velocity error, respectively, from our EKF. The attitude errors are initially quite large (as expected, given our poor initial estimate and high uncertainty). The approximate range of these errors is encapsulated well by the associate covariance output by the EKF, presented in Figures 65 and 66; note that in general, the error of our estimate is within the 95% confidence interval suggested by the associated covariance. We've used the formulation developed in John B. Schleppe's thesis [10] to transform the covariance of our quaternions to that of the associated Euler angles.

Finally, we consider our residuals (both the pre-fit and post-fit residuals whose computation is described in Appendix J) for our various measurements, as plotted in Figures 67-69. The plots include the 95% confidence interval based on the covariance of the last 1000 data points - the resulting values are very similar to the sensor errors that we use for generating sensor noise (10 deg/s for the gyroscope, 1 μT for the magnetic sensors, and 3 deg for the azimuth and elevation), as expected.

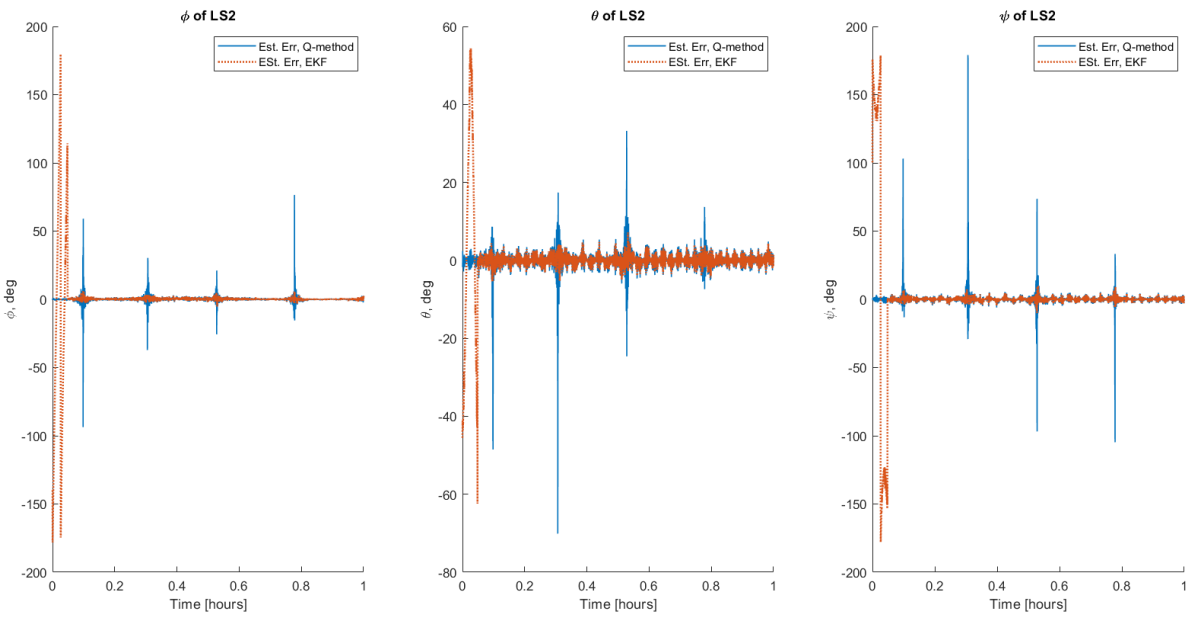

Figure 63: Attitude error from EKF state estimation.

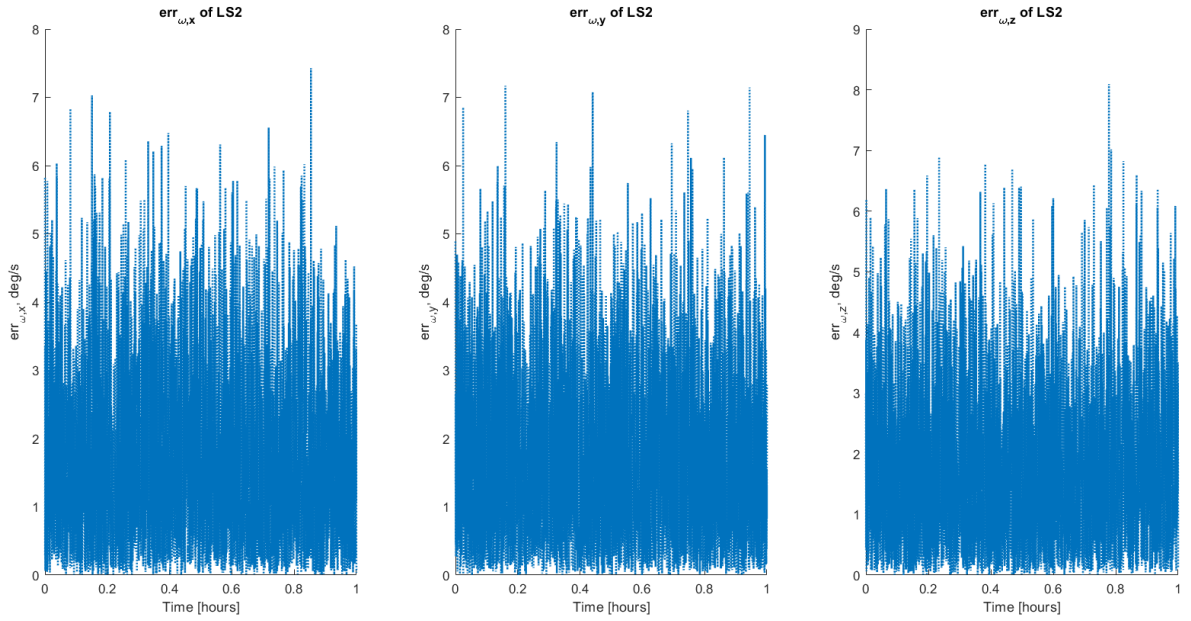

Figure 64: Angular velocity error from EKF state estimation.

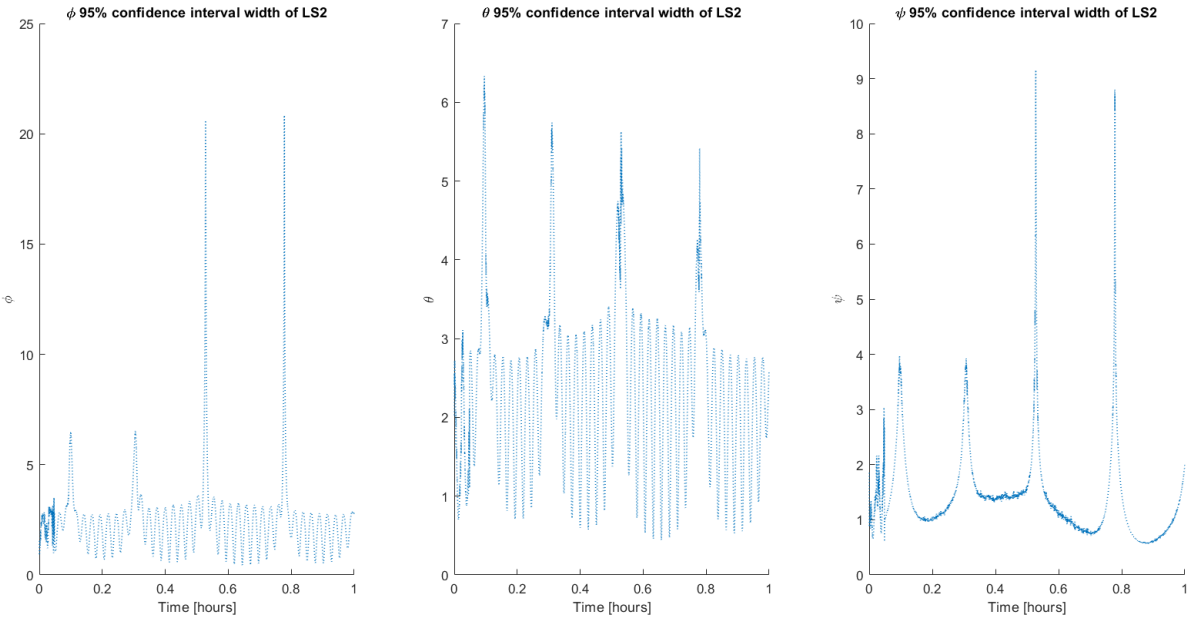

Figure 65: Attitude confidence interval from EKF state estimation.

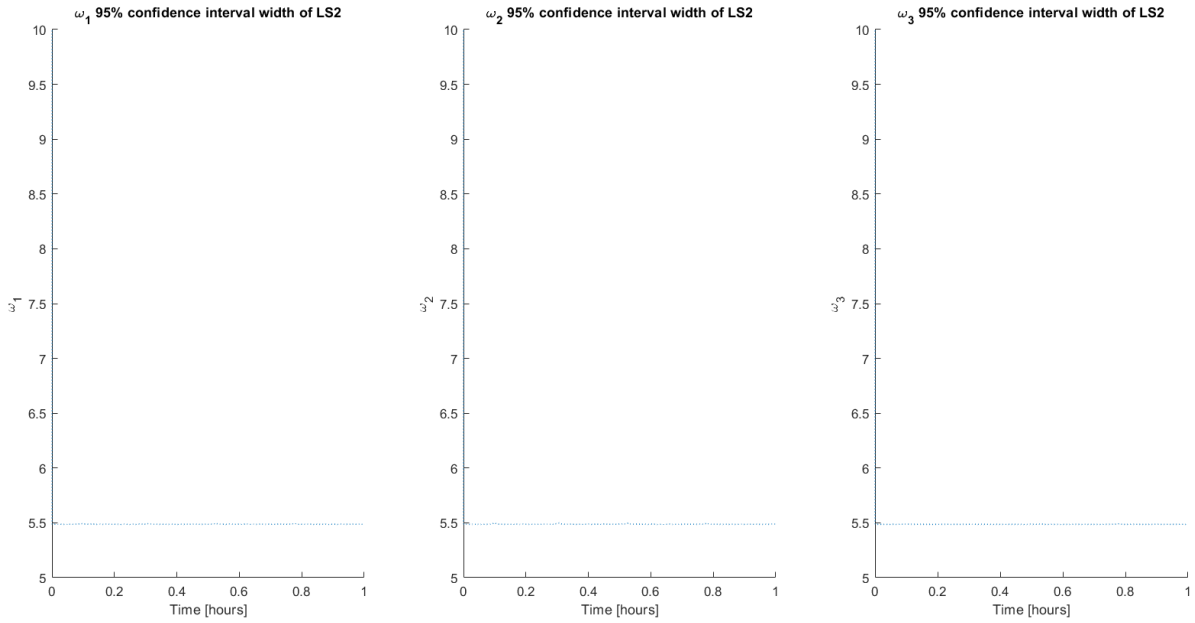

Figure 66: Angular velocity confidence interval from EKF state estimation.

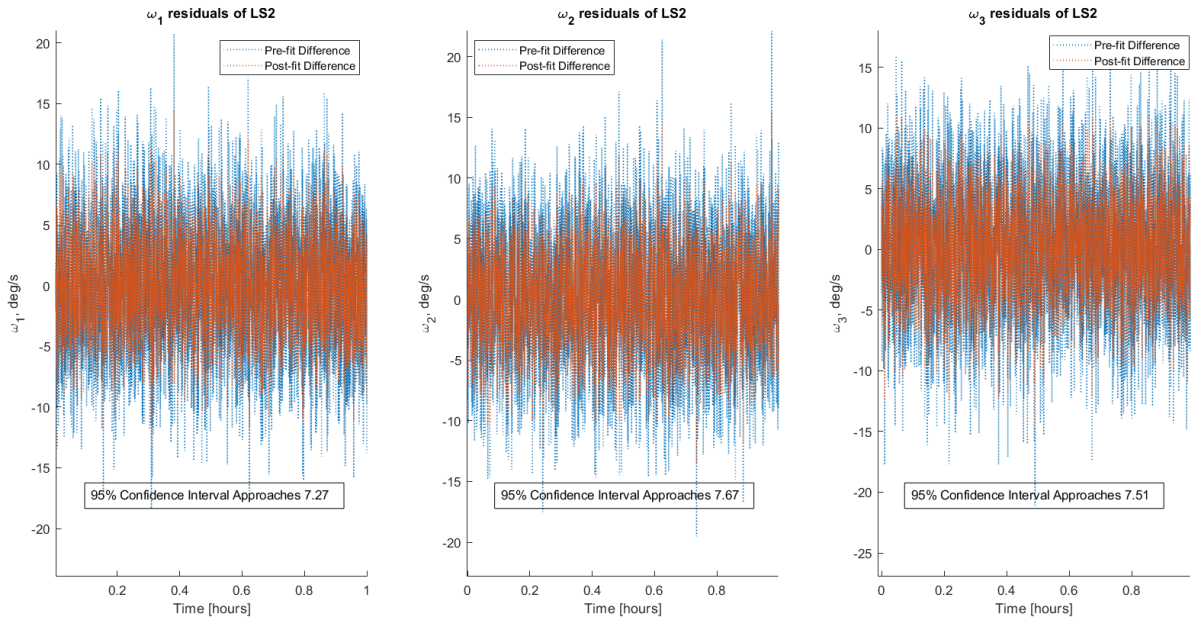

Figure 67: Angular velocity pre- and post-fit residuals from EKF state estimation.

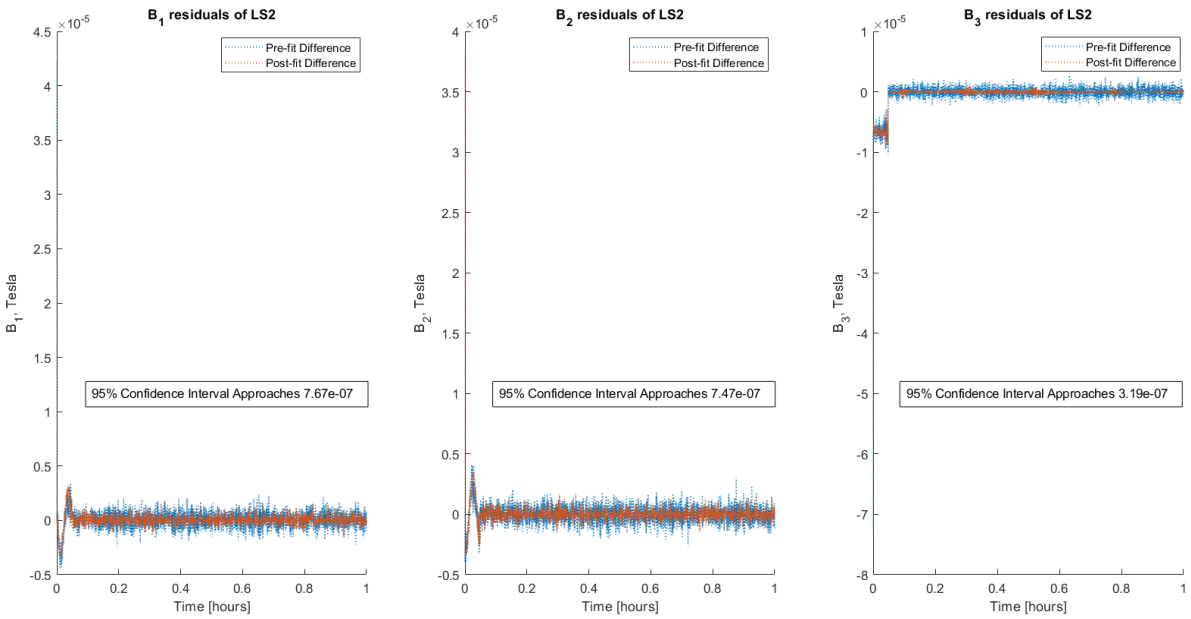

Figure 68: Magnetic sensor pre- and post-fit residuals from EKF state estimation.

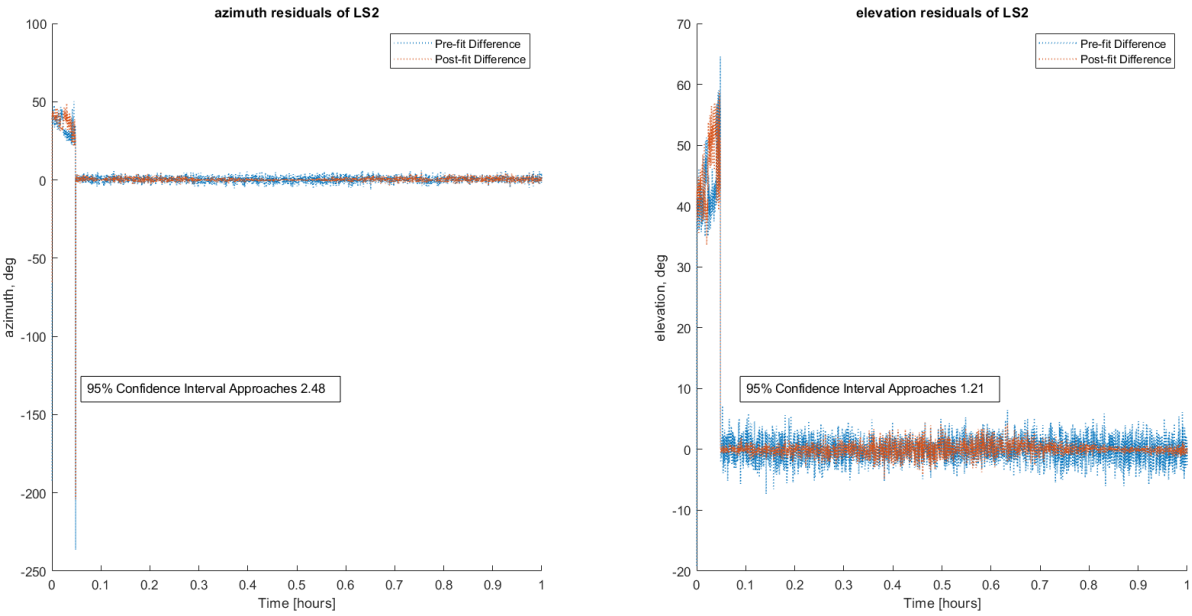

Figure 69: Sun sensor pre- and post-fit residuals from EKF state estimation.